2009

Qualitative measurements of pressure-atomized sprays through simultaneous collection of planar fluorescence, phosphorescence, and Mie scattering data

Jacob Brian Schmidt
Iowa State University

Recommended Citation

www.manaraa.com

Qualitative measurements of pressure-atomized sprays through simultaneous collection of

planar fluorescence, phosphorescence, and Mie scattering data

by

Jacob Brian Schmidt

A thesis submitted to the graduate faculty

in partial fulfillment of the requirements for the degree of

MASTER OF SCIENCE

Major: Mechanical Engineering

Program of Study Committee:
Terrence Meyer, Major Professor
Theodore Heindel
Hui Hu

Iowa State University

Ames, Iowa

2009

TABLE OF CONTENTS

iii

LIST OF FIGURES

ABSTRACT

A laser diagnostic technique useful for qualitatively locating and describing regions of vapor and liquid structures of a pressure atomized fuel spray is examined. While Mie scattering is sensitive to the liquid phase within a spray, planar laser-induced fluorescence is sensitive to both the liquid and vapor phases. Hence, a comparison of images utilizing these two techniques could be used to qualitatively distinguish regions of vapor from regions dominated by droplets. Quantitative subtraction of the two signals is subject to significant error in polydisperse sprays, however, due to the fact that scattering is sensitive to droplet surface area (diameter squared) while fluorescence is sensitive to droplet volume (diameter cubed). Moreover, even qualitative comparison of the two signals may yield false identification of fuel vapor because of possible differences in signal behavior within dense regions of the spray. By simultaneously capturing phosphorescence in addition to fluorescence and Mie scattering, it is possible to gain further insight because phosphorescence is proportional to droplet volume, like fluorescence, but is sensitive only to droplets, like Mie scattering. Hence, phosphorescence can be used to determine whether differences between fluorescence and Mie scattering signals are due to the presence of fuel vapor or due simply to the different photophysics between the two techniques. The current work shows the utility of using phosphorescence for added information and advances the state of the art by (1) testing the use of fluorescence, phosphorescence, and Mie scattering (FPM) in a dense spray, (2) testing FPM in a multi-component fuel, (3) implementing FPM in a practical device, and (4) conducting tests with FPM under elevated temperatures. Signal collection techniques and data conditioning methods are presented and discussed for both

laboratory and test cell applications. Results show that the measurement of fuel vapor from differences in fluorescence and Mie scattering data can be misleading due to variations in multiple scattering with these two techniques. By adding phosphorescence, it is possible to show that regions that appear to consist of fuel vapor from fluorescence are more likely attributable to diffuse scattering from a dense field of droplets within the spray. This is an important result that shows the significance of simultaneous collection of FPM signals in practical fuel sprays. Suggestions to improve and advance the technique are also presented.

CHAPTER 1. INTRODUCTION

Liquid sprays have been a topic of great interest for some time, but predicting their behavior has proven to be very difficult. Understanding and observing the mechanics that create and destroy the droplets and other liquid structures presents an interesting challenge in that the measurement technique must be non-intrusive so as to not to disturb the flow field. The balance between surface tension and external fluid mechanical forces results in a complex flowfield that eventually undergoes atomization and evaporation. Understanding this process holds implications to many fields, including but not limited to fuel sprays, cooling sprays, aerosol collection sprays, etc. The primary area of focus for this study is with regard to fuel sprays for power and propulsion applications. Since fuels must vaporize before combustion can take place, determining the rate and fuel vaporization is critical for these applications.

A laser diagnostic technique is presented that is used to gain further insight into spray characteristics and fluid atomization. The specific area of focus is in understanding the relationship between liquid and vapor regions of a pressure atomized spray. This relationship is investigated through simultaneous collection of fluorescence, phosphorescence, and Mie scattering data. Through image conditioning and subtraction processes it is suggested that an image could be produced that removes all liquid based signal and leaves only the signal from vapor regions. A variety of injection pressures, flow rates, spray orientations, temperatures, fuels and other flow conditions are tested to further support this hypothesis. These conditions are tested in two different testing configurations. The first is within the Multiphase Reacting Flow Laboratory at Iowa State University and is geared towards proving the theoretical capabilities of the technique. The second configuration involves a demonstration within an

test section with heated crossflow and includes fuel injection into heated and unheated crossflows.

A literature review is presented that discusses the history of the technology and each technique. This is necessary for understanding the current motivation and direction of the research. The experimental setups are then broken down into each of their components and discussed in detail, including the spray system, laser system, timing control, and cameras. After experimental components are discussed, all data collected is presented in for comparison while pointing out the similarities and differences between the different conditions. Once presented, correction and display methods such as scaling and background subtraction are discussed, and conclusions are presented. Measurement challenges, such as multiple scattering, are analyzed and discussed, and suggestions for future work that may help alleviate these difficulties are presented. Lastly, a summary of all items discussed is presented, recommendations for interpretation of the data and for future work is provided, and final conclusions are made for the reader.

CHAPTER 2. REVIEW OF LITERATURE

This Chapter gives a brief overview of the topics useful in understanding the current research. Section 2.1 will discuss items related to fuel sprays and their applications. Section 2.2 will detail characteristics about the fuels being used. These include descriptions of why each fuel is being used and implications to the current research. Section 2.3 will discuss the concepts of fluorescence, Mie scattering and phosphorescence. Specifically, the history of each technique, how each is used and other areas to which this technology can be applied.

2.1 Sprays

The demand for high-efficiency and ultra-low emissions from combustion based devices has pushed the design, development, and incorporation of advanced combustion concepts forward. One area of advancement is in the control of fuel/air mixture preparation through the design of fuel injection nozzles. In most cases, liquid fuel is atomized, heated, and vaporized to create a fuel/air mixture prior to combustion. In order to achieve optimum performance over the entire combustion process, steps must be taken optimize the degree of vaporization and to stabilize the flame (Eckbreth 1988). Many designs have been investigated to achieve this high degree of vaporization and, in turn, efficiency while also to reduce unwanted emissions. Advanced computational and experimental tools have proven to be valuable in the development of modern injectors for combustion devices. Among these experimental tools, non-intrusive laser diagnostics techniques have made it possible to observe many of the thermal/fluid and chemical dynamics of interest in such fuel sprays (Eckbreth 1988).

Investigations of these fuel/air mixtures have been conducted for many years, often while utilizing a model fuel in a theoretical application (Schulz 2005). While providing valuable

fundamental insight, the drawback is that these tests to not simulate the actual conditions in which a multi-component fuel spray typically resides and combusts. Despite the inherent importance of understanding complex fuel sprays, experimental approaches for such applications are not as well developed.

2.2 Fuel Studies

Fuel-air mixing and concentration studies have great importance when it comes to efficient combustion. Research to improve performance of liquid-fueled combustors has been conducted for a number of years in several areas. These range from determining fuel distributions in a spark ignited engine (Baritaud et al. 1992), to determining the fraction of unburnt fuel being exhausted from jet engines (Seyfried et al. 2005), to finding emission concentrations (Bazile et al. 1995), and everything in between.

Acetone is chosen as a fuel of choice for many laboratory studies and its photophysical properties have been well documented (Tran et al. 2005, Lozano 1992, Koch et al. 2004, Bryant et al. 2000). It is chosen for its linear relationships between fluorescence intensity, laser power and acetone vapor concentration. It also has non-overlapping absorption and emission spectra, allowing straightforward separation of excitation and detection wavelengths.   Acetone has been used for thermal mapping because its signal can be related to temperature using single wavelength excitation (Kearney et al., 2003) and dual-wavelength excitation (Thurber et al., 1997, 1998). Further studies have shown that signal intensities vary by less than 10% across applied temperature and pressure ranges (Bryant et al. 2000). Pressure and composition studies have also shown that acetone signal levels at three different wavelengths (Thurber et al. 1999) can produce highly repeatable results.

Ambient oxygen quenching of fluorescence signals (Bortolus et al. 1986) have shown little dependence on oxygen concentration, which further supports the case to use acetone as a benchmark fuel in exploratory diagnostic work.

Acetone is also known as a fuel of choice for different studies that involve signal discrimination. It is shown that acetone absorbs from 225nm to 320nm while emitting from 350nm to 550nm. When using this technique with a filter or a lens that passes only the upper range of wavelengths, it is easy to discriminate between laser scatter and fluorescence signal. Acetone also proves itself to be relatively benign when compared with other tracers used for laser-induced fluorescence (Seitzman, et al. 1993, Richie et al. 2004).

Shown below in Figure 1 is a plot of absorption of laser light based on wavelength collected using a UV-Vis spectrometer. Solutions were prepared and diluted with methanol, which does not absorb light in this spectrum. While the 1ppm mixture of jet-A fuel shows stronger absorption at lower wavelengths, both the 250ppm acetone and 1ppm jet-A show elevated absorption levels in the purposed UV region near 266nm. It should be noted that the jet-A fuel does show stronger absorption than similar concentrations of acetone.
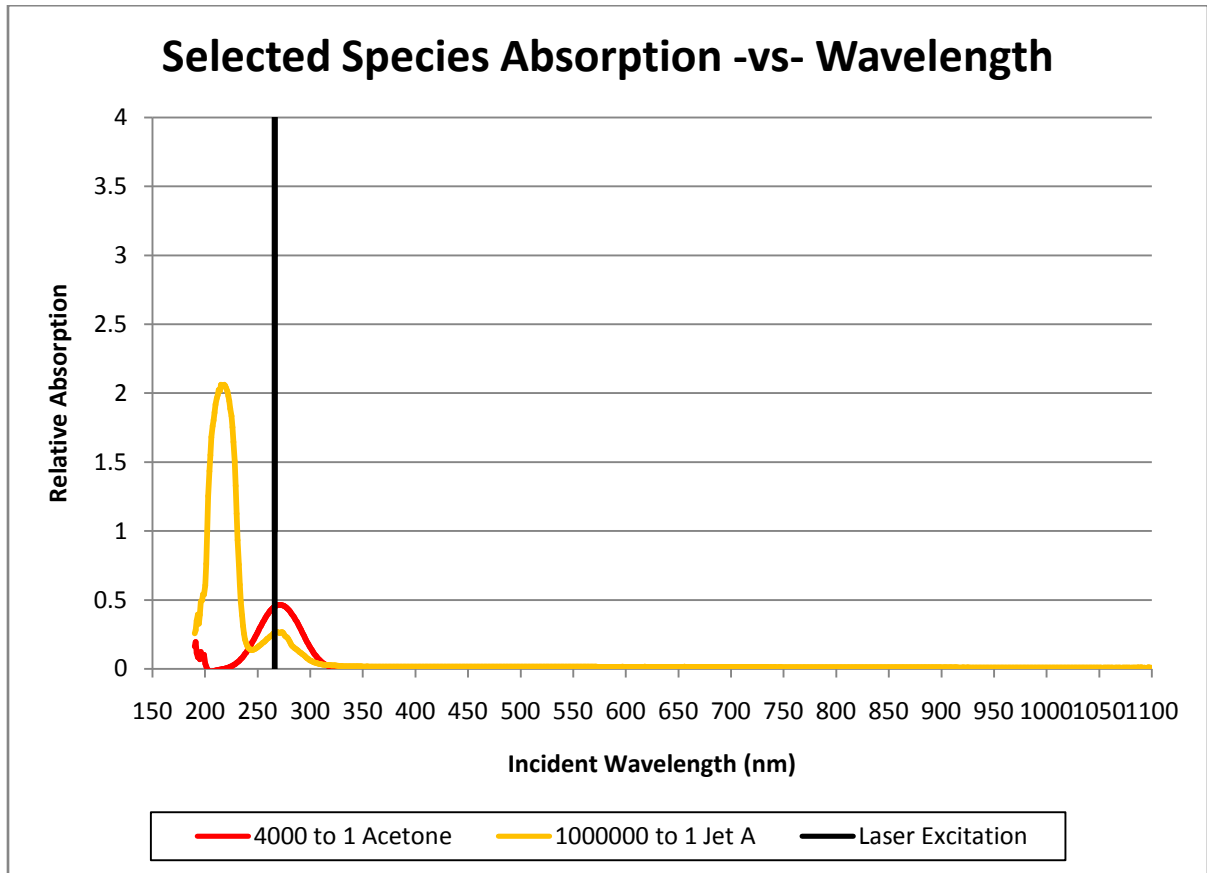
Figure 1: Acetone and Jet-A fuel absorption dependencies on wavelength.

Lastly, acetone has a very well documented dissociation history and has been tested at elevated temperatures and pressures with the same techniques to be employed in this research (Emerich et al. 2000).

In the current work, acetone is used for laboratory set-up, but most of the experiments involve the use of jet-A fuel for fluorescence, phosphorescence, and Mie scattering. Because of different distillation curves between jet-A and acetone, it is important to study the applicability of the current approach to realistic fuels.

2.3 Fluorescence, Phosphorescence and Mie Scattering

This section will provide background on the laser-based experimental techniques and concepts employed in the current work. One of the main limitations with investigating some of these fuel-air mixing sprays is being non-intrusive. This is a main advantage of laser-based experimentation. Thanks to their high-temporal resolution and non-intrusive nature, laser-based diagnostics have become the most popular methods for investigating turbulent, reacting flow fields.

2.3.1 Fluorescence Techniques

Laser-induced fluorescence involves excitation of a molecule to a higher quantum state with laser irradiation and subsequent detection of the spontaneous emission photon released when the molecule decays to a lower quantum state. LIF theory and its applications are described in greater detail in numerous references (e.g., Lucht 1987; Eckbreth 1988). While the excited energy level is populated only by laser excitation, it is depopulated through a number of competing mechanisms, as shown in Figure 2. First is the spontaneous emission rate which produces the desired LIF signal. This spontaneous emission has been characterized by short lifetimes (Seitzman et al. 1993, Lozano 1992) and is proven to depend on the intersystem crossing efficiency (Borkman et al. 1966, Haas et al. 1978). Collisional quenching, which describes random collisions with other molecules that lead to energy losses without corresponding photon release, or upper-level losses, such as collisionless processes including predissociation of molecules or intersystem crossing into adjacent energy levels, do not produce the required fluorescence event. It is this intersystem crossing of molecules to adjacent energy levels that produces a phosphorescence signal. This can be seen below in Figure 2.
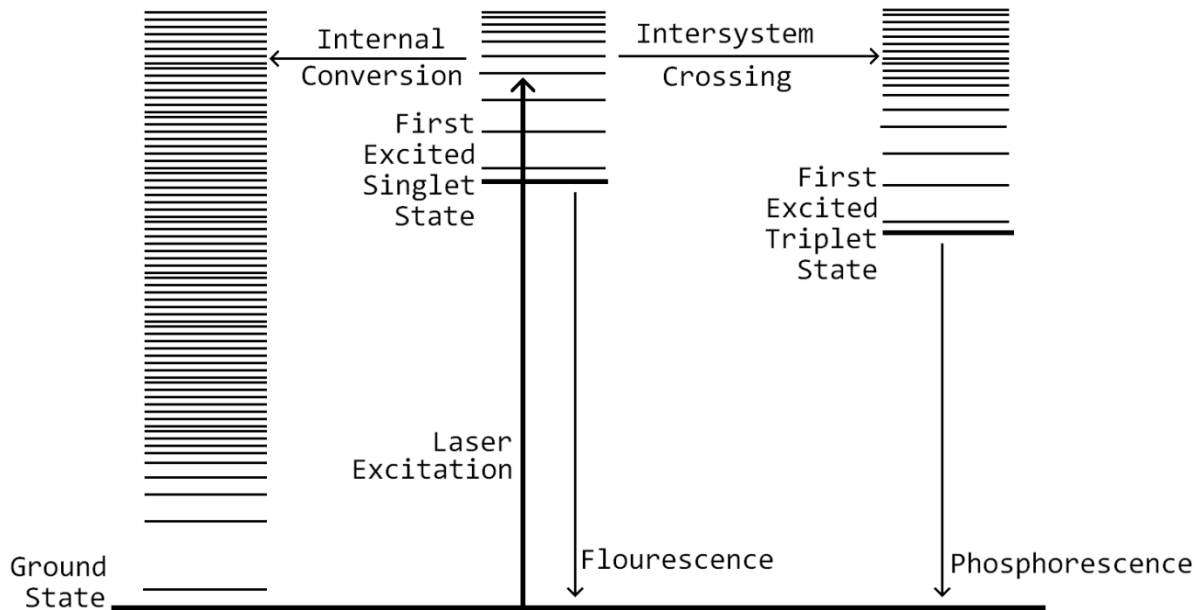
Figure 2: Schematic for LIF transfer process in the acetone molecule

Planar laser induced fluorescence (PLIF) is a technique proven to be non-intrusive and able to provide two-dimensional instantaneous snapshots of a variety of combusting fuel flow parameters. These parameters are species concentration, temperature, and pressure. Specific research has been done to investigate some of these parameters.

Specifically, PLIF has been shown to measure gaseous and liquid concentrations, velocities, and temperatures (Seitzman et al. 1993). Many other studies have investigated gaseous fuel-air mixing.

Some of these studies have shown dependencies on incident wavelength related to output signal strength (Costella et al. 1986, Seitzman et al. 1993, Tran et al. 2005). This work has shown that while dependencies are low, there are recordable differences between tests employing 300+nm wavelengths compared to those using 260-280nm wavelengths, with an increased signal level in the former. Other work has focused simply on the effects of pressure and incident wavelength on decay lifetimes of fluorescence. Research such as that done by Greenblatt et al.

(1984) have studied this behavior showing that charging the fuel with an oxygen depleted gas will significantly increase the noticed lifetime of the fluorescence of the fuel.

The disadvantage to using fluorescence is that both liquid droplets and vapor both fluoresce with an intensity related to concentration which makes it hard to analyze vapor-only regions. Due to the importance of accurately describing behavior of vapor regions it is desired to use an experimental technique that will enable easier discrimination between droplets and vapor regions. Both scattering, such as Mie and Rayleigh scattering, and phosphorescence techniques are able to aide in this type of measurement.

2.3.2 Scattering Techniques

Scattering techniques employ incident light to elastically scatter off the surface of large liquid structures and droplets. The returned signal is of the same wavelength of the incident light and therefore can be harder to discriminate between incident laser light and return signal. There are two types of scattering processes available for laser diagnostics. The first is Rayleigh scatter. This scatter occurs when the incident light has a wavelength that is larger than the body that it interacts with. The physical process that occurs during this type of scattering is complex and is outside the scope of this research and will not be discussed in depth. The second, Mie scatter, occurs when the scattered light has a wavelength that is smaller than the physical body that it is scattering off of. This is the type of scattering that this study will be concerned with as the droplets can be assumed to be larger than the 266nm beam that is incident on them.

Both Mie and Rayleigh scattering methods can be used to assist in a number of areas related to spray laser diagnostics. The area of specific interest to the current research is particle sizing. This can be accomplished using one of several different principles based on diffraction

(Anon 1983), visibility (Farmer 1972, Bachalo et al. 1980), scattered intensity (Yule el al. 1983), a combination of visibility and scattered intensity (Hess 1984), and the spatial interference pattern of the scattered light (Bachalo et al. 1986, Bachalo et al. 1983). These techniques have been utilized for many years and have been applied to many different applications from simple combustion studies (Seyfried et al. 2006) to complex flow studies (Meyer et al. 2005). Mie scatter, as it relates to fuel studies, have been paired with fluorescence techniques in fundamental spray studies (Jermy et al. 2000), combustion engine applications (Davy et al. 2000, Stojkovic et al. 2001), and gas turbine combustors (Lofstrom et al. 1996, Lofstrom et al. 2000).

2.3.2 Phosphorescence Techniques

Phosphorescence is slightly more complex than fluorescence. Due to the increased complexity of the adjacent energy level, the decay lifetime from that energy level is slower. Work has been done to quantify this decay time and has been shown to be near 1μs (Borkman et al. 1966, Wilkinson et al. 1963, Bogan et al. 1991) while others show this decay lifetime to be about 30 times longer (Haas et al. 1985, Emrich et al. 2000, Bortolus et al. 1986). It should be noted that the fuel used in these experiments was acetone that was tested in conditions that did not resemble typical fuel-air PLIF conditions. The acetone was prepared in freeze-pump-thaw cycles to remove contaminant gases (Bortolus et al. 1986, Pischel et al. 2001). In addition the phosphorescence signal has been proven to be quenched when interacting with oxygen (Lozano 1992). This suggests that the signal discussed previously in a fuel vapor-air mixing spray is produced from fluorescence alone. Work done at the laboratory scale does suggest that phosphorescence can contribute signal in regions that have not yet been quenched by oxygen, such as liquid droplets. There is also work that

has been done that supports this claim and furthers it by saying that under certain conditions, such as pressurizing the liquid acetone with N_2, elevated phosphorescence signal levels as compared with that not pressurized can be acquired (Richie et al. 2004). Work done previous to this by Bazile et al. (1995) tried to characterize the combination of these fluorescence and phosphorescence signals and suggested that the signal level from a liquid droplet may not be linear past some critically sized droplet due to large amounts of absorption by the droplet. More characterization work has been done such as Tran et al. (2005) but little of this work deals with high speed sprays or sprays of commercial fuel, or both.

CHAPTER 3. EXPERIMENTAL SETUP

The purpose of Chapter 3 is to provide a basic understanding of the experimental equipment, setup, and methods used in the subsequent research. Section 3.1 describes the general objectives of the entire setup up for each of the applications. Once the objectives are understood it is possible to break down the differences and similarities for both of the laboratory and test-cell setup. Section 3.2 breaks down the entire experimental setup into each of its components and addresses the need and function of these components. Section 3.3 deals with the data collected in a flow tunnel to simulate a test-cell application and each of its components detailing differences to that of the laboratory experiment.

3.1 Objectives of Laboratory Setup

Section 3.1 describes the objectives of the laboratory and test-cell setup. It is always desired when looking at global properties of sprays to not disturb the spray to be studied. These disturbances can lead to a collection of non-representative data. While this is accomplished in different ways, both setups use laser diagnostics, specifically fluorescence, phosphorescence, and scattering techniques to cause excitation and generate signal without physically or chemically disturbing the spray. Due to elevated temperature and pressure conditions, the test section was enclosed, whereas the laboratory testing was done at atmospheric conditions.

In addition to not disturbing the spray, it is also important that the experimental setup is able to distinguish between the different signal types and can accurately collect each signal at the correct time. Due to test section complexities, having optical components such as a dichroic mirror that is capable of passing certain wavelengths of light while reflecting others assisted in

the data collection. This was not the case in the laboratory setup where optical access was available from both sides of the spray.

Lastly, it is important that the timing scheme within the experimental setup is capable of being modified. In order to balance signals and collect the right pulse of light at the correct time requires a bit of adjustment for a given experiment. Without the advantage of being able to carefully adjust the timing of each event and exposure it would be nearly impossible to acquire representative data.

All of these topics, such as optics used, timing, signal types, etc., are discussed later in Sections 3.2 and 3.3 in greater detail.

3.2 Components for Laboratory Experiment

Section 3.2 describes the main components of the experimental setup that was responsible for all data collection on laboratory setup. These main components can be broken down into four main subsections. These sections are laser equipment to produce a laser beam, beam optics to align and condition the beam, the camera system to collect data, and the test section where the experiment is run. These items will be described in greater detail in the following subsections

3.2.1 Laser System

This subsection details the Nd:YAG laser system used for all experimental work. The system was comprised by two main components. First, the Nd:YAG laser itself which created the first laser beam of collimated light with an initial wavelength of 1064nm. Second, the frequency

doubling units which doubled the frequency of the light emitted from the Nd:YAG from 1064nm to 532nm and again in another unit from 532nm to 266nm.

The Nd:YAG is a solid-state laser and is named according to the lasing medium which is used. This lasing medium is neodymium-doped yttrium aluminum garnet ($Nd:Y_3Al_5O_{12}$). Nd:YAG lasers are optically pumped using a system of flashlamps or photodiodes and typically emit light with a fundamental wavelength of 1064nm in the infrared light spectrum. Nd:YAG lasers also have the option to be operated in a continuous or pulsed operation. Pulsed operation, achieved by activation of the Q-switching mode which inserts an optical switch into the laser cavity that waits for a maximum population inversion in the neodymium ions before it opens, was used in the experimental setup to create discretized, high-energy quantities of light. These pulses of high-energy, 1064nm light are then frequency doubled to 532nm using a Type II crystal with about 50% conversion efficiency. After passing through a few mirrors, a wave plate and a thin film polarizer, seen in Figure 3, the beam is then routed through a second frequency doubling unit.
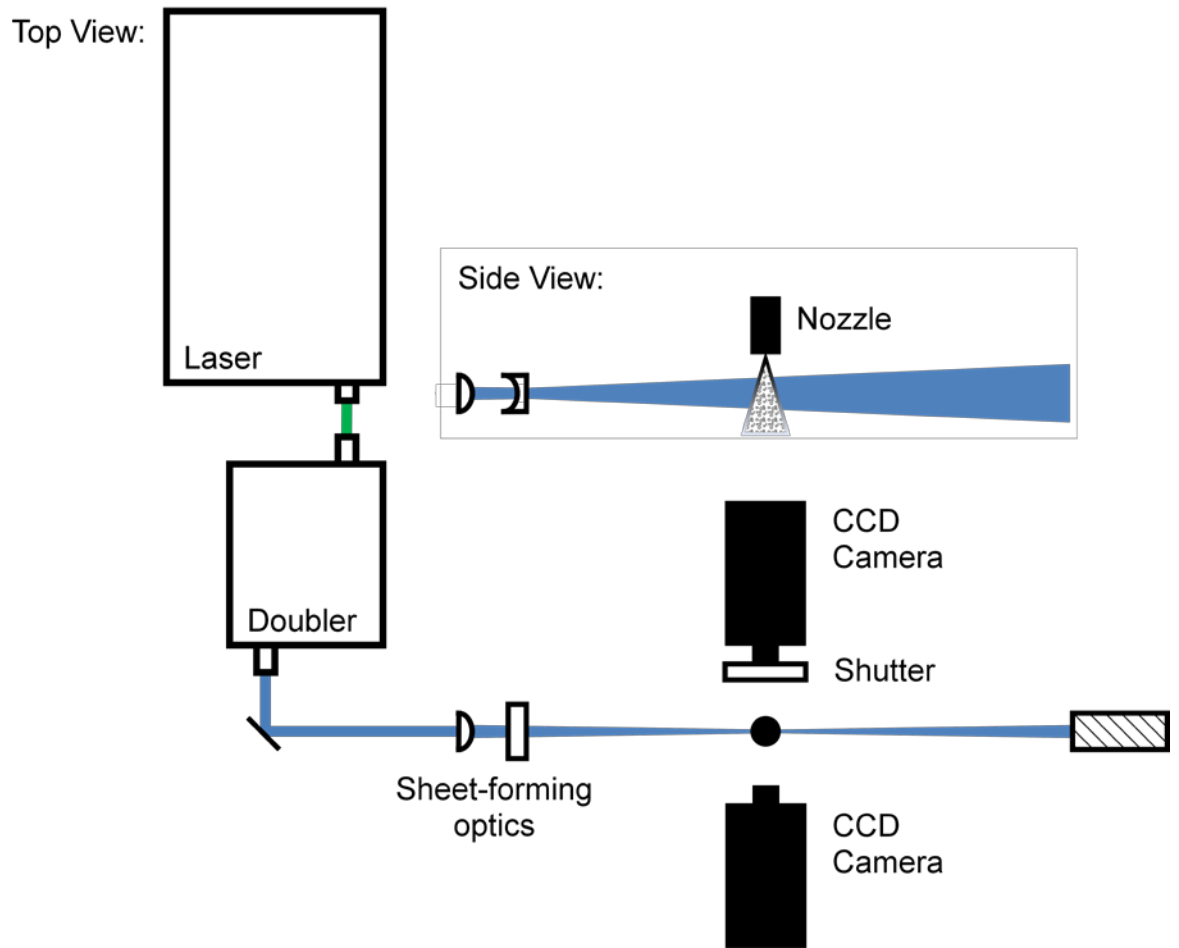
Figure 3: Schmatic of PLIF setup implemented in the laboratory setup.

This doubling unit contains a nonlinear, BBO crystal with output at roughly twice the frequency and half the wavelength, and therefore twice the energy of the initial photons. Once this doubling process has taken place for a second time the original 1064nm wavelength light has been frequency quadrupled to the required 266nm wavelength light that can effectively excite the fuel. The maximum conversion efficiency of the second doubling process in around 10% due to the incident wavelength. This ND:YAG laser system, capable of producing 1J per pulse in its fundamental wavelength of 1064nm, 400mJ per pulse in 532nm, or 13mJ/pulse of 266nm UV

light, was operated at peak power and at 10Hz for all ISU related experimental applications. Each of these pulses ranged from 10ns to 12ns in duration and the beam profile, while assumed to be Gaussian, can accurately be described by its transverse electric magnetic modes as TEM$_{00}$.

3.2.2 Optical Layout

This subsection details the components of the optical train responsible for conditioning the beam so that it may be effectively passed through the test section for data collection. For the laboratory setup it was desired to have a vertically-aligned sheet to pass through the test section. This laboratory setup can be seen in Figure 3. After the doubling unit, the beam was aligned through two conditioning optics to expand the beam from a 6-mm diameter round cross section to a tall thin sheet. The first conditioning optic is a plano-convex, UV fused silica, spherical lens with a focal length of +750mm. This caused the 266-nm beam to converge down to just a point of light at roughly 750mm from the curved side of the lens. The second optic is a plano-concave, UV fused silica, cylindrical lens with a focal length of -75mm. This lens caused the beam to diverge in only a single direction. When these two optics were aligned and spaced correctly it is possible to create a laser sheet of pre-specified dimensions that is converging horizontally and diverging vertically. This beam, as it passd through its focus under the spray nozzle, had a minimum thickness of roughly 800μm and a height of about 115mm. It should be noted that the laser sheet was slowly expanding as it passed through the probe volume, which leads to an energy variation of less than 10% of the total beam energy.

After passing through the test section and out of the testing chamber, the beam is safely collected by one of two methods. High energy density beams were collected in a beam dump

while lower energy density beams were allowed to strike a non-reflective, non-ablative surface to harmlessly dump the energy.

3.2.3 Test Apparatus

This section details the test apparatus, composed of the spray chamber, the manifold nozzle system, and the fuel delivery system.

3.2.3.1 Spray Chamber

The spray chamber was constructed out of a large HDPE container standing roughly 1 meter high and roughly 0.5 meters in diameter. The chamber had 25cm diameter openings in the side of the chamber, spaced 90 degrees from one another, which served as the optical access to the spray on the inside.

The laser beam exited the chamber through a slit at the back of the chamber to avoid scatter off of the inside of the chamber. This chamber was then positioned so that the region of interest matched the height of the laser sheet.

3.2.3.2 Manifold and Nozzle System

The spray manifold was constructed out of a 6061 aluminum disk. It was 100mm in diameter and 25mm thick. Detailed drawings for the disk can be seen in the attached appendix. Four ¼"-20 holes were tapped and used to bolt the manifold down to the HDPE cover of the chamber. A silicone rubber gasket was placed between the cover and the aluminum manifold to prevent leaks. In the middle of the disk on each side, holes were tapped to receive one of two items. One side received a plastic coupling that had a quick disconnect fastener which was able to accommodate a 10mm plastic tube. The other tapped hole received a pipe nipple. This pipe

nipple was approximately 100mm long and had a pipe coupling attached to the free end that could receive the nozzle to be tested. The length of the nipple was chosen so that when entirely assembled, the tip of the nozzle just appeared in the very top of the region of interest of each camera.

Nozzles tested in the laboratory-scale spray were purchased from Allspray, LLC. or donated by Delavan Spray Technologies and Goodrich Turbine Fuel Technologies. The nozzles from Allspray were manufactured from brass bar stock and were intended for various industrial duties such as water cooling, air and gas washers, scrubbers, product washing, dust control, cooling and quenching spraying, or fire control. These nozzles were selected for different reasons including simple one piece construction, compatibility with liquid fuels, wide variety in spray shape, availability of flow rate and pressure ratings, as well as accuracy and consistency in producing medium to small, ~100 micron diameter, droplets. This was an important characteristic in the ability to test signal levels between liquid and droplets. If the droplets produced were too large, fluorescence and scattering signals would have been drastically higher and little vapor would have been produced. Nozzles for the laboratory experiment took one of two main shapes. They were either a flat spray or a hollow cone spray. Graphic depictions of each of these sprays can be seen in Figure 4 along with the corresponding nozzle responsible for each of the shapes.
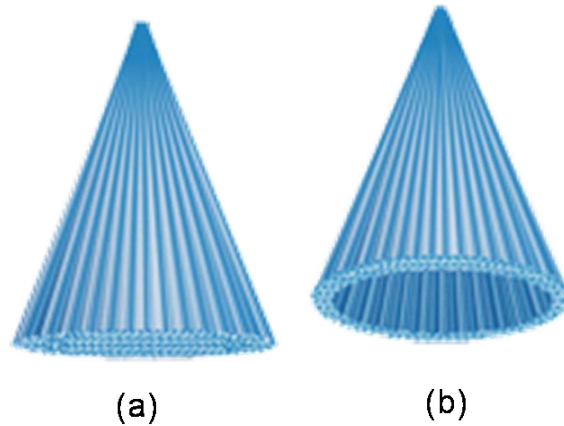
Figure 4: Graphic representation of the two different spray types used in PLIF measurement in the laboratory setup. Shown are the flat spray in (a) and the hollow cone in (b). Retrieved from http://www.allspray.com 06 Oct 2008.

In addition to varying the shape of the spray, fuel flow rates were varied within each spray shape from a minimum of 0.76 lpm to a maximum of 7.57 lpm based on a 275.8 kPa supply pressure. The nozzles received from Delavan Spray Technologies and Goodrich Turbine Fuel Technologies were originally constructed to inject home heating oil into a furnace for a home heating application. As before, these nozzles are constructed from brass and produce a hollow cone spray. The flow rate availability was slightly more constrained providing flow rates between 0.0632 lpm and 0.1264 lpm based on a 689.5 kPa supply pressure.

3.2.3.3 Fuel Delivery System

It was initially desired to have a system that could recirculate the fuel to reduce down time between tests and ease of use, but due to the corrosive properties of liquid acetone and jet fuel, it was determined that this would not be possible and still achieve the slow and steady liquid flow rates desired. It was decided that charging a pressure vessel that was holding the liquid fuel to be sprayed with a bottle of 99.9% pure nitrogen would provide the best solution. This method, shown in Figure 5, would allow for a consistent flow rate that depends on the discharge pressure

from the tank and alleviate any flow rate inconsistencies, such as surging, from a positive

displacement pump.
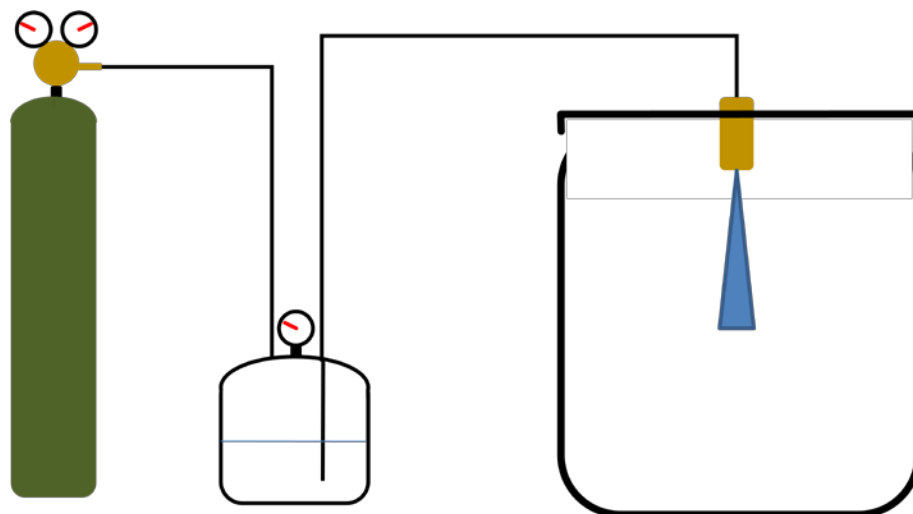
Figure 5: Laboratory spray schematic. Pressureized cylinder used to pressure a stainless steel vessel with a long dip tube that supplies the nozzle manifold at the test section.

In addition, when the liquid fuel was placed in a stainless steel pressure vessel, there were fewer

wetted parts, and charging the liquid fuel with nitrogen reduces oxygen partial pressure, thus

increasing phosphorescent signal from the liquid phase. The drawback to this system is the

additional time required to charge the vessel before tests can be run. The pressure vessel had a

long tube that dipped down into the liquid and, when this vessel was charged, can only dispense

the liquid fuel until the liquid level dropped below its minimum height. The vessel was also

equipped with quarter-turn ball valves at the inlet outlet, a overpressure pop-off valves for

immediate stopping, starting, and general safety of operation.

3.2.4 Camera System

This section details the camera and camera systems used in data collection. Due to the

fact that there are three different signals to be collected, Mie scattering, fluorescence, and

phosphorescence and at least two of these signals occurred at the same time, multiple cameras had to be used. Two cameras were used to image from both sides of the planar sheet, as enabled by the two optical access ports. These cameras had a large percentage of their region of interest overlapping, and were perpendicular to the laser sheet. The first was a PIV camera manufactured by PCO Imaging, and the second was a spectrometer camera sensitive to UV light manufactured by Andor Technologies. The PIV camera was a PCO Imaging CCD camera, model PCO 4000s. It had a physical resolution of 4008 by 2672 pixels with a pixel size of 9 by 9μm, a baseline readout noise of 11 e- rms at 8Hz, and a peak quantum efficiency of 50%. When coupled with its driving software, CamWare v.2.21, also produced by PCO, this CCD camera was capable of capturing two frames of variable exposure length that are separated in time by 180 nanoseconds. The inter-frame camera jitter 20ns, as measured experimentally. When timed correctly, it was possible to capture fluorescence of the liquid fuel and a weaker phosphorescence signal in the first frame and only phosphorescence signal in the second frame. The second camera was a Newton model spectroscopy camera manufactured by Andor Technologies, model number DU940-BU. It had a physical resolution of 2048 by 512 pixels with a pixel size of 13.5μm, a baseline readout noise 11 e- rms at 2.5Hz, and a typical quantum efficiency of 25%. The Andor camera, when equipped with a UV camera lens was able to capture Mie scattering signal from the liquid droplets. A UG 11 Schott Glass color filter was used so that the Andor camera would only detect UV scatter rather than fluorescence or phosphorescence.

3.3 Test Cell Application Components

Section 3.3 details the components used for the test cell application experiments. It will describe the purpose of each of the components and note differences between that the test cell application and laboratory-scale setup used.

3.3.1 Laser

The laser system used in the test cell application was nearly identical to the laser used in the laboratory setup, but it produced a slightly higher energy per pulse of ~140mJ/pulse after the fundamental wavelength had been quadrupled.

3.3.2 Optical Layout

This subsection details the components of the optical train responsible for conditioning the beam so that it may be effectively passed through the test section for data collection. The goals of the optical layout were the same as those discussed in the laboratory setup. It was desired to have a tall, thin sheet to pass through the test section that was wide enough to capture the entire spray characteristics and thin enough to be able to completely resolve small structures within the laser sheet. One difference to the optical train was that the final optics need to be mounted to a traversing stage that allowed the optics and cameras to move and image different planes of the spray without changing the focus of the cameras or the geometry of the laser sheet. To accommodate this, it was necessary to add a third lens to the sheet forming optics to ensure that the laser sheet width was constant throughout the beam path approaching the spray. As shown in Figure 6, the first optic in this cylindrical telescope would cause the beam to focus in a given direction and then, with the second optic to recolimate the beam at the desired focal length,

created a constant-width thin laser sheet that can be passed through the test section. When

combined with a cylindrical lens with a very long focal length aligned so that it operated in the

opposite direction it created a very thin 12cm sheet as the beam passed through the test section.
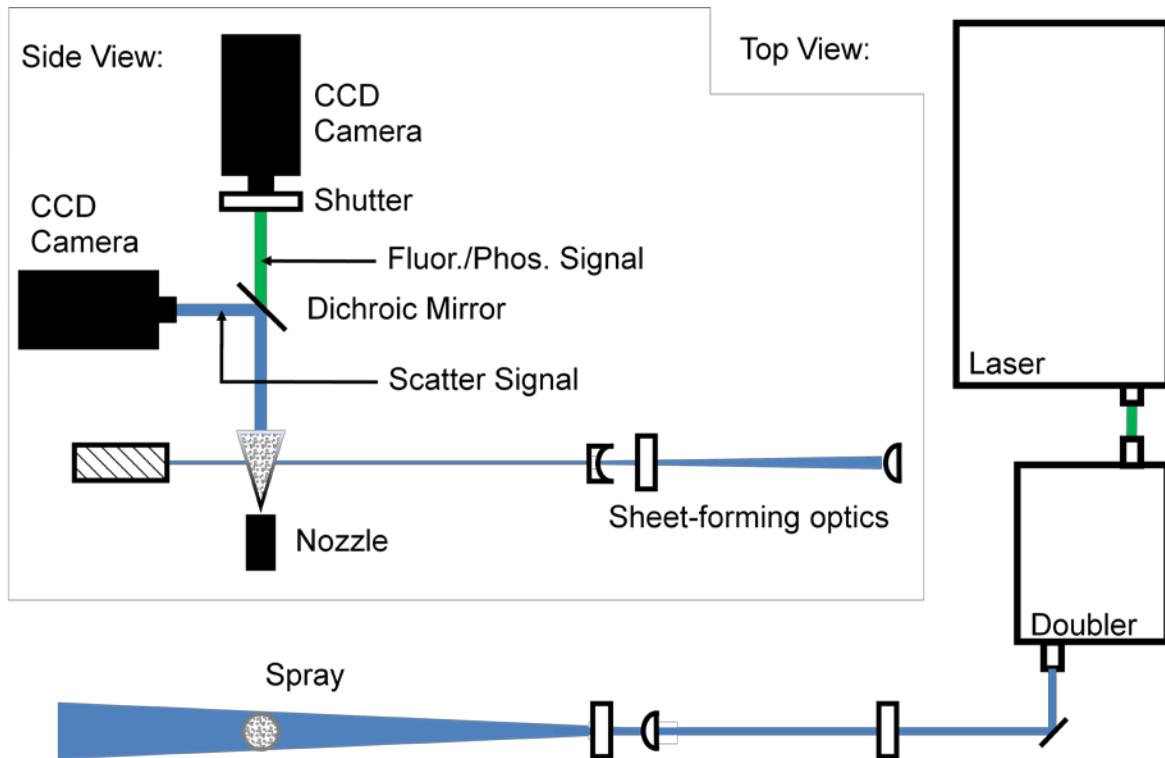
Figure 6: Schematic of first optical setup for PLIF measurements for a test cell application. This setup, passing a horizontal beam through the test section, is responsible for creating the 'donuts' of signal for each spray condition.

Due to the two different planes of the spray that were to be collected, two different

optical layouts had to be used. The first, shown in Figure 6, was constructed so that the beam that

passed through the test section was parallel to the ground and normal to the spray direction. In

the second, vertical configuration, the laser sheet was oriented along the spray direction.
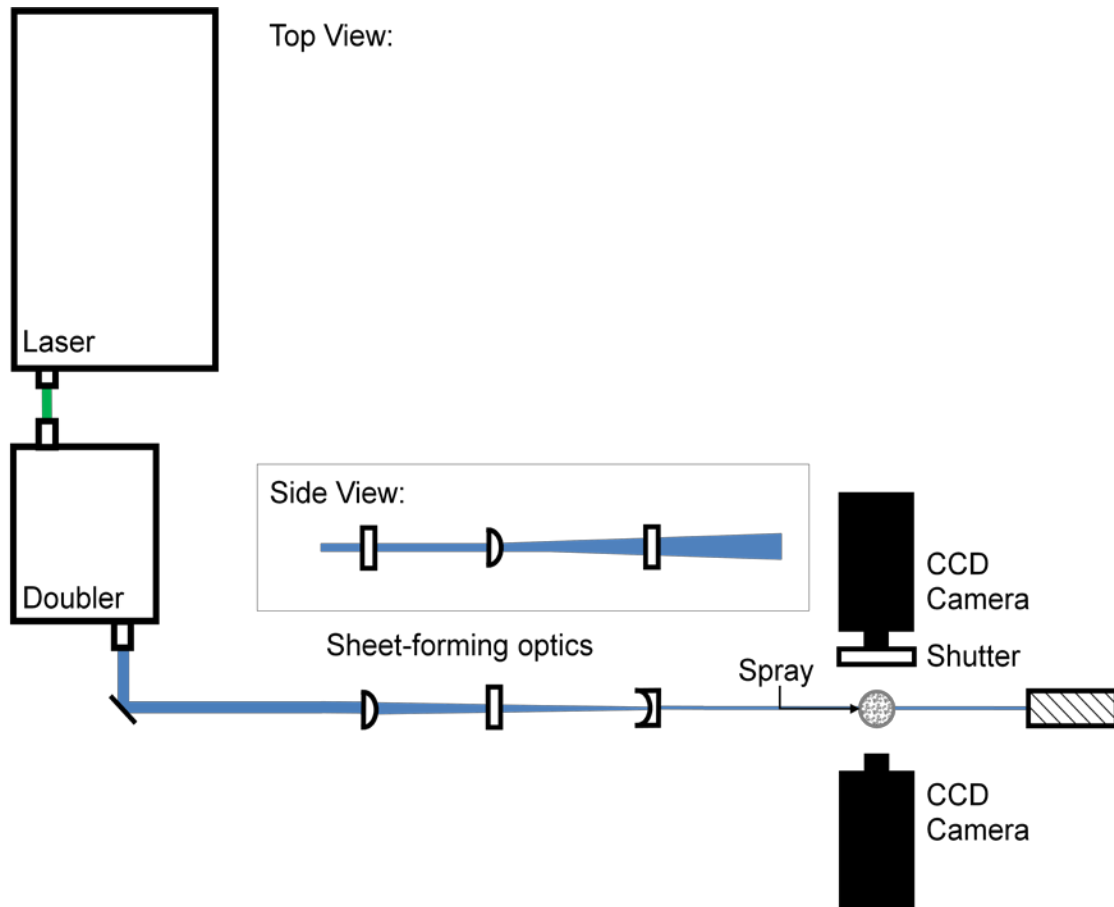
Figure 7: Schematic of second optical setup for PLIF measurements for a test cell application. This setup, passing a vertical beam through the test section, is responsible for creating the 'V' of signal for each spray condition.

3.3.3 Test Section

This section details the test section used for the test cell application. This test section, designed to test multiple temperature and pressure-related conditions for a variety of different projects, was inherently more complex. It consisted of a rectangular steel passage with an injector manifold protruding from the bottom. Optical access was available from four sides surrounding the manifold using fused silica windows. This test section allowed investigations of sprays with heated and unheated crossflows. Because of the size and complexity of the test section, it was

necessary to leave it stationary and adjust the entire optical setup to image different planes of data. Shown in Figure 8 is an image of the mirrors and sheet forming optics leading to the test section.
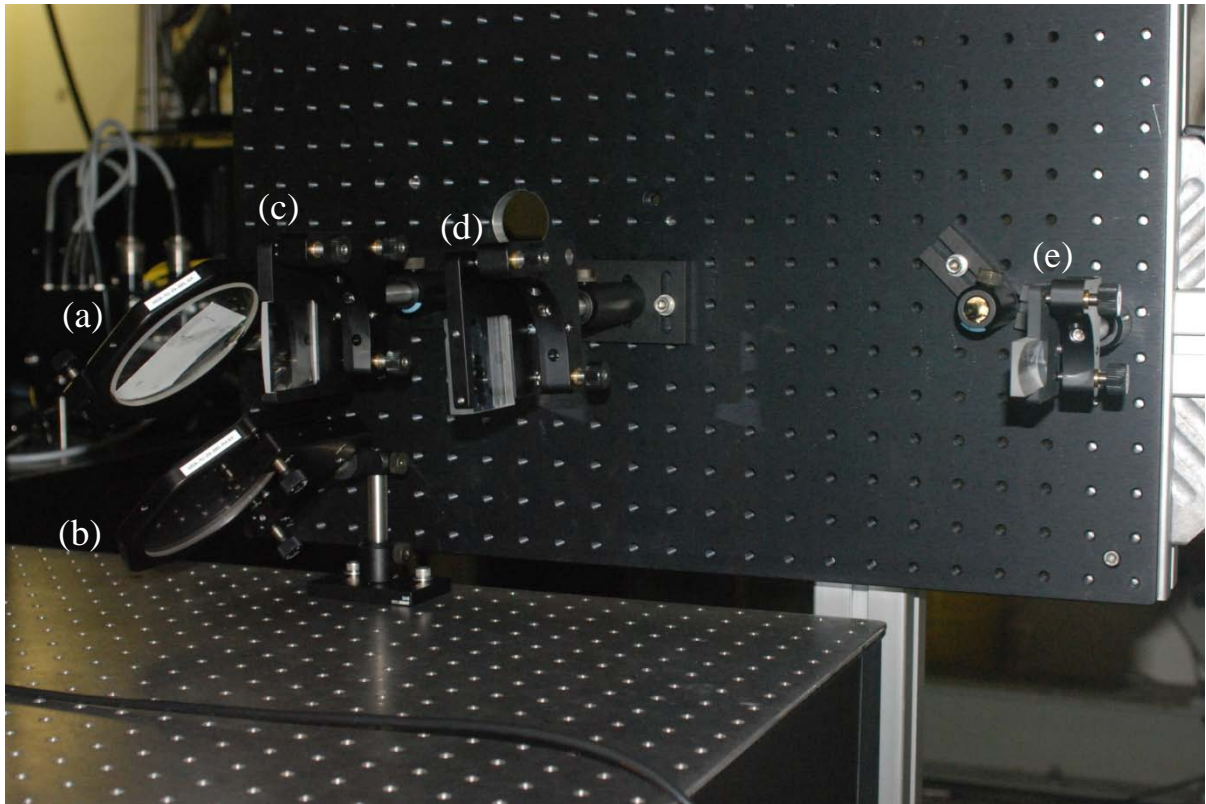
Figure 8: Image of sheet forming optics mounted on a breadboard that is mounted to a large traverse stage. This mounting system enables imaging of multiple planes within the spray without changing sheet geometries. (a) & (b) 12cm mirrors that form a periscope that allows for vertical translation of the transverse stage. (c) First optic in the telescope. (d) Cylindrical lens with very long focal length that cause beam to become very narrow. (e) Last optic in telescope that recolimates the beam.

The test cell setup also used a much more sophisticated control system to monitor and manage all aspects of each test. The items handled from a main control room include but are not limited to fuel flow rate, ambient temperature, crossflow velocity, crossflow temperature, and ambient air temperature. Due to the added levels of complexity, this facility required full-time staff for operation, and the details related to the control system will not be discussed here.

3.3.4 Camera System

This section details the camera and camera systems used in data collection for the test cell application. Due to the two different optical layouts to collect the various spray orientations there had to be two different camera setups to accommodate these optics.

For the first setup, when the beam was parallel to the floor, it was necessary to pass all three signal types out of a single glass window and then use a dichroic mirror to split the signals according to signal wavelength for the respective cameras. The dichroic mirror had a UV reflective coating on one side and had and an anti-reflective coating on the other side to prevent a double image on the camera chip.. This allowed the UV light from the scattering signal to be reflected to the UV sensitive (Andor Technologies) camera, shown to the left in Figure 9. The visible light from the fluorescence and phosphorescence signals is passed through the dichroic mirror and to the dual-frame (PCO) camera shown on the upper right in Figure 9. Due to the mirror the scattering images collected by the UV sensitive camera is flipped along a horizontal symmetry line and must be corrected to spatially match the fluorescence and phosphorescence images. Image correction is discussed later in Section 4.
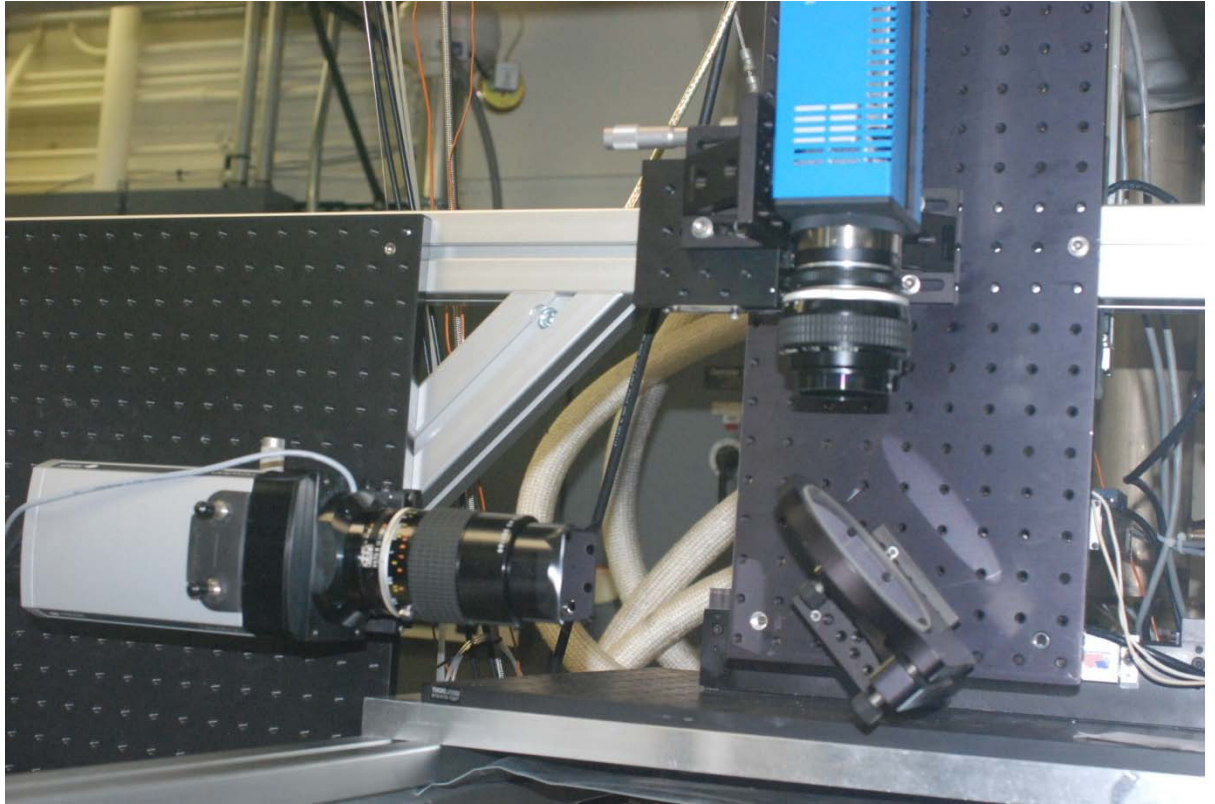
Figure 9: Imaging setup for the first optical setup. Signal, from the test section (bottom of image), comes up and contacts the mirror, and depending on the wavelength of the signal is directed to one of the cameras. The Mie scatter signal has a shorter wavelength and is reflected by the mirror to the Andor camera on the left of the image. Both fluorescence and phosphorescence signals are longer and pass through the mirror into the PCO camera at the top of the image.

The second camera setup used to collect data in the test cell application is responsible for vertical-slices of data. This setup was similar to that of the laboratory-scale setup. As shown previously in Figure 7, the beam passed through the middle of the test section and in a way that allowed the planes of data created by this laser sheet to be optically accessible to the cameras on each side of the test section. As before, the cameras will not be spatially matched as collected. One set or the other must be flipped about a vertical symmetry line to correct the images.

3.4 Experimental Procedure

Section 3.4 deals with the experimental procedure used for both the laboratory-scale and test cell applications. This section includes discussions of the various signal types, timing of events, and problems encountered.

3.4.1 Signal Types

This subsection details the signal types of all events related to the experimental setup, including Mie scattering, fluorescence, and phosphorescence.

The first signal collected is Mie scattering. This signal was produced from the laser sheet striking the liquid droplets and scattering off of the droplets in all directions. The scattered signal is at the same wavelength as that initially incident on the droplets. Due to the fact that the original beam needs to come into contact with the droplet liquid-gas interface for this to occur, the Mie scattering signal is only produced from droplets and not vapor. It is also important to note that scattering signal can only be produced when a beam is present and contacting a droplet and thus will only last as long as the original (~10-ns) laser pulse.

The second signal collected is fluorescence, which was emitted from both droplets and vapor when each is excited by the 266nm laser energy. It differs from Mie scattering in the fact that the excited liquid or vapor has a relaxation time for decay back to its original energy state. This relaxation time is of the order ~100ns long, and thus these excited molecules can emit light for a very brief time after the pulsed excitation source is removed.

The third signal collected is phosphorescence, which is derived from the decay of energy states that are excited from internal energy transfer processes within a molecule. While being very similar to fluorescence, phosphorescence has the major difference in that the relaxation time

of the excited molecule is much longer and allows the molecule to continue to emit light ~300ns

or longer after the exciting energy source has been removed. The phosphorescence signal is

highly quenched by oxygen so that the signal from the liquid phase is much stronger than signal

from the vapor-phase in an oxygen-based environment. Lifetime decay charts of fluorescence and

phosphorescence can be seen in Figure 10.
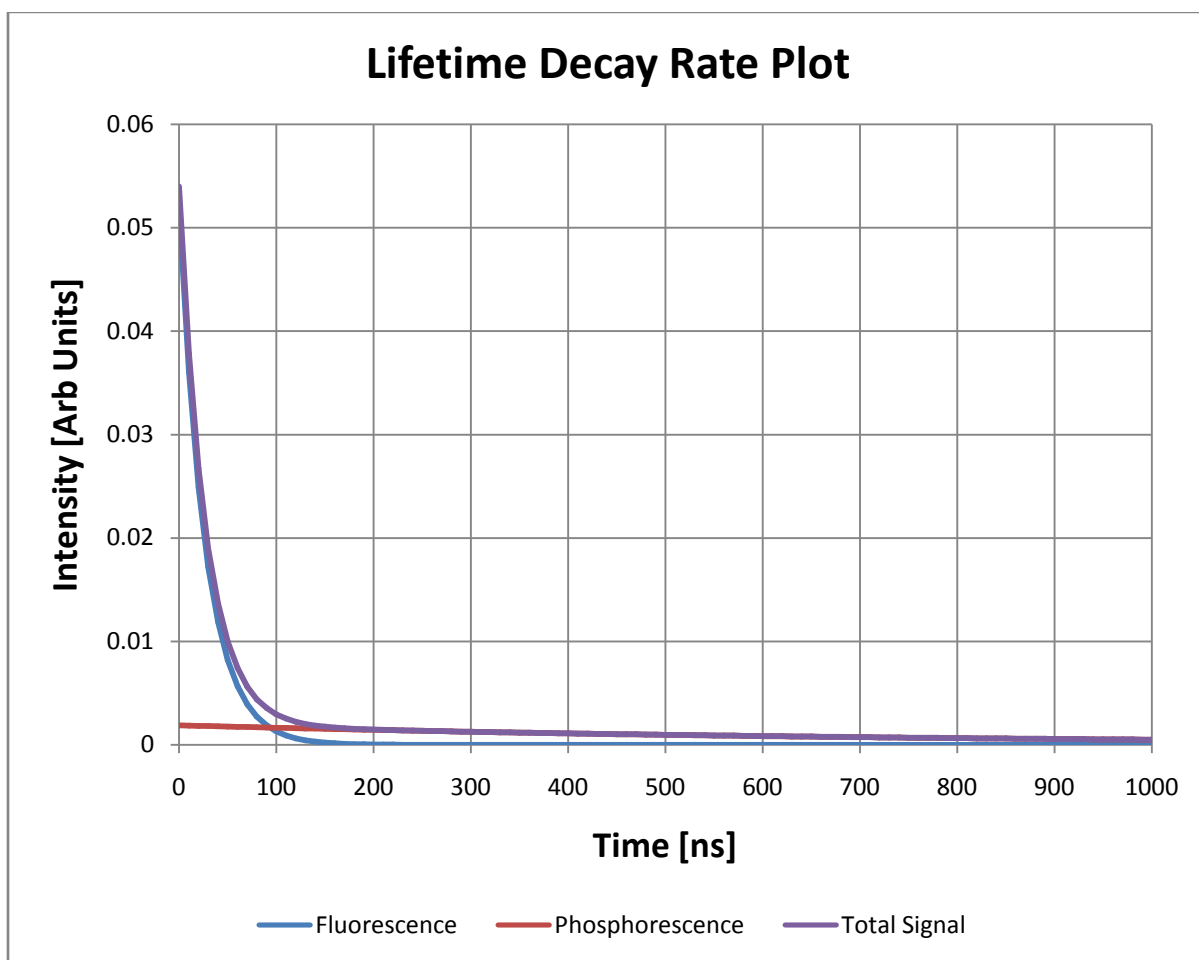
Figure 10: Lifetime decay chart for both fluorescence and phosphorescence.

This plot shows the total signal, shown in purple, as being comprised of the sum of two related signals. To generate this data, jet fuel was placed in a sealed cuvette and struck with 266nm, 100mJ/pulse laser light. This light, when incident on the cuvette, caused fluorescence, phosphorescence, and scattering events to occur. These events were captured by a photodiode to trace the emitted light intensity in time. Since only fluorescence and phosphorescence are to be measured, a glass lens with a very long focal length (~1000mm), was placed in front of the photodiode. This acted as a filter and does not pass the UV scatter. It was assumed that the total signal would be comprised of two different exponential decay functions; one for fluorescence and the other for phosphorescence. When the data was fit to the sum of two decaying exponentials of the form shown in Equation 1 it was possible to note the time constants and relationships between the two different exponentials.

$$Total\ Signal = A_1 \cdot e^{-t_1} + A_2 \cdot e^{-t_2}$$

Equation 1: Structure of two competing decaying exponentials.

For the first decaying exponential, contributed from the fluorescence event, the time constant was 27.8ns and the pre-exponential constant was 0.0521 while the second decaying exponential, contributed from the phosphorescence event, had a time constant of 749.5ns and a pre-exponential constant of 0.0018. This demonstrated the previously mentioned concepts dealing with fluorescence and phosphorescence lifetimes and intensity magnitudes. With a smaller time constant than the phosphorescence, fluorescence signal had a much, much shorter lifetime. Conversely, fluorescence signal had a much larger pre-exponential constant and therefore had a much greater overall intensity than the phosphorescence signal. In order to effectively collect each type of signal it was necessary to have a detector that was capable of

capturing elevated intensities for short amounts of time for the fluorescence and a detector that was capable of resolving reduced intensities for a much longer time for the phosphorescence signal. Due to the overall reduced level of the phosphorescence signal as compared with the fluorescence signal increased levels of signal detection error is noticed. This is also seen in the spray studies to be discussed later.

3.4.2 Timing

This subsection deals with the timing of all events to enable the signals to be captured. One of the main tasks of setting up the correct timing to each of the cameras to capture the different types of signal was having all cameras collect the correct laser pulse. For both the laboratory and the test cell application setup the laser responsible for exciting the liquid fuel was being run at 10Hz. Due to limitations within the camera software and readout times for each of the camera CCD chips the cameras could only sample at 0.5Hz. This means that once the cameras exposed and collected data from one of the laser pulses 19 laser pulses were emitted and passed through the test section, exciting the fuel, before the cameras were ready to sample again. This made it imperative to ensure that the cameras were all collecting the same laser pulse or correlations would not be able to be made between the signals for a given frame.

It was also important for the timing to place the laser pulse in the correct timing range within each of the camera frames to maximize the amount of each signal type. An example of this was seen when looking at the fluorescence and phosphorescence signal lifetimes. Since each of these signal types were to be collected by the same dual-frame camera, just in different frames, and each signal was started when the laser pulse was incident on the liquid droplets of fuel, it was important to have the laser pulse moved as far back in time in the 10ms exposure time of the first

frame to allow the phosphorescence signal to be maximized in the second frame. If the laser pulse were to occur at the beginning of the first frame both the fluorescence and phosphorescence signal would be captured in that first frame since the 10ms exposure time is much longer than either of the lifetimes of the signals. The actual timing envelope used in the laboratory setup is shown in Figure 11. The variable delay listed in the data summary is delayed from the end of the fluorescence image exposure. While not originally timed like this, the delay is mathematically simplified.
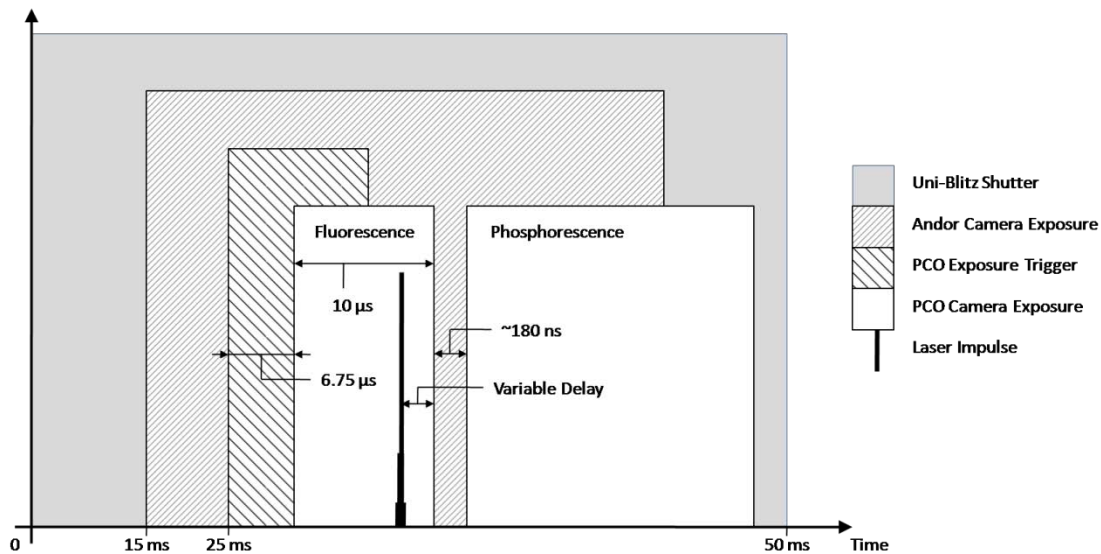
Figure 11: Timing envelope used in laboratory setup. Note: not to scale.

Less importance was given to the timing of the Andor camera responsible for collecting the Mie scattering signal. This can be attributed to the fact that this signal was only present when the exciting laser pulse was present and the Andor camera was only responsible for collecting this single signal. The exposure time for the Andor camera was set to 20 ms and the beginning of the frame was set to roughly 10ms before the laser pulse arrives at the test section. With the very short duration of the laser pulses and the long frame length of the Andor camera, it was

guaranteed to capture the laser pulse desired, although the shutter within this camera must be timed to collect signal from the same laser pulse as the dual-frame camera.

The other item that required correct timing was the UniBlitz shutter used in front of the PCO camera. This shutter, which ensured only one laser pulse was captured per camera exposure, was set to have an open time of 50ms, which was much longer than the actual exposure time of the PCO camera but still shorter that the time between laser pulses. In addition the shutter was stated to have a 15ms open and close time which shortens the actual open time to roughly 40ms. With this in mind it was important that the shutter open time was centered about both of the exposures of the PCO camera to maximize signal.

3.4.3 Challenges Encountered and Changes to be Made

This subsection details the experimental challenges encountered as each of the experiments were setup, run and analyzed. One of the main difficulties that occurred in each of the experimental setups was the inter-frame camera jitter of the dual-frame camera. This jitter, which caused the time between the fluorescence and phosphorescence frame to vary, caused a problem in accurately capturing each of the signal types. This jitter varied from 5 to 20ns. If this reached its maximum value for a given exposure it would greatly reduce the amount of phosphorescence signal received because the phosphorescence signal is rapidly decaying during this time and the longer the jitter, the more of the signal is not captured. Limitations within the camera hardware and software prevented the jitter from being eliminated from the setup, and corrections must be employed in image processing to account for this effect (see Section 4.1).

Jitter was also seen in the start time of the fluorescence image. Any jitter noticed here had a smaller negative effect on the result because this jitter was much smaller and easier to eliminate

by having a more accurate controlling system that is responsible for starting the image. Effects from this type of jitter were similar to those of the inter-frame jitter discussed above.

Other problems such as beam quality and optical alignment affected the experiment, but not as drastically as the aforementioned issues. Steps should be taken to correct each of these issues for future experimentation.

CHAPTER 4. RESULTS

Selected data from the experimental measurements are presented below, along with a detailed discussion of the results. Additional data is provided in the Appendix. To begin, the image processing procedures are detailed in Section 4.1. Results of the laboratory-scale experiments are presented in Section 4.2, focusing on a comparison of fuels and timing techniques to maximize signal levels between fluorescence and phosphorescence images. Results of the test-cell experiments are discussed in Section 4.3. This section is broken down into a number of different imaging conditions representing changes in fuel flow, crossflow, timing issues, temperature, image or laser sheet orientation and height effects on spray images and signal intensity.

4.1 Data Processing and Conditioning

The data processing procedures used for correcting and comparing the images from fluorescence, phosphorescence, and Mie scattering techniques are described in Section 4.1. Each image is comprised of a number of different signals collected by the CCD chip of the camera. Ideally, signal interferences can be avoided using optical filters. In the case of fluorescence or phosphorescence, it is possible to block unwanted UV scattering by using a glass camera lens. Background scattering at the same wavelength as the detected signal must be removed in post-processing.

For each condition that data was collected, a background set of images was collected to record general ambient light in the room, lights from instrumentation, etc. It was not possible to collect the background images at the same time as the actual data so each background was collected promptly after each data set. Background images collected for each flow condition were

averaged together to form a single image that is representative of the entire data set. This averaged image is subtracted from each individual image for the same flow condition. Averaging of the background files was performed using a program entitled ImageConvert, which allows batch processing of certain image manipulations. Image mathematics and intensity scaling of data sets, as shown in Figure 12, was performed using WinView software, which is capable of experimental control, data collection, signal processing, and image statistics on entire images or regions of interest. Because of jitter in timing between the laser used for fluorescence/phosphorescence excitation and the interframe time of the dual-frame CCD camera, the relative intensity of fluorescence and phosphorescence signals required rescaling from shot to shot. Because both signals are proportional to droplet volume, variations in camera counts can be corrected using linear scaling from image to image to achieve comparable signals from each technique. Essentially, it is possible to artificially rescale intensity counts for a given image in post-processing to enable image subtraction. This is discussed later. Mie scattering signals, on the other hand, cannot be adjusted with a single scaling factor as the signal intensity will vary for each pixel depending on the droplet diameter. Hence, these images were scaled simply to allow features of the spray to be clearly visualized.
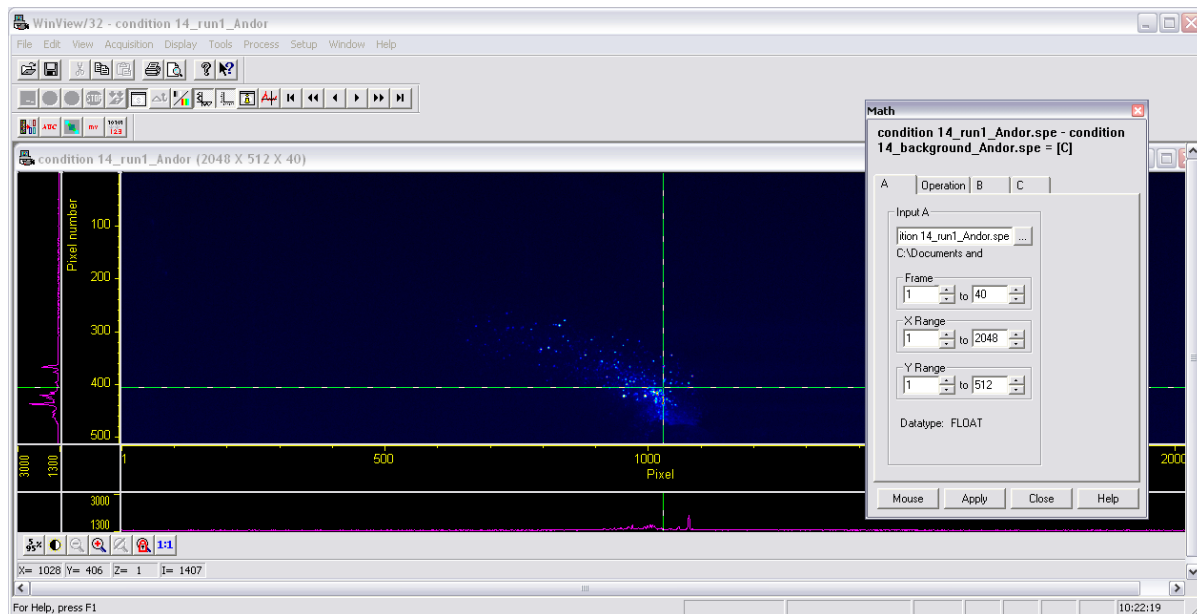
Figure 12: Screenshot of WinView with file loaded and image math window open. WinView was used to do all image math, except for averaging, to create the final signal shown in all data presentation.

4.2 Presentation of Laboratory Data

The data presented in Section 4.2 encompass a number of different test criteria for the laboratory-scale fuel spray, including flow rate and delivery pressure, camera delay sensitivity, and fuel type (acetone and jet-A).

4.2.1 Signal Intensity Dependencies on Flow Rate and Delivery Pressure

This subsection focuses on the relationship between flow rate and the delivery pressure of the fuel as it relates to processed signal level within the laboratory-scale spray. The fuel flow rate and pressure are varied by exchanging spray nozzles and supplying a charged fuel vessel with a higher or lower delivery pressure, depending on the condition to be tested.

The first comparison is made between two different nozzles that are designed for an in-home heating device such as a furnace. These two nozzles have the same delivery pressure of

689.5 kPa but differ in fuel flow rate. Presented as Test 1 and Test 2, both compared in Figure
13, these nozzles are capable of flowing 0.1264 lpm (gallons per hour) and 0.0632 lpm,
respectively. For the comparison each image pair was scaled to the same intensity, where the
range of counts (e.g., 0 to 3000) represents the minimum and maximum for the false color scale,
as noted in the figure.

Fluorescence
[0 to 3000]

Phosphorescence
[0 to 3000]

Mie Scatter
[0 to 13000]
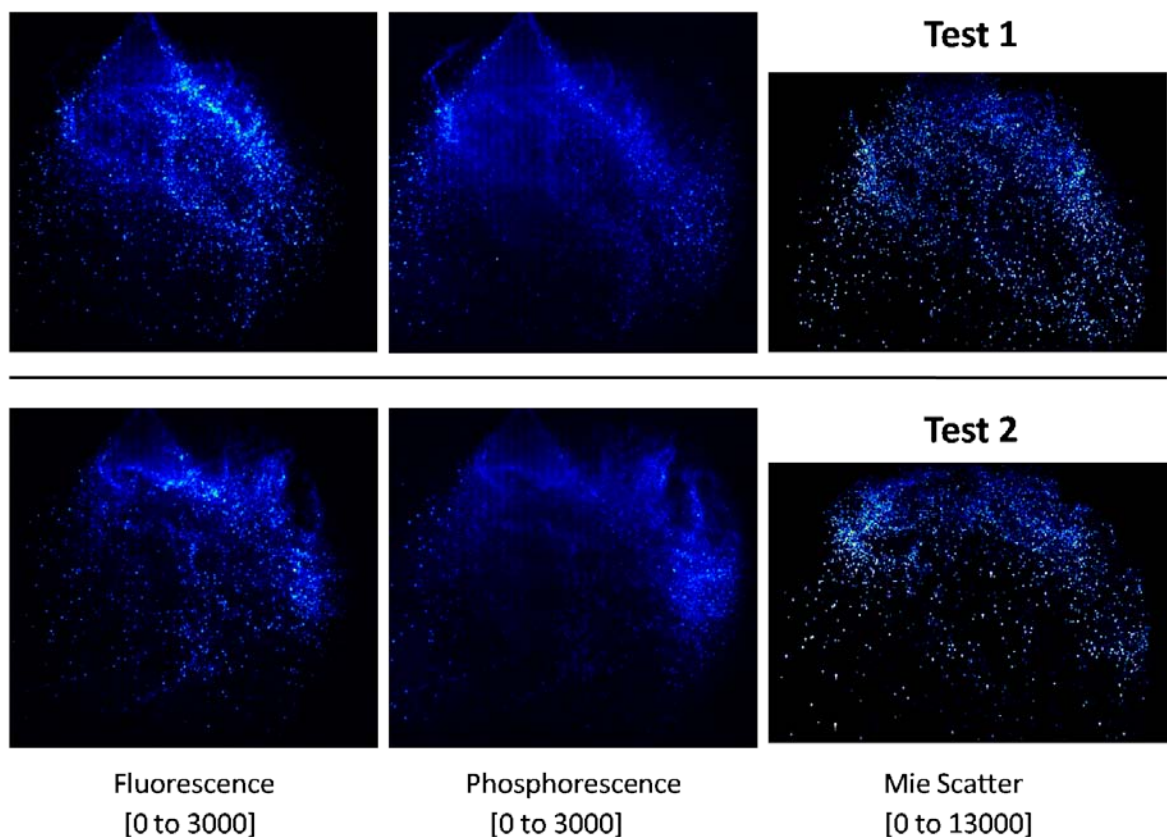
**Figure 13: Comparison of data collected in the laboratory setup, Test 1 and Test 2,
highlighting the relationship between an increase in fuel flow rate and measured signal
intensity. The nozzle in Test 1 is capable of flowing 0.1264 lpm @ 689.5 kPa while the
nozzle in Test 2 is capable of flowing 0.0632 lpm @ 689.5 kPa.**

A second comparison is made with a different type of nozzle that is designed for

industrial particle collection or cooling. These two nozzles have the same delivery pressure of

275.8 kPa but differ in fuel flow rate. Labeled as Test 6 and Test 7, both compared in Figure 14, these nozzles are capable of flowing 3.79 lpm and 0.76 lpm, respectively.
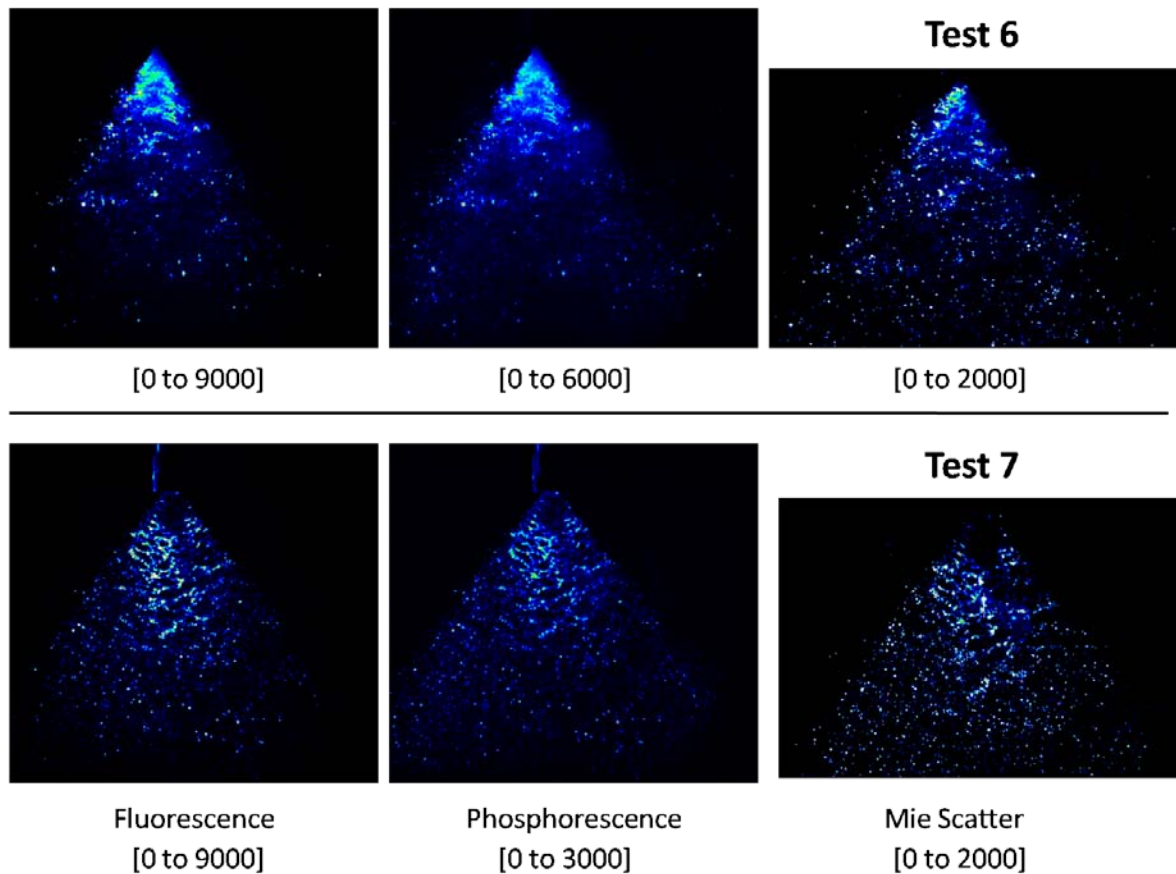
Figure 14: Comparison of data collected in the laboratory setup, Test 6 and Test 7, highlighting the relationship between an increase in fuel flow rate and measured signal intensity. The nozzle in Test 6 is capable of flowing 3.79lpm @ 275.8 kPa while the nozzle in Test 7 is capable of flowing 0.76lpm @ 275.8 kPa.

As expected, higher fuel flow rates lead to an increase in signal for fluorescence, phosphorescence, and Mie scattering in Figure 14, especially near the nozzle tip where the spray is somewhat dense. Under more dilute conditions in Figure 13, the spray does not appear qualitatively different for 0.0632 lpm as compared with 0.1264 lpm. It may be that for this

condition that the spray is comprised of a very fine mist and that the images are dominated by larger droplets that are not representative of the total fuel mass.

However, for both Figure 13 and Figure 14, it is clear that the fluorescence signals have broad regions of signal that may be interpreted as vapor, whereas the Mie scattering shows discrete points of light representing droplets. Hence, it may appear that this is an evaporating spray. However, the phosphorescence signals, which are sensitive mostly to the liquid phase, nearly match that of fluorescence. This implies that the fluorescence signals can be somewhat misleading and may be prone to effects of multiple scattering.

4.2.2 Camera Delay Sensitivity

This subsection focuses on the sensitivity of fluorescence and phosphorescence signals to the relative time with respect to the dual frame PCO camera. There is an inherent jitter between the laser event and the camera exposure. As discussed previously in Section 3, the laser excitation pulse should be as close to the end of the first exposure as possible while not overlapping into the second image collected shortly thereafter. A longer delay moves the laser pulse away from the end of the first exposure. This is easier understood when looking at Figure 11 above. The delay being discussed is represented as "Variable Delay" in the figure. It should be noted that due to timing issues, the "Variable Delay" is not shown to scale and that this delay can be much larger that shown in Figure 11.

Figure 15 compares three different conditions, all with a different delay. Test 12 has a relative delay of 40.1722ms while Test 13 and Test 11 add ten and twenty nanoseconds to this delay, respectively. The fuel used for all the timing tests was acetone as its characteristics are well known.

Test 11 **Test 13** **Test 12**

Delay = 110ms Delay = 100ns Delay = 90ns
[0 to 9000] [0 to 9000] [0 to 10000]
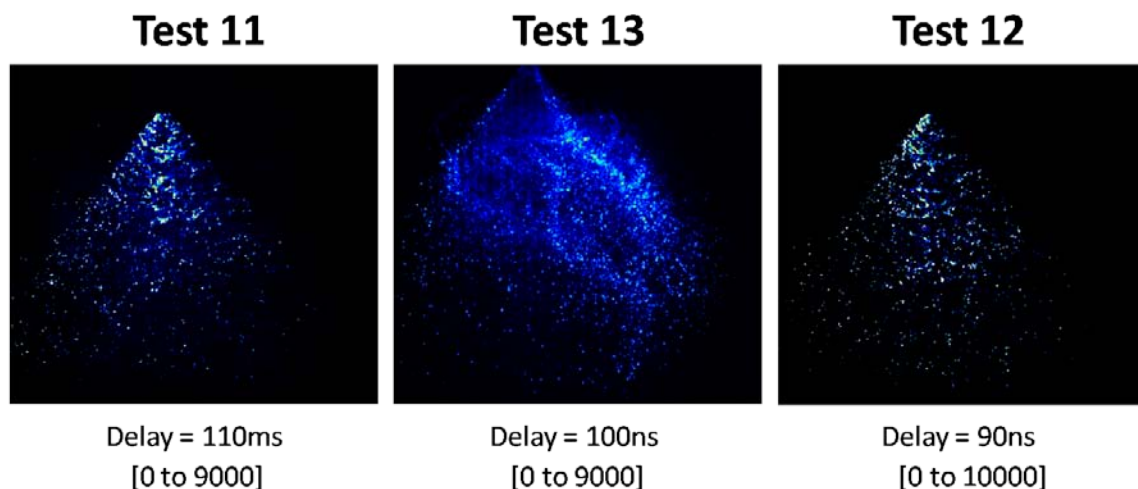
Figure 15: Comparison of data collected in the laboratory setup, Test 11, Test 12 and Test 13, highlighting the relationship between the delay to the first exposure and measured fluorescence signal intensity under the same flow conditions.

With the increase in adjustment it is easier to see the difference between the delays and what effect it has on the received fluorescence signal. Starting on the far left, delay of 110ns, and moving to the center image, delay of 100ns, the delay is decreased by 10ns. With this decrease in delay, the laser pulse moves closer to the edge of the first exposure of the fluorescence image. This can be more easily seen when looking at Figure 11, above. As the laser pulse moves closer to the edge of this first exposure, it has less time to collect this signal and report it as fluorescence. As discussed above, both fluorescence and phosphorescence events are occurring and decaying at the same time. Moving the laser pulse in this fashion does not give an accurate representation of the phosphorescence signal as it is more likely capturing both events.

This trend is continued in the image on the far right. In order to maximize each of the fluorescence and phosphorescence signals, it is desired to adjust the delay to the smallest possible that still produces consistent signals in the fluorescence image.

4.2.3 Fuel Studies; Acetone and Jet A Fuel

This subsection focuses on the relationship between fuels as it relates to processed signal level. Both acetone and Jet-A fuel were chosen for this study. While much of this study deals with Jet-A fuel, not much is known about fluorescence or phosphorescence behavior. This creates a need to be able to benchmark the findings from the Jet-A fuel with results from a well characterized fuel, such as acetone.

Both fuels were tested under the same conditions and in the same experimental setup. These results for acetone and for Jet-A fuel, shown below in Figure 16, do show marked differences.
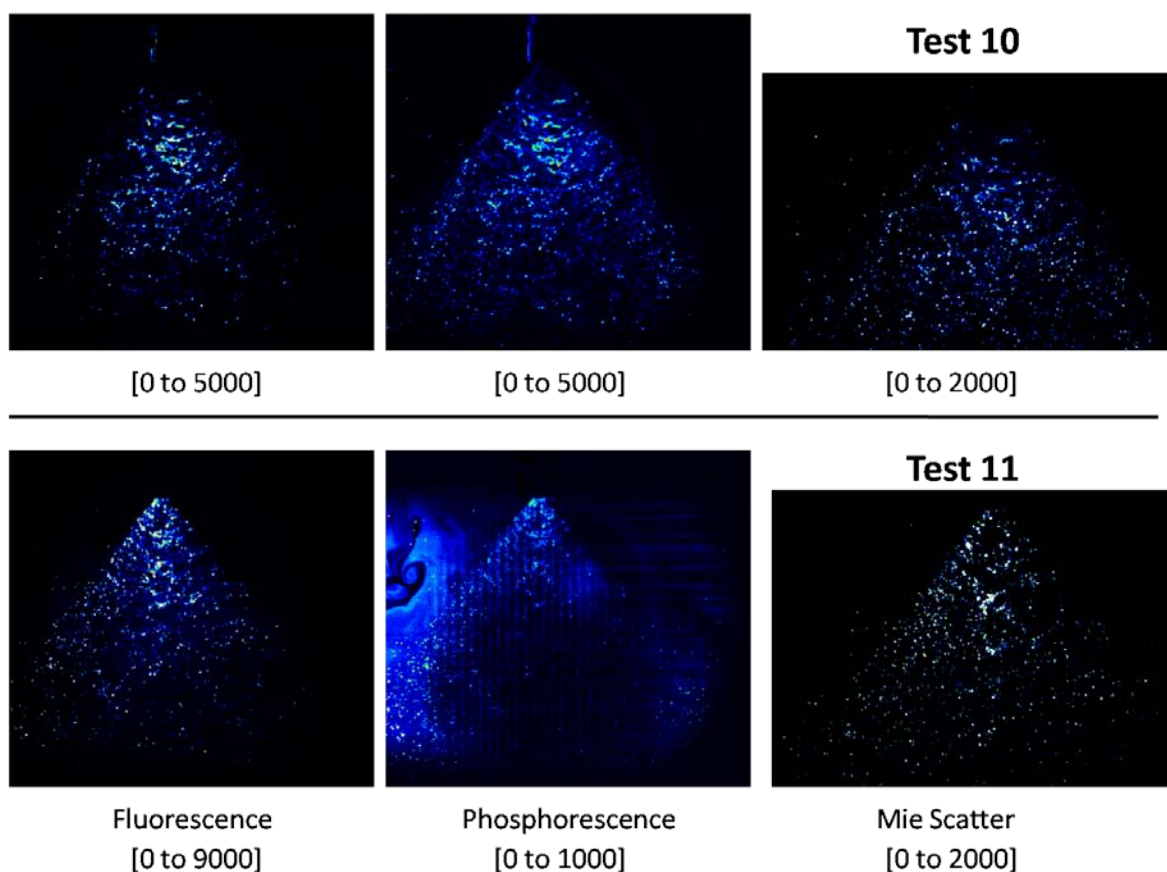
Figure 16: Comparison of data collected in laboratory setup, Test 10 showing Jet-A fuel and Test 11 showing acetone, highlighting the relationship between the fuel and measured signal intensity under the same flow conditions.

When fluorescence images from Test 10 and Test 11 are compared, note that each image had to be scaled to a different intensity level. Signal levels from the acetone fluorescence are nearly twice that of the jet-A fuel. However, this trend is not seen in the phosphorescence images. The reason for this is that the phosphorescent lifetime of acetone is much shorter than that of jet-A fuel, and so much of the signal is dominated by fluorescence. The swirl pattern

shown in the phosphorescence image demonstrates the limitations of this technique as this is most likely a rescatter event that is causing nearby vapor to fluoresce. As expected, the Mie scattering signal intensity did not change with the different fuel. This is due to the characteristics of Mie scattering, which does not actually interact or excite the fuel and simply scatters off of the surface. Hence, it can be expected that if the input laser energy is the same and the nozzle creates roughly the same spray structures that the scattering signals should be relatively unaffected.

While these concepts can be quantified experimentally, this was not the purpose of this work and therefore the data collection system was not designed as such.

4.2.4 Subtraction Methods and Results

As stated before, the fluorescence and phosphorescence images both depend on liquid volume and it is of interest to determine if the signals can be subtracted from one another to produce an image that contains only the vapor regions of the spray. This is done by taking a fluorescence image, which is supposed to contain both liquid and vapor intensities, and subtract from that a phosphorescence image, which is supposed to contain only liquid data. The result from this subtraction would be an image containing only vapor intensities.

Results from one of these subtractions can be seen below in Figure 17. The original fluorescence and phosphorescence images come from Test 20 from the data collected in the test section with heated crossflow. The first image is a direct subtraction of the phosphorescence image from the fluorescence image. The second image is still a direct subtraction of the two images, but this time the phosphorescence image is scale by 1.538 times its original magnitude. This number is selected as it minimizes, both positive and negative intensity values, for a given region of the image that contains primarily signal and little of the background. The third image is

also a direct subtraction, this time scaling the phosphorescence image by 3 times its original

magnitude. Again, this number is selected because it minimizes the magnitude of a region that is

much smaller and contains just a few discrete points of light that are thought to be droplets.
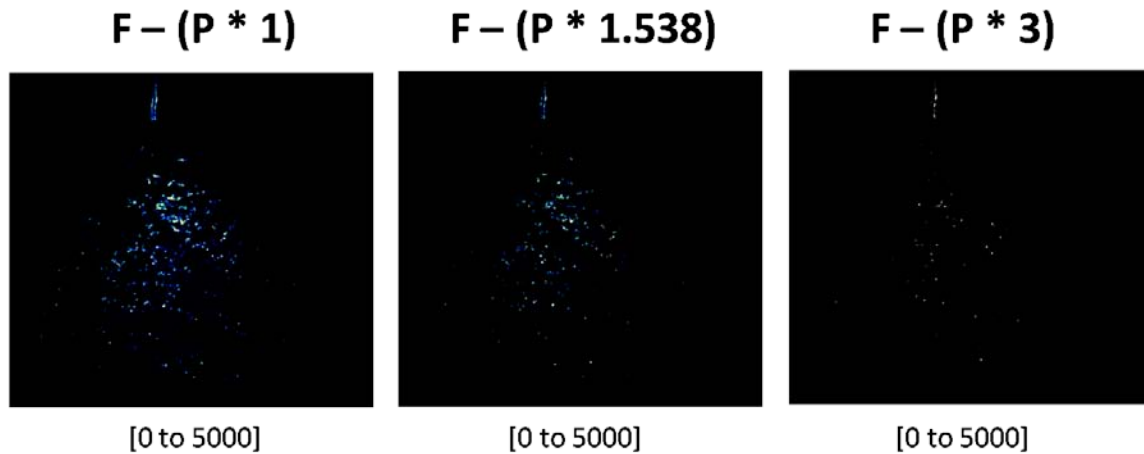
Figure 17: Comparison of data collected in laboratory setup, Test 20, showing the resultant image after image subtraction is conducted on the data set. Each subtractions use a scaled-magnitude phosphorescence image for the subtraction. These scaling factors are 1, 1.538, and 3 from left to right.

While it was hoped that a clear image map of the regions that only contained vapor would

emerge, no vapor is visible in the subtracted image. While these points to a lack of vapor being

present under these conditions, it is also possible that the larger intensity values from the liquid

region dominate the image and mask any regions of vapor that may otherwise appear.

4.3 Presentation of Test Cell Application Data

Section 4.3 presents the processed data generated by experiments in an test section with

heated crossflow facility. This data encompasses a number of different test criteria for injection

into a heated crossflow of air, including changes in fuel flow rate, crossflow velocity, timing

issues, crossflow gas temperature, image or laser sheet orientation/ height effects on spray

characteristics and signal intensity. Both horizontal and vertical orientations detailed earlier are presented in this section.

4.3.1 Signal Intensity Dependencies on Fuel Flow Rate

This subsection focuses on the relationship between fuel flow rates and processed signal level. Rather than controlling delivery pressure as was the case for the laboratory-scale tests, the desired fuel flow rate in the test-cell facilities was controlled directly and did not require a change in nozzle geometry.

The data, shown below in Figure 18, compares the same exact flow conditions but with a different flow rates. Test 17 has a total fuel flow rate that is twice that of Test 21.
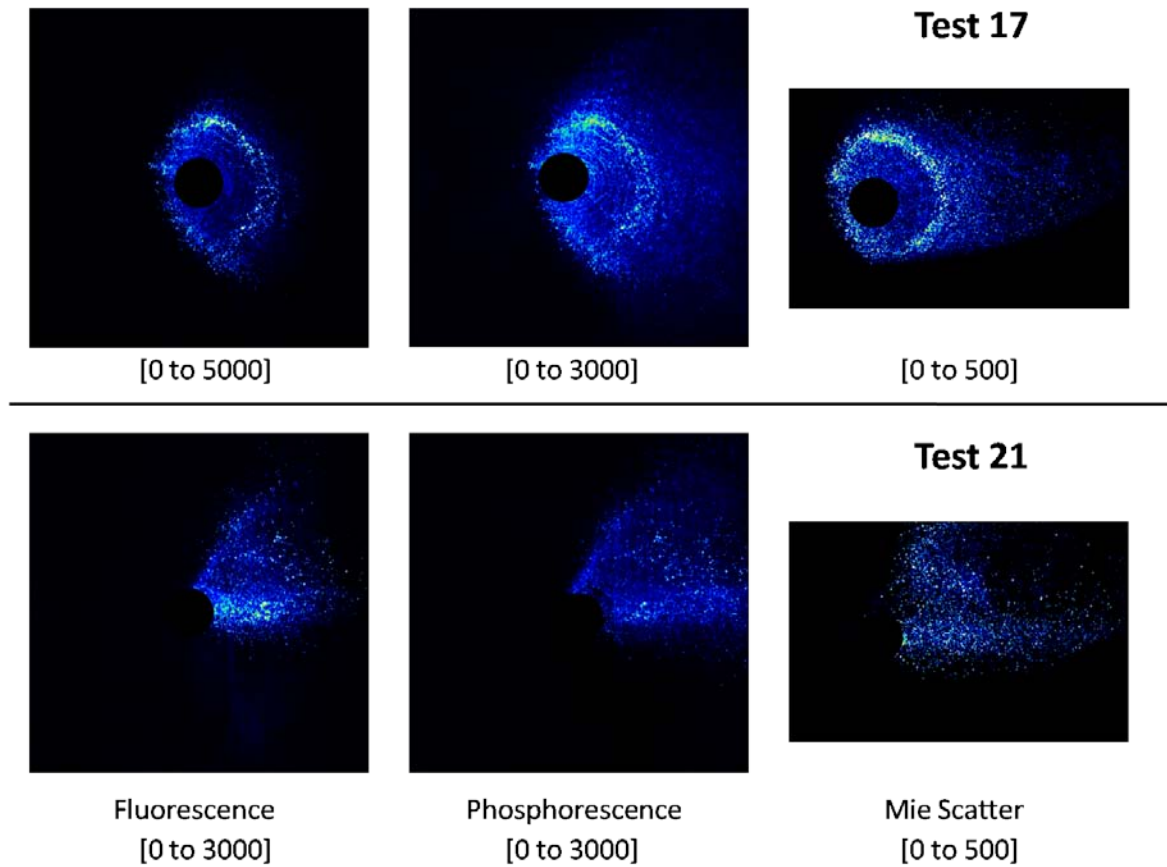
Figure 18: Comparison of data collected for a test cell application, Test 17 and Test 21, highlighting the relationship between an increase in fuel flow rate and measured signal intensity. The fuel flow rate in Test 17 is twice that of the fuel flow rate in Test 21.

As discussed before, an increase in fuel can be expected to increase the total received signal for that test. This trend is supported qualitatively in Figure 18. In addition, it is also noted that with this increase in total fuel flow that the liquid-to-air momentum ratio increases and the crossflow has less of an effect on the spray. This leads to the cone shape for Test 21 as the crossflow is able to collapse the structure of the spray.

4.3.2 Signal Intensity Dependencies on Crossflow Velocity

This subsection presents the data collected for a test cell application and focuses on the relationship between crossflow velocity as it relates to processed signal level and spray structure. Similar to that of fuel flow in the previous section, changes can be easily made to the amount of crossflow for each test. With this ability it is possible to ensure that each of the tests presented in this section have the exact same flow conditions except for the crossflow velocity. Shown below in Figure 19, Test 24 has three times the crossflow velocity as Test 26.
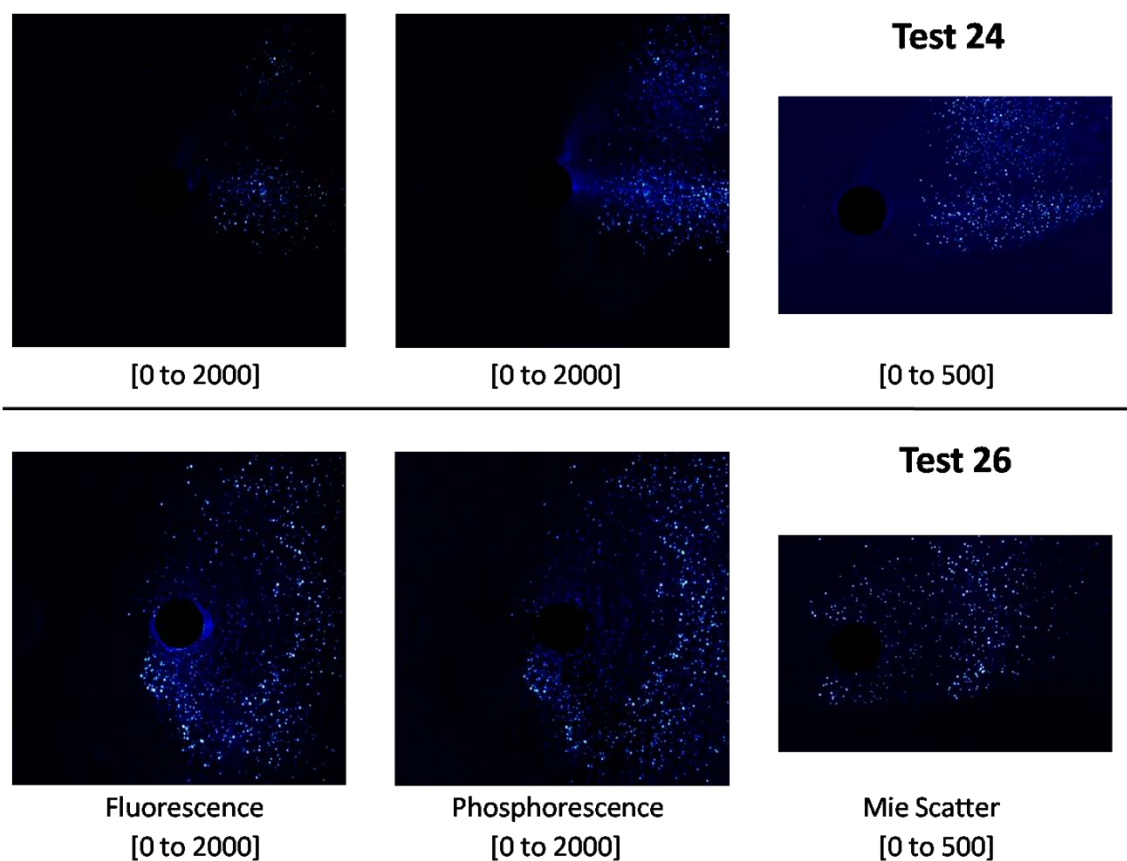
Figure 19: Comparison of data collected for a test cell application, Test 24 and Test 26, highlighting the relationship between an increase in crossflow velocity and measured signal intensity as well as spray structure. The crossflow velocity in Test 24 is three times that of the crossflow velocity in Test 26.

Comparisons between the conditions shown in Figure 19 are a bit easier to make as each of the images are scaled to the same limits. Initially it is quite easy to see that increasing the amount of crossflow drastically changes the shape of the spray. In terms of the shape, Test 26 shows the spray to be very much collapsed and much of the spray droplets have been moved further down the test section due to this large increase in crossflow velocity. It is important to note that the same signal levels are recorded. There seems to be no change in absolute maximum signal even though there seems to be fewer droplets to create this signal. This demonstrates that the crossflow has little to do with adjusting the signal of the fluorescence, phosphorescence, or Mie scattering, but has a large effect on spray shape.

4.3.3 Camera Delay Sensitivities

This subsection presents the data collected for a test cell application and focuses on the relationship between exposure start times delayed from the laser pulse as it relates to processed signal level. These delays are modified by adjusting the time delay within the digital signal generators responsible for controlling all the components in the experiment. This manner of adjustment is the same as what was used for the laboratory-scale experiments. These delays and corresponding images are shown below in Figure 20. Each image from the given condition represents the fluorescence signal. Thus accurate comparisons can be made between each of the images as they are comparing the same flow conditions and signal.

Test 14   Test 15   Test 16

Delay = 110ns   Delay = 210ns   Delay = 10ns
[0 to 5000]   [0 to 5000]   [0 to 100]
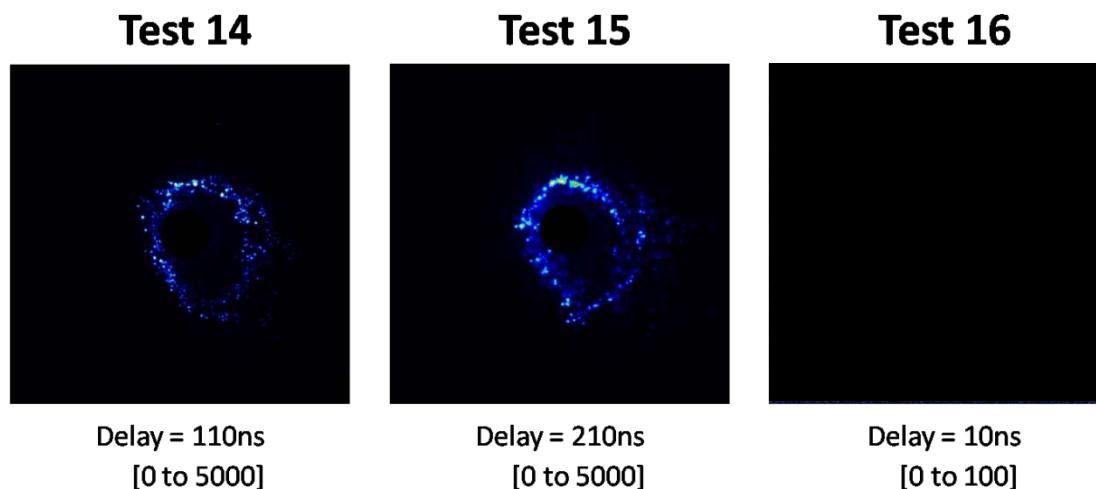
Figure 20: Comparison of data collected for a test cell application highlighting the relationship between the delay between the exposure and the laser pulse and measured signal intensity. The delay between the laser pulse and the exposure start time is shown for Test 14, Test 15, and Test 16.

The delay changes are much larger than that of the changes made in the laboratory setup. With the increase in adjustment it is easier to see the difference between the delays and what effect it has on the received fluorescence signal. Starting on the far left, delay of 110ns, and moving to the center image, delay of 210ns, the delay is increased by 100ns. Larger changes were made to the delay to further elaborate on finding from work done previously in the laboratory setting. With this increase in delay, the laser pulse moves further with in the first exposure of the fluorescence image. This can be more easily seen when looking at Figure 11, above. As the laser pulse moves further within this first exposure, it has more time to collect this signal and report it as fluorescence. As discussed above, both fluorescence and phosphorescence events are occurring and decaying at the same time. Moving the laser pulse in the fashion does not give an accurate representation of the fluorescence signal as it is capturing both events.

Moving the laser pulse in the other direction, seen when going from the image on the far left in Figure 20 with a delay of 110ns to the image on the far right with a delay of 10ns, is a

change of 100ns again. With the laser pulse moving in the other direction, the laser pulse actually falls outside of the first exposure's envelope and is not captured at all by the fluorescence image. This is why there is no signal at all in the image on the far right.

In order to maximize each of the fluorescence and phosphorescence signals, it is desired to adjust the delay to the smallest possible that still produces consistent signals in the fluorescence image.

4.3.4 Signal Intensity Dependencies on Sheet Orientation in the Spray

This subsection presents the data collected for a test cell application and focuses on the relationship between laser sheet orientation as it relates to processed signal level and spray structure. Because all optics and cameras were mounted on a large translation stage is was possible to make height adjustments and collect data at different heights within the spray.

The first comparison used a horizontal laser sheet for excitation at two different heights within the spray. This comparison is shown below in Figure 21. In this comparison, Test 25 is collected at twice the height from the nozzle as Test 20. With all flow conditions and experimental parameters held constant, it is possible to make comparisons that only depend on height within the spray.
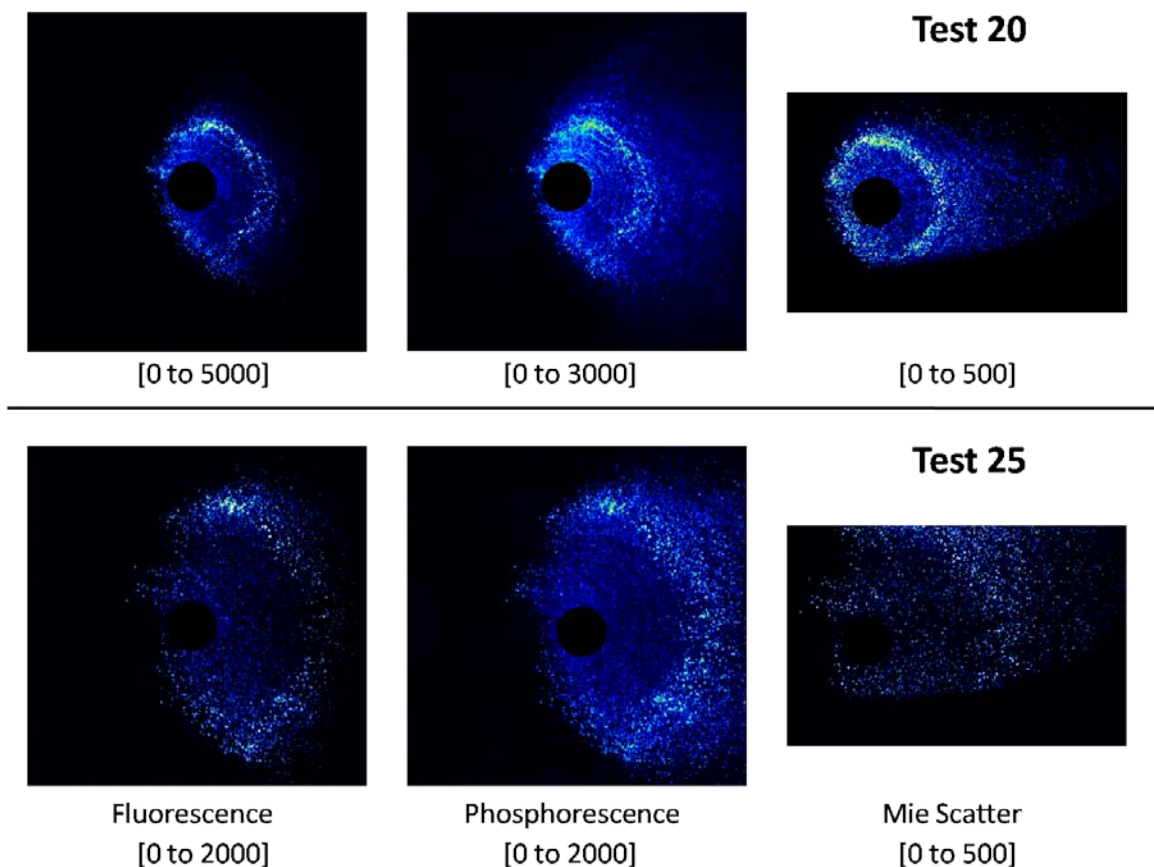
Figure 21: Comparison of data collected for a test cell application, Test 20 and Test 25, highlighting the relationship between the height within the spray and measured signal intensity as well as spray structure. The height in Test 20 is twice that of the height in Test 25.

When looking at Test 20, which is the lower of the two heights sampled, there appears to be more signal received than that of Test 25. This is supported when comparing the color scaling applied to each of the two conditions. Because neither fluorescence nor phosphorescence has any dependencies on the height in which it is sampled, this can be attributed to conservation of mass. As the same amount of fuel is sampled at a greater height the fuel spreads and the signal intensity diminishes. If the intensity of each of the cells were added together to form a single, total intensity for each height that intensity would be very close to the same.

A second sheet orientation study was conducted that passes a vertical sheet through the spray at different distances from the centerline of the spray. This data, each showing fluorescence images, is presented below in Figure 22.
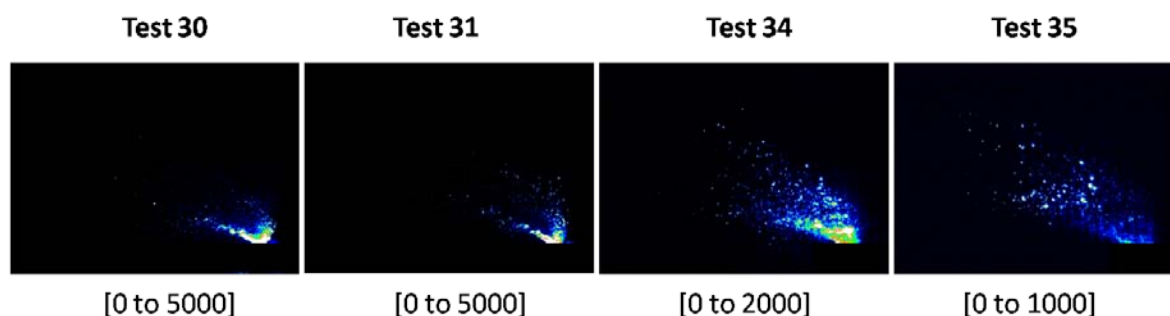
Figure 22: Comparison of data collected for a test cell application, Test 30, 31, 34 and 35, highlighting the relationship between the vertical distance from centerline of the spray and measured signal intensity as well as spray structure. Test 30 is taken at centerline while Test 35 is taken at the outer edge of the spray. Test 31 and 34 are equally spaced between Test 30 and 35.

While it may be hard to resolve the internal structures present in the spray, this comparison shows how the spray structures change as the laser sheet is moved from the centerline of the spray to the outer edge. Test 30 is taken at the centerline of the spray and Test 35 is captured at the outer edges of the spray. Test 31 and 34 are equally spaced between Test 30 and 35. It is possible to see the transition between dense structures seen in Test 30 and smaller and more dilute structures present in Test 35. This theme is also supported by the changing intensities from the centerline data to that on the edge of the spray. As expected, larger groups of higher intensity regions are present at the centerline while smaller groups of reduced intensity are present in outer regions. Interestingly, even at the outer spray location, liquid near the spray nozzle can be observed even though the laser sheet does not pass through the centerline of the spray. This can be attributed to light from either Mie scattering, fluorescence, or

phosphorescence that is illuminating the spray near the nozzle. This provides strong evidence of multiple scattering effects in the spray.

4.3.5 Signal Intensity Dependencies on Temperature

This subsection presents the data collected for a test cell application and focuses on the relationship between ambient air temperatures as it relates to processed signal level.

One concern that was present was the amount of fuel vapor being produced. While all fuels tested will vaporize at room temperature, the process is much slower than that seen in actual combustion processes. This thought can be seen a bit more clearly when looking at the distillation curve shown in Figure 23. At room temperature the amount recovered after distillation, or percentage of vapor is incredibly low, but at elevated temperatures, specifically above 200°C the amount of vapor produced is significantly higher.
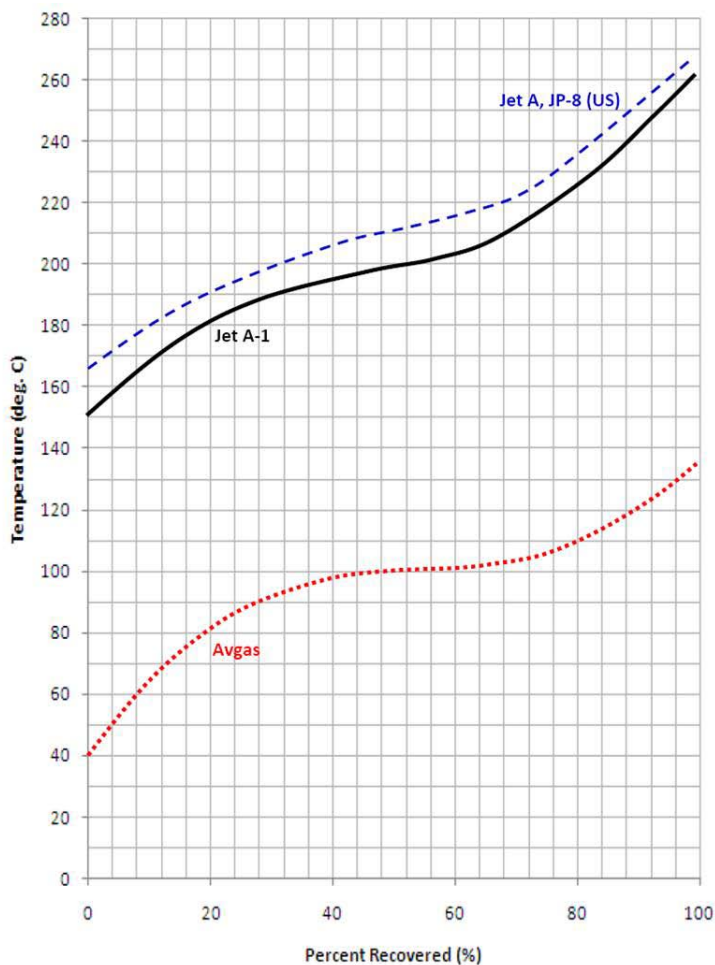
Figure 23: Typical distillation curve for standard aviation fuels according to ASTM D 86. Based on data from the Handbook of Aviation Fuel Properties (SAE, 2004)

One step taken to alleviate this concern was to run tests that would place the fuel spray

into test conditions that the ambient air temperatures were elevated to encourage evaporation.

The data produced from these tests can be seen in Figure 24.
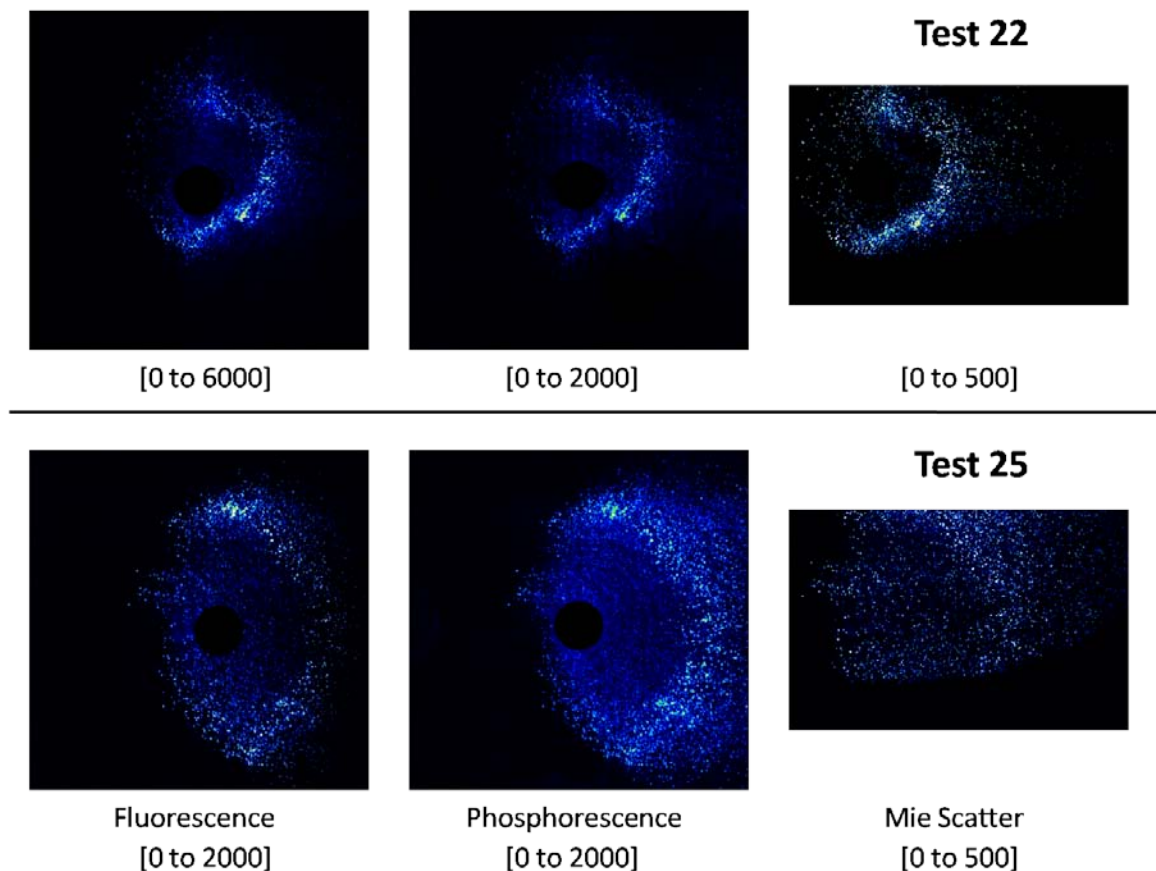
Figure 24: Comparison of data collected for a test cell application, Test 22 and Test 25, highlighting the relationship between the temperature and measured signal intensity as well as spray structure. The temperature of the ambient air in Test 22 is above the vaporization temperature of the fuel while the temperature in Test 25 is just below.

Seen above in the comparison, Test 22 indicates a reduction in the amount of fuel

vaporized due to the reduced signal levels. This is expected as it is this condition that was

subjected to the elevated ambient temperatures. One thing that is surprising though is that the

same dull glow that is seen in Test 25 is not seen in Test 22. One possible explanation for this is

that not as much of the fuel is being vaporized in Test 22 as originally thought. While the

ambient temperature for the test is just above the vaporization temperature of the fuel it is

possible that due to elevated flow rates or the ambient air being saturated with fuel vapor that not

as much fuel is allowed to vaporize. If this were the case, one would expect to see higher signal levels due to the saturated air containing the fuel vapor. This is not the case. Another explanation is that the other flow parameters that are not being held constant in the test are causing the spray shape in Test 22 to be more confined and actually not allowing the spray to spread out and vaporize more completely like seen in Test 25. Lastly, the two images are imaged at two different vertical heights and this can make these noted differences between the images more pronounced.

It is important to note that the overall geometry for each of the sprays are not the same. This is due to other flow parameters being modified at the same time as ambient air temperature. Hence, the variable under study is not completely isolated due to the experimental program determined by test-cell personnel. In the future, efforts will be taken to ensure that only one flow parameter is modified between each test to ensure the accuracy of the results.

CHAPTER 5. SUMMARY AND DISCUSSION

The purpose of Chapter 5 is to summarize the work accomplished, discuss challenges encountered while analyzing the data, and make final recommendations. Section 5.1 details the difficulties that arise in the type of analysis performed and suggest what improvements can be made in future work. Section 5.2 provides a summary of all discussed in the thesis and provides a conclusion of all work.

5.1 Challenges to Signal Interpretation

This section discusses the challenges related to reported signals as discussed above in Section 3. These challenges can be grouped into three areas: the occurrence of background scatter, the difference in signal between liquid and vapor, and the total production of vapor.

5.1.1 Rescatter and Backscattering Issues

One of the key challenges to analyzing the data is, depending on the data set, that there are only marginal differences between the fluorescence and phosphorescence images. Moreover, some of the phosphorescence images have broad regions of signal, normally indicative of fuel vapor, that are greater in intensity than the fluorescence signals. However, the phosphorescence images should only be responsible for signals from the liquid phase because of strong quenching of oxygen. This means that the fluorescence images should be much more filled in and have more structures appearing, both liquid and vapor. When looking at the images, the opposite seems to be true for a number of the data sets. In addition, the phosphorescence images also seem to show a dull glow in the background of each of the images. There is evidence that there can be significant rescattering within the spray. When the laser pulse is incident on the spray, the signal

is emitted in all directions. Because this signal has the opportunity to interact with other droplets, it can lead to a background glow rather like diffuse light as it passes through a cloud.

When looking at some of the fluorescence images and comparing them with Mie scattering images, which are known to only show liquid structures, the fluorescence images show discrete points of light and a dull glow. It could be suggested that this glow can be attributed to vapor regions. This may not be the case, however, due to the diffuse scattering that occurs away from the plane of imaging. This is why signals were seen near the injector tip even though the laser sheet was well away from the injector, as in the Test 35 in Figure 21. This phenomenon can be observed in other vertical plane data sets presented in the appendix. A good way to check this is to see if the same structures and characteristics that are present in the fluorescence images are seen as well in the phosphorescence images. This leads to the conclusion that broad regions of diffuse signal are not actually vapor and can be attributed to this rescattering phenomenon.

Very recently work has been completed that addresses this issue (Berrocal, 2008). The work suggests that diffuse scatter in dense sprays can pose significant challenges when trying to collect quantitative data. Berrocal presents data and conditions that are very similar to the laboratory-scale measurements performed here and also provides correction techniques to assist in analysis of the data. The current work on simultaneous fluorescence, phosphorescence, and Mie scattering does prevent misinterpretation of signals from dense sprays, although perhaps with the work done by Berrocal (2008) it may be possible to extend this to quantitative imaging.

5.1.2 Disparity Between Signal from Liquid and Vapor

Another issue seen in the fluorescence and phosphorescence images is the difference in signal levels produced by vapor and liquid. It is known that signal levels produced by vapor will

be lower than that of the signal levels produced by liquid. This is due to the higher density in the liquid droplets. Because the signal levels from the vapor are dominated by that of the liquid, it is difficult to accurately resolve the vapor regions. While it was verified that the detection scheme in this work is capable of detecting vapor signals, the subtraction of much higher signals from liquid regions using fluorescence and phosphorescence may overwhelm the available signal from vapor regions. If the technique is to be used for accurately resolving the vapor regions of a spray, it is necessary to improve this aspect of the technique.

5.1.3 Total Production of Vapor

Lastly, if the one of the main aspects of the technique is to be able to resolve vapor within a liquid/vapor spray, sufficient vapor must be produced for reliable tests to be conducted. Because many of the tests were conducted at standard temperature and pressure, reduced amounts of vapor were produced. While the fuels studied do atomize at these temperatures and pressures, high levels of vapor are not produced under these conditions. This is supported when looking at distillation curves of each of the fuels. At room temperature the amount recovered after distillation, or percentage of vapor is incredibly low, but at elevated temperatures, specifically above 200°C the amount of vapor produced is significantly higher. From this, it can be concluded that minimal amounts of vapor was produced and the signal produced by this vapor is easily dominated by the large amounts of liquid fuel also in the spray. For future testing it is recommended that the tests are conducted at elevated temperatures in order to produce larger amounts of fuel vapor.

5.1.4 Future Work

It follows logically that future work should take on two forms: correcting what needs to be corrected from previous work and expanding on the present work. The future work here will be no different.

Future work will employ updated post-processing schemes to eliminate issues seen in this work such as multiple-scatter and rescatter. It will also include expanded test conditions to include higher temperature regions that would produce more vapor. This, in combination with a more sensitive camera for the dual frame imaging, would increase the overall vapor signal and provide an increased signal to noise ratio that this work lacked. In terms of expanding this technique it would much benefit from an application to other fuels, both simple and complex. This would hopefully better quantify fluorescence and phosphorescence lifetimes and their application.

5.2 Summary

In summary, the diagnostic technique that simultaneously captures images of fluorescence, phosphorescence, and Mie scattering is capable of providing additional information about the state of atomization and vaporization than would otherwise be unavailable from the use of only one or two of the techniques. This capability arises because of the different photophysics of each approach. Fluorescence is sensitive to liquid and vapor phases, and its liquid signal is proportional to droplet volume. Phosphorescence is sensitive to the liquid phase, and its vapor phase is quenched in the presence of oxygen. Like fluorescence, its signal from liquid is proportional to droplet volume. Mie scattering is sensitive to the liquid phase only, and is proportional to droplet surface area. These techniques are not without their limitations.

Originally developed to produce fluorescence and phosphorescence images that are able to be subtracted from one another to leave only vapor regions, this aspect of the technique was only partially successful. Comparison of fluorescence and phosphorescence signals could be used to avoid misinterpretation of vapor signals, but quantitative subtraction of the two signals was difficult because of interferences from multiple scattering of the signals in the spray. While full-image, flat field subtraction does not produce viable data, subtraction techniques when only used in smaller, dilute regions of the image sets is able to resolve some of the desired spray characteristics. The use of phosphorescence for marking liquid regions is clearly more accurate as its signal is proportional to droplet volume as is the case for fluorescence. The use of Mie scattering combined with fluorescence for extracting information on vapor concentrations would result in significant errors in signal interpretation. Phenomena such as rescattering within the spray, intensity disparity between vapor and liquid regions, and a lack of production of vapor have hindered full analysis of the data, although use of the three imaging techniques simultaneously has clearly improved the insight that can be gained regarding spray structure. Recent work to correct the problem of diffuse scattering can be implemented to make this approach more applicable to realistic sprays. Hence, while unable to provide quantitative data in its present state, the demonstration of simultaneous fluorescence, phosphorescence, and scattering data was successfully implemented and shown to be a powerful qualitative spray diagnostic tool capable of providing much needed clarity to present fuel spray work.

APPENDIX

A.1 Laboratory Setup Data

Test Name	Fuel Flow Rate		Injection Pressure		Variable Delay*		Selected Fuel
Test 1	7.57	lph	689.48	kPa	120	ns	Jet-A
Test 2	3.79	lph	689.48	kPa	120	ns	Jet-A
Test 3	3.79	lpm	275.79	kPa	120	ns	Jet-A
Test 4	3.79	lpm	275.79	kPa	120	ns	Jet-A
Test 5	3.79	lpm	275.79	kPa	120	ns	Jet-A
Test 6	3.79	lpm	275.79	kPa	120	ns	Jet-A
Test 7	0.76	lpm	275.79	kPa	120	ns	Jet-A
Test 8	0.76	lpm	275.79	kPa	120	ns	Jet-A
Test 9	0.76	lpm	275.79	kPa	120	ns	Jet-A
Test 10	0.76	lpm	275.79	kPa	110	ns	Jet-A
Test 11	0.76	lpm	275.79	kPa	110	ns	Acetone
Test 12	0.76	lpm	275.79	kPa	90	ns	Acetone
Test 13	0.76	lpm	275.79	kPa	100	ns	Acetone

* (Note on Variable Delay) – Refer to Figure 11 for physical clarification.
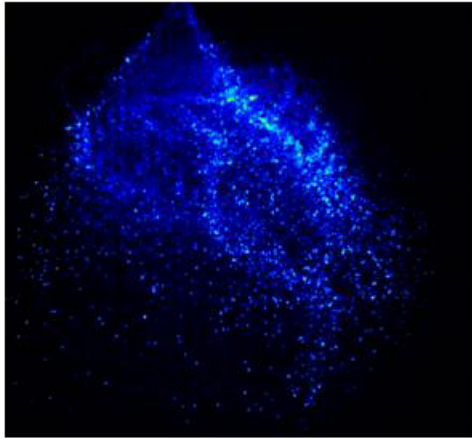
Test 1

Fluorescence	Phosphorescence	Mie Scatter
[0 to 3000]	[0 to 3000]	[0 to 13000]
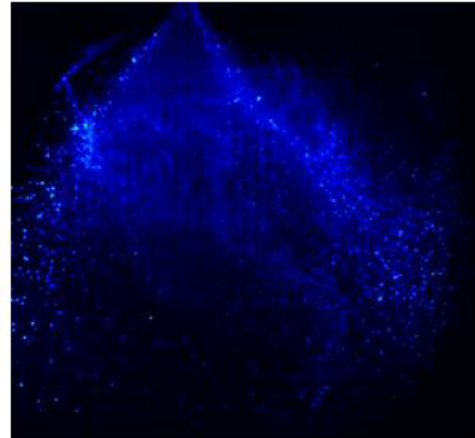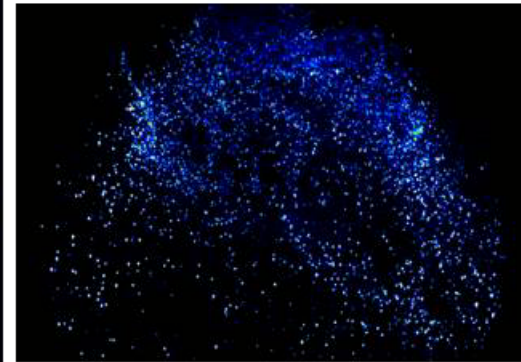
PCO Camera – 10µs exposure (first frame), f-stop: 2
Andor Camera – 30ms exposure, f-stop:11
Fuel Flow Rate – 7.57lph @ 689.48kPa
Delay to PCO – 120ns
Laser Energy – 112mJ/pulse

Test 2
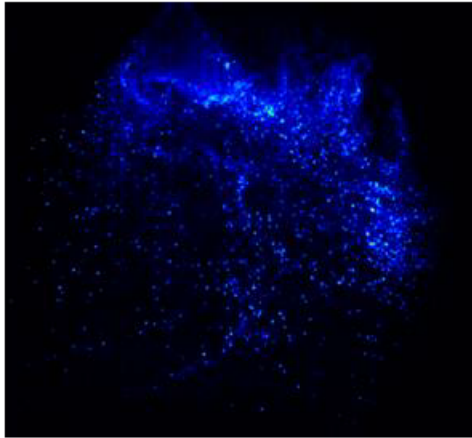
| Fluorescence | Phosphorescence | Mie Scatter |
| [0 to 3000] | [0 to 3000] | [0 to 13000] |
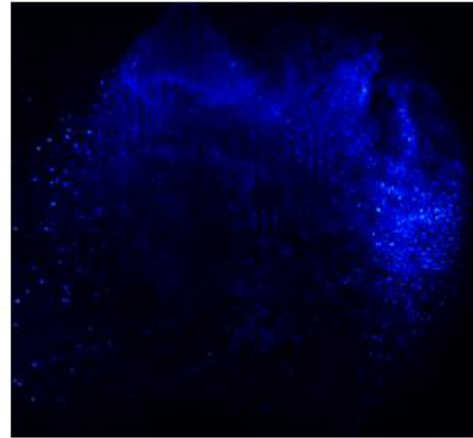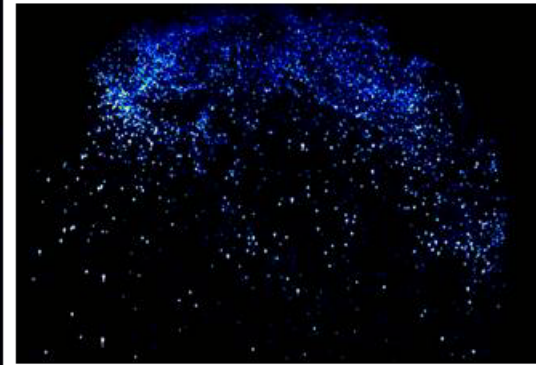
PCO Camera – 10µs exposure (first frame), f-stop: 2
Andor Camera – 30ms exposure, f-stop:11
Fuel Flow Rate – 3.79lph @ 689.48kPa
Delay to PCO – 120ns
Laser Energy – 112mJ/pulse

Test 3
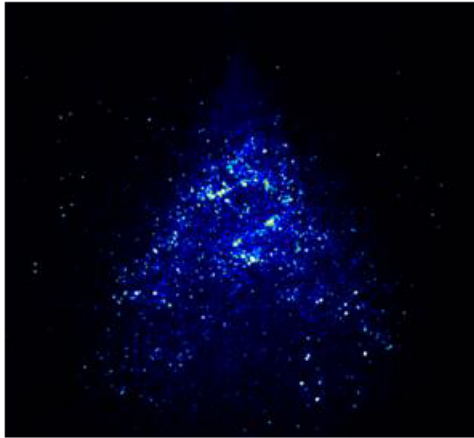
Fluorescence	Phosphorescence	Mie Scatter
[0 to 3000]	[0 to 3000]	[0 to 13000]
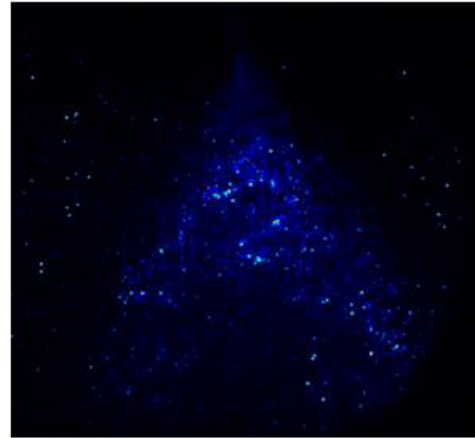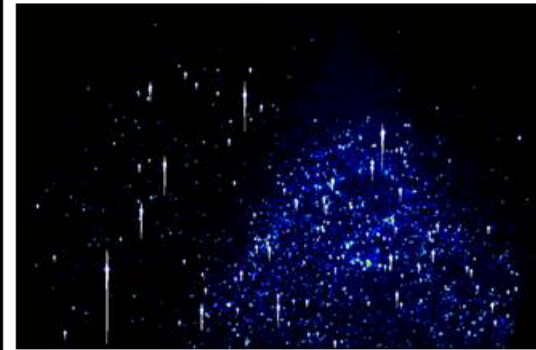
PCO Camera – 10μs exposure (first frame), f-stop: 5.6
Andor Camera – 30ms exposure, f-stop:11
Fuel Flow Rate – 3.79lpm @ 275.79kPa
Delay to PCO – 120ns
Laser Energy – 112mJ/pulse

Test 4
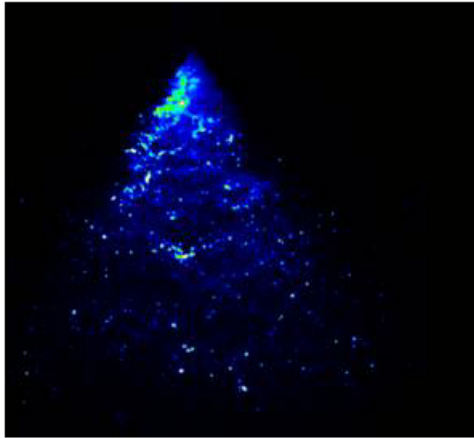
Fluorescence	Phosphorescence	Mie Scatter
[0 to 9000]	[0 to 3000]	[0 to 8000]
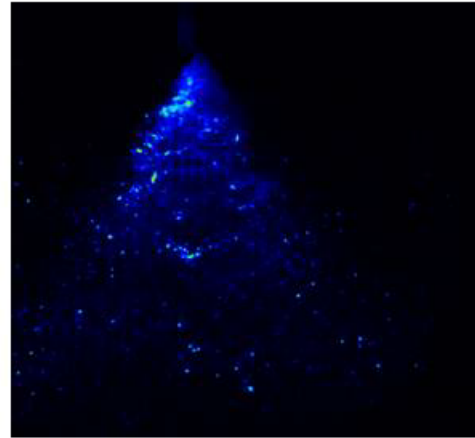
PCO Camera – 10μs exposure (first frame), f-stop: 4
Andor Camera – 30ms exposure, f-stop:22
Fuel Flow Rate – 3.79lpm @ 275.79kPa
Delay to PCO – 120ns
Laser Energy – 112mJ/pulse

Test 5
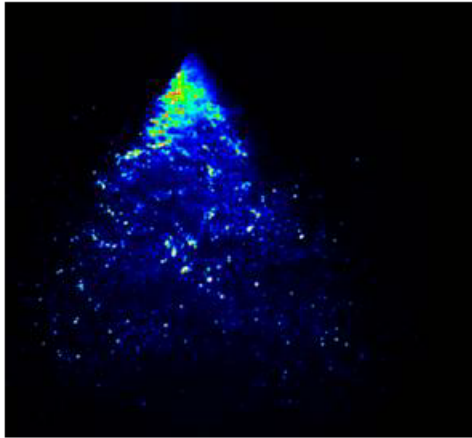
Fluorescence	Phosphorescence	Mie Scatter
[0 to 9000]	[0 to 3000]	[0 to 8000]
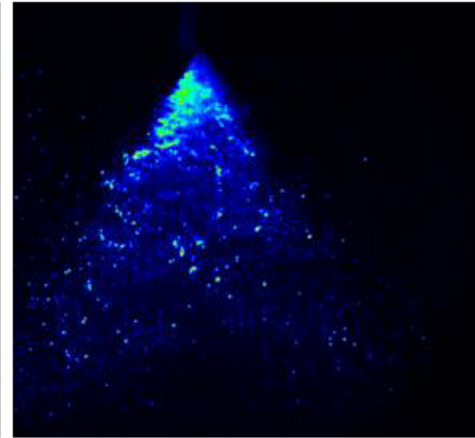
PCO Camera – 10μs exposure (first frame), f-stop: 4
Andor Camera – 30ms exposure, f-stop:32
Fuel Flow Rate – 3.79lpm @ 275.79kPa
Delay to PCO – 120ns
Laser Energy – 112mJ/pulse

Test 6
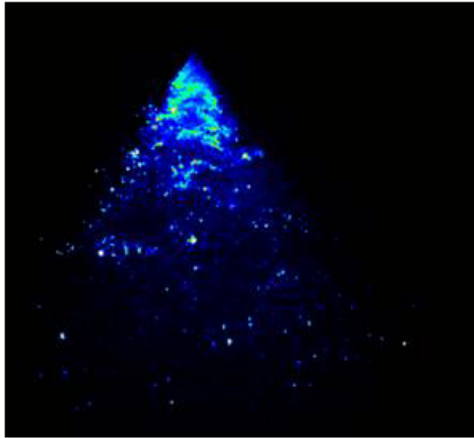
Fluorescence	Phosphorescence	Mie Scatter
[0 to 9000]	[0 to 6000]	[0 to 2000]
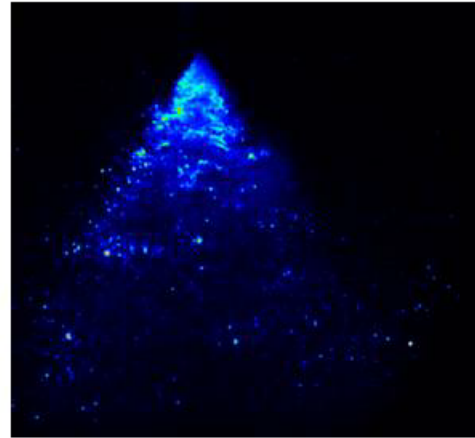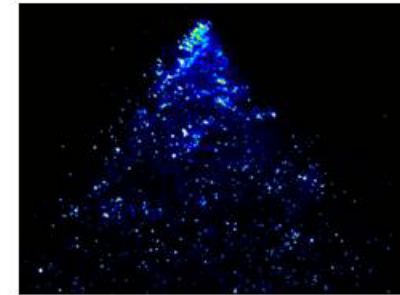
PCO Camera – 10µs exposure (first frame), f-stop: 4
Andor Camera – 30ms exposure, f-stop:16
Fuel Flow Rate – 3.79lpm @ 275.79kPa
Delay to PCO – 120ns
Laser Energy – 112mJ/pulse

w/ ND-100-2.0 (O.D. 1 Filter) added to Andor Camera

Test 7
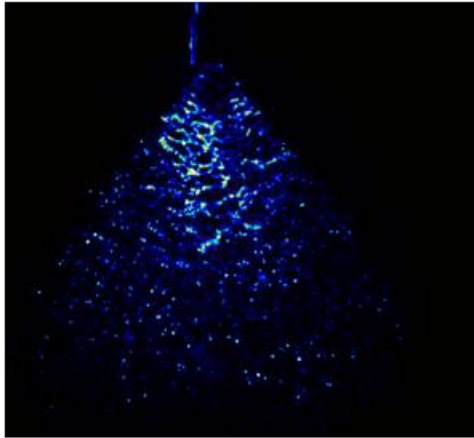
Fluorescence	Phosphorescence	Mie Scatter
[0 to 9000]	[0 to 3000]	[0 to 2000]
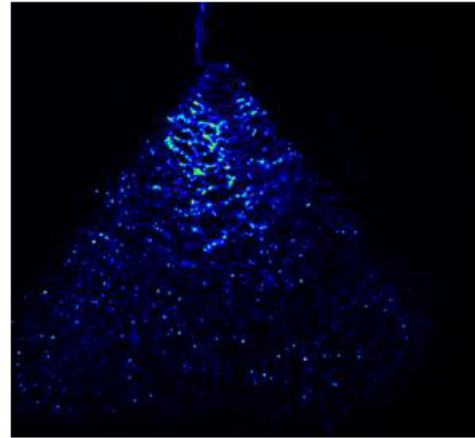
PCO Camera – 10µs exposure (first frame), f-stop: 4
Andor Camera – 30ms exposure, f-stop:16
Fuel Flow Rate – 3.79lpm @ 275.79kPa
Delay to PCO – 120ns
Laser Energy – 112mJ/pulse

w/ ND-100-2.0 (O.D. 1 Filter) added to Andor Camera

Test 8
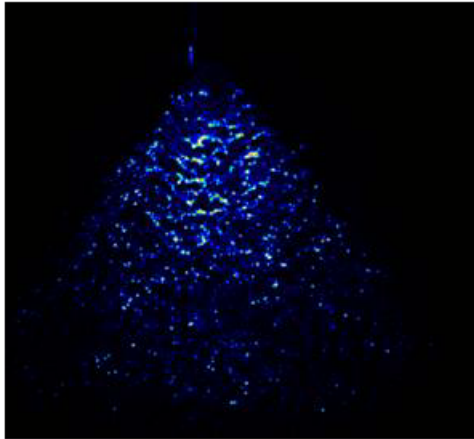
Fluorescence	Phosphorescence	Mie Scatter
[0 to 9000]	[0 to 3000]	[0 to 2000]
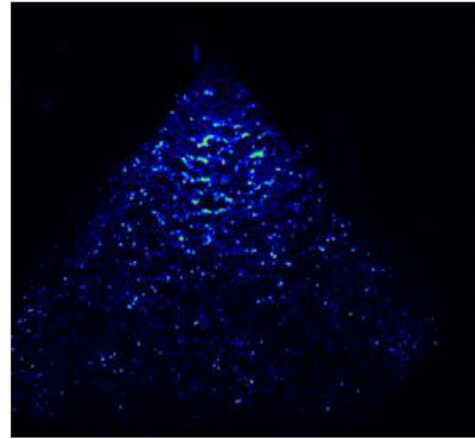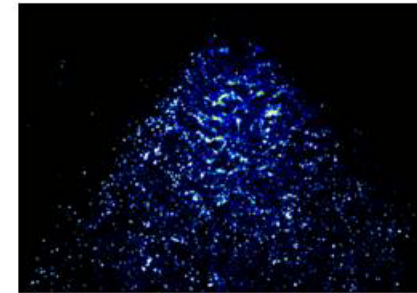
PCO Camera – 10μs exposure (first frame), f-stop: 4
Andor Camera – 30ms exposure, f-stop:11
Fuel Flow Rate – 3.79lpm @ 275.79kPa
Delay to PCO – 120ns
Laser Energy – 112mJ/pulse

w/ ND-100-2.0 (O.D. 1 Filter) added to Andor Camera

Test 9
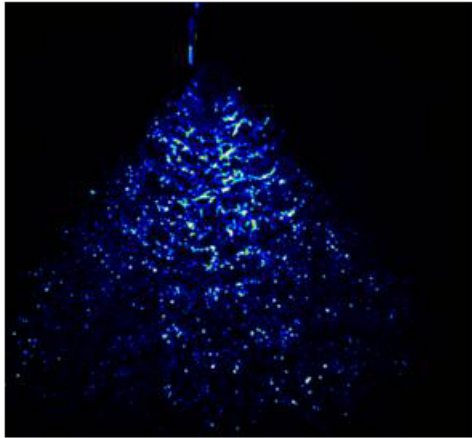
Fluorescence	Phosphorescence	Mie Scatter
[0 to 7000]	[0 to 2000]	[0 to 1000]
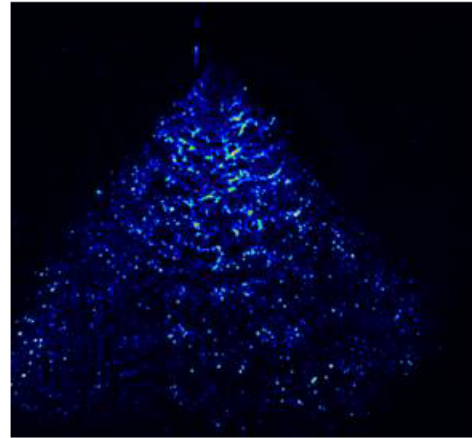
PCO Camera – 10µs exposure (first frame), f-stop: 4
Andor Camera – 30ms exposure, f-stop:22
Fuel Flow Rate – 3.79lpm @ 275.79kPa
Delay to PCO – 120ms
Laser Energy – 112mJ/pulse

w/ ND-100-2.0 (O.D. 1 Filter) added to Andor Camera

Test 10

Fluorescence	Phosphorescence	Mie Scatter
[0 to 5000]	[0 to 5000]	[0 to 2000]
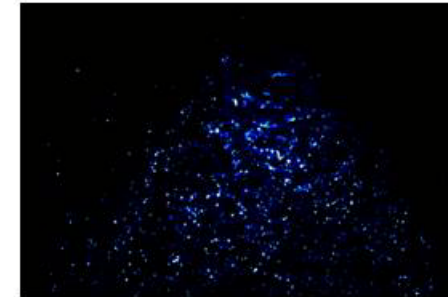
PCO Camera – 10µs exposure (first frame), f-stop: 4
Andor Camera – 30ms exposure, f-stop:16
Fuel Flow Rate – 3.79lpm @ 275.79kPa
Delay to PCO – 110ns
Laser Energy – 112mJ/pulse

w/ ND-100-2.0 (O.D. 1 Filter) added to Andor Camera

Test 11

Fluorescence	Phosphorescence	Mie Scatter
[0 to 9000]	[0 to 1000]	[0 to 2000]
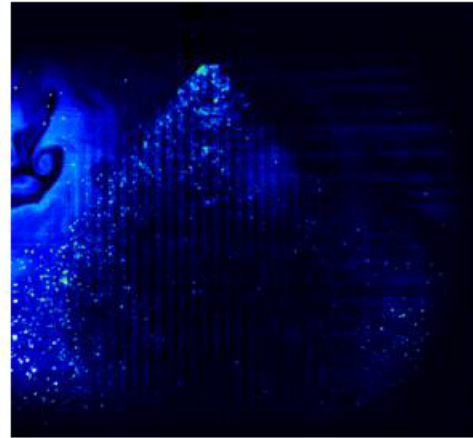
PCO Camera – 10μs exposure (first frame), f-stop: 4
Andor Camera – 30ms exposure, f-stop:16
Fuel Flow Rate – 3.79lpm @ 275.79kPa
Delay to PCO – 110ns
Laser Energy – 112mJ/pulse

w/ ND-100-2.0 (O.D. 1 Filter) added to Andor Camera

Test 12

Fluorescence	Phosphorescence	Mie Scatter
[0 to 10000]	[0 to 3000]	[0 to 2000]
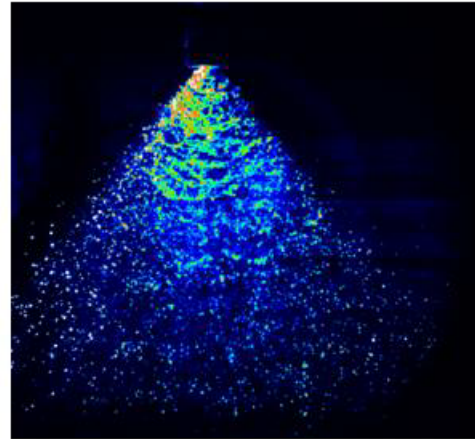
PCO Camera – 10μs exposure (first frame), f-stop: 4
Andor Camera – 30ms exposure, f-stop:16
Fuel Flow Rate – 3.79lpm @ 275.79kPa
Delay to PCO – 90ns
Laser Energy – 112mJ/pulse

w/ ND-100-2.0 (O.D. 1 Filter) added to Andor Camera

Test 13
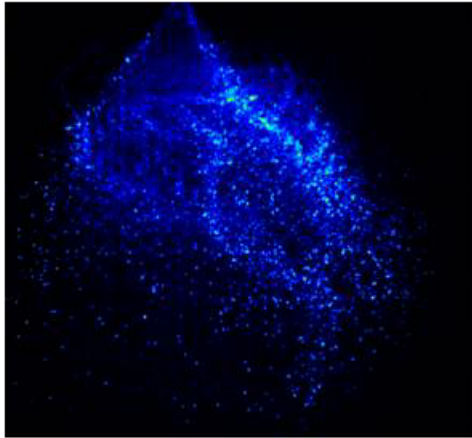
Fluorescence	Phosphorescence	Mie Scatter
[0 to 10000]	[0 to 3000]	[0 to 2000]
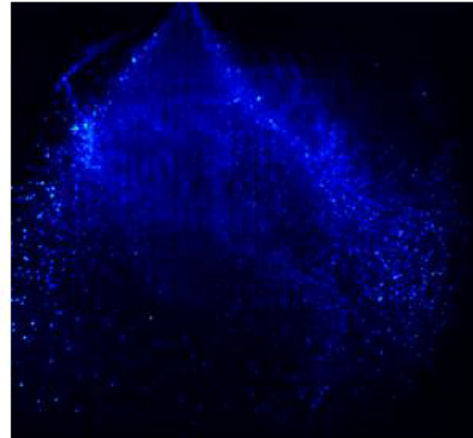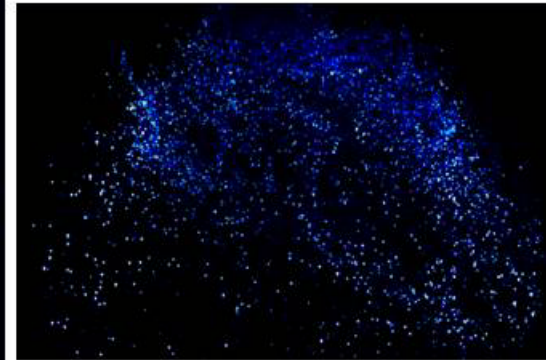
PCO Camera – 10μs exposure (first frame), f-stop: 4
Andor Camera – 30ms exposure, f-stop:16
Fuel Flow Rate – 3.79lpm @ 275.79kPa
Delay to PCO – 100ns
Laser Energy – 112mJ/pulse

w/ ND-100-2.0 (O.D. 1 Filter) added to Andor Camera

A.2 Test Cell Application Data

A.2.1 Images of Horizontal Planes through the Spray

Test Name	Fuel Flow Rate		Cross Flow Temperature		Plane Height		Cross Flow Velocity		Variable Delay*	
Test 14	9.07	kg/hr	446	K	12.7	mm	15	m/s	110	ns
Test 15	9.07	kg/hr	446	K	12.7	mm	15	m/s	210	ns
Test 16	9.07	kg/hr	446	K	12.7	mm	15	m/s	10	ns
Test 17	26.76	kg/hr	446	K	12.7	mm	46	m/s	110	ns
Test 18	26.76	kg/hr	446	K	12.7	mm	46	m/s	110	ns
Test 19	26.76	kg/hr	446	K	12.7	mm	46	m/s	105	ns
Test 20	26.76	kg/hr	446	K	12.7	mm	46	m/s	100	ns
Test 21	10.89	kg/hr	446	K	12.7	mm	46	m/s	100	ns
Test 22	18.60	kg/hr	557	K	12.7	mm	31	m/s	100	ns
Test 23	18.60	kg/hr	557	K	25.4	mm	30	m/s	100	ns
Test 24	10.89	kg/hr	444	K	25.4	mm	46	m/s	100	ns
Test 25	26.76	kg/hr	446	K	25.4	mm	46	m/s	100	ns
Test 26	9.07	kg/hr	449	K	25.4	mm	15	m/s	100	ns

* (Note on Variable Delay) – Refer to Figure 11 for physical clarification.

Test 14
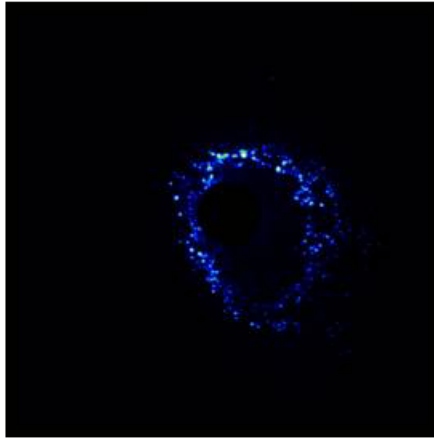
Fluorescence
[0 to 5000]
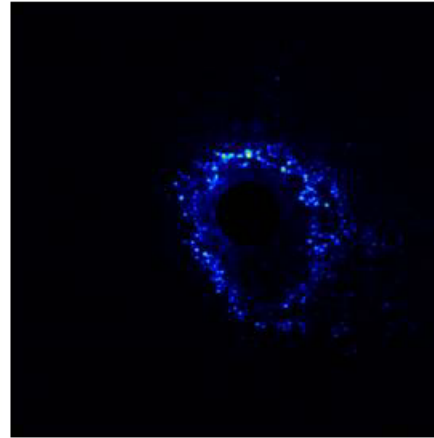
Phosphorescence
[0 to 5000]
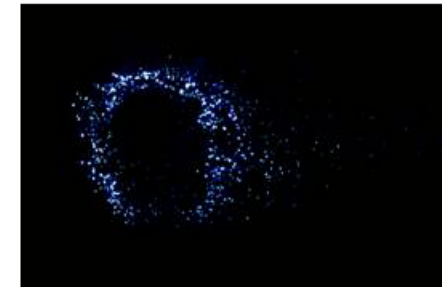
Mie Scatter
[0 to 500]

PCO Camera – 10ms exposure (first frame), f-stop: 2.8
Andor Camera – 20ms exposure, f-stop:16
Delay to PCO – 110ns
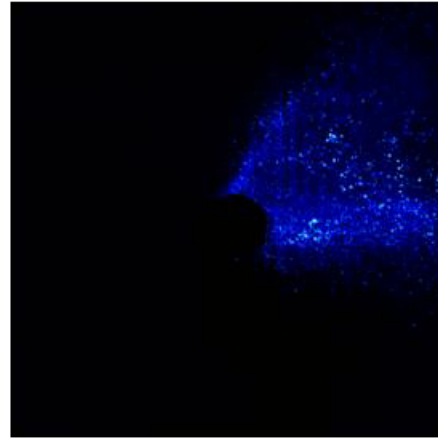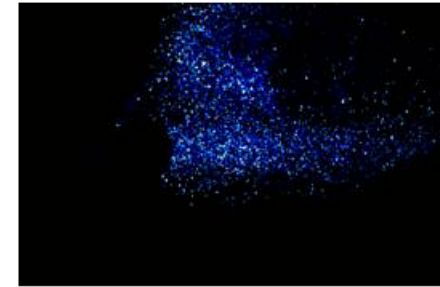Laser Energy – 133mJ/pulse

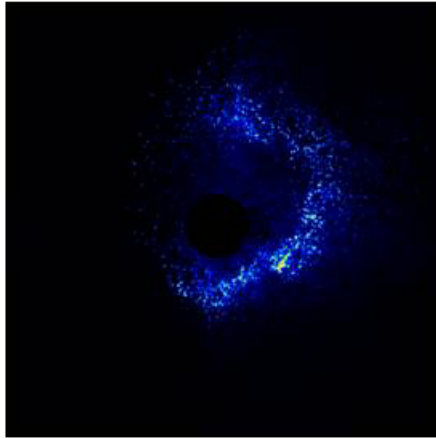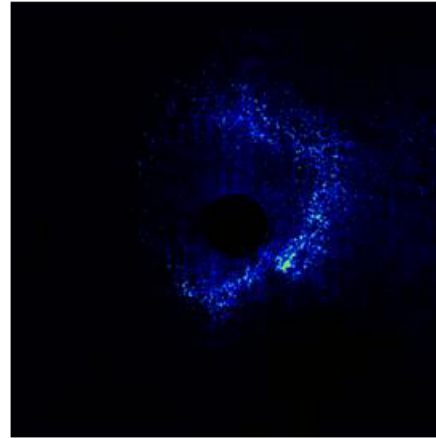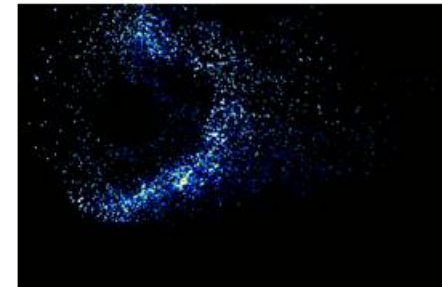Temp (K) – 446   Plane Height (mm)– 12.7
Fuel Flow (kg/hr) – 9.07   Cross Flow Velocity (m/s) – 15

Test 15
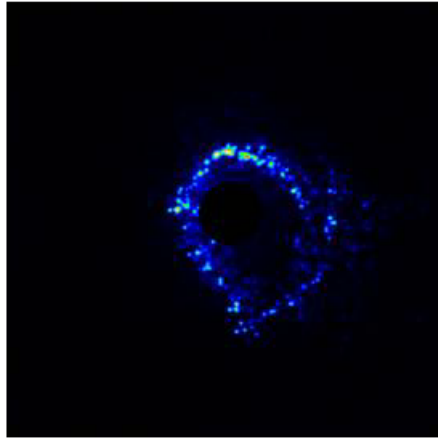
Fluorescence	Phosphorescence	Mie Scatter
[0 to 5000]	[0 to 200]	[0 to 500]
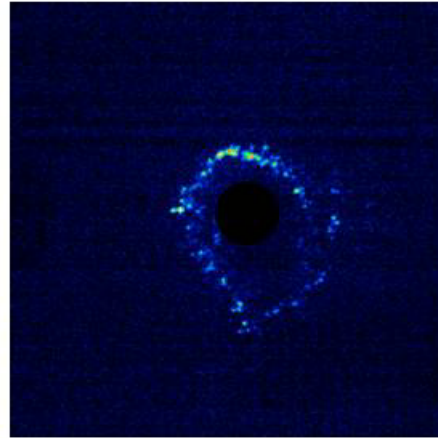
PCO Camera – 10ms exposure (first frame), f-stop: 2.8
Andor Camera – 20ms exposure, f-stop:16
Delay to PCO – 210ns
Laser Energy – 133mJ/pulse

Temp (K) – 446   Plane Height (mm)– 12.7
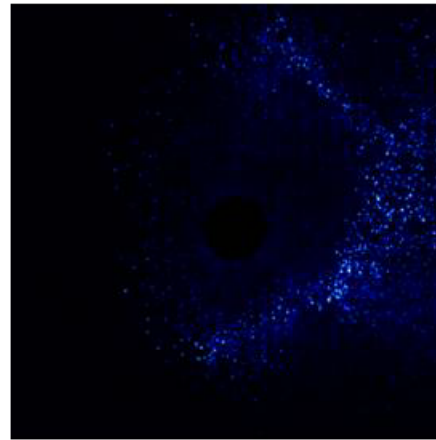Fuel Flow (kg/hr) – 9.07   Cross Flow Velocity (m/s) – 15

Test 16

Fluorescence	Phosphorescence	Mie Scatter
[0 to 100]	[0 to 5000]	[0 to 500]

PCO Camera – 10ms exposure (first frame), f-stop: 2.8
Andor Camera – 20ms exposure, f-stop:16
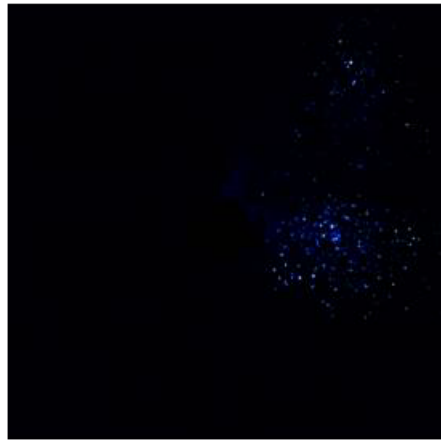Delay to PCO – 10ns
Laser Energy – 133mJ/pulse

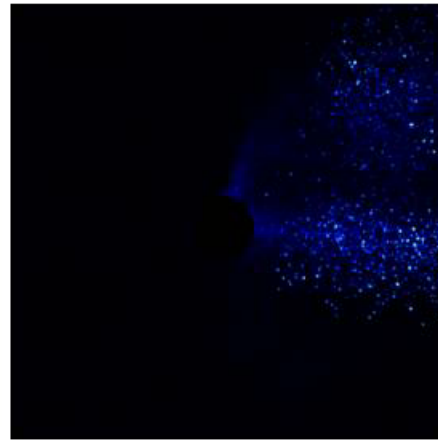Temp (K) – 446   Plane Height (mm)– 12.7
Fuel Flow (kg/hr) – 9.07   Cross Flow Velocity (m/s) – 15

Test 17
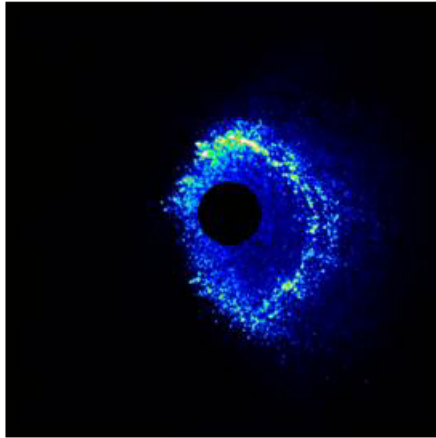
Fluorescence [0 to 7000]
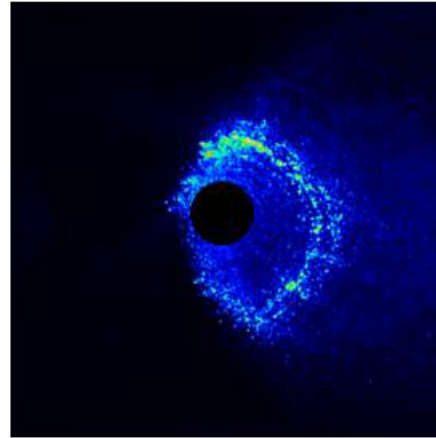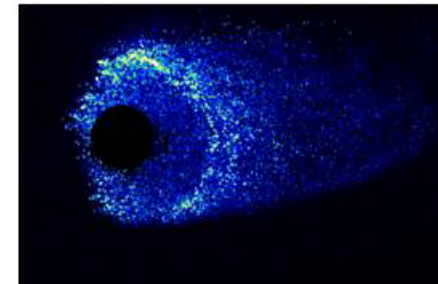
Phosphorescence [0 to 3000]

Mie Scatter [0 to 500]

PCO Camera – 10ms exposure (first frame), f-stop: 2.8

Andor Camera – 20ms exposure, f-stop:16

Delay to PCO – 110ns

Laser Energy – 133mJ/pulse

Temp (K) – 446	Plane Height (mm)– 12.7
Fuel Flow (kg/hr) – 26.76	Cross Flow Velocity (m/s) – 46

Test 18
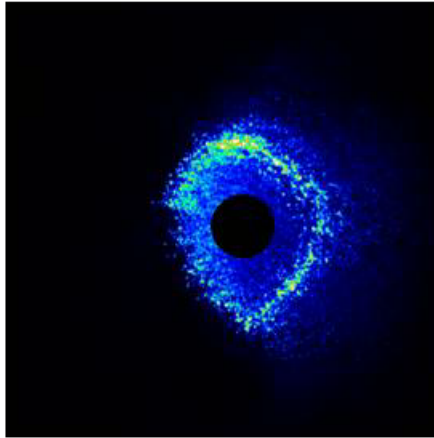
Fluorescence
[0 to 7000]
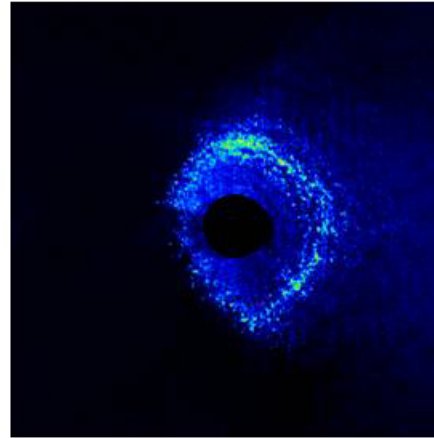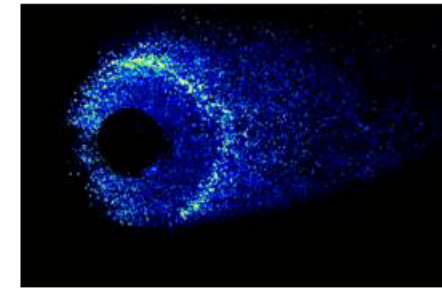
Phosphorescence
[0 to 3000]

Mie Scatter
[0 to 500]

PCO Camera – 10ms exposure (first frame), f-stop: 2.8
Andor Camera – 20ms exposure, f-stop:16
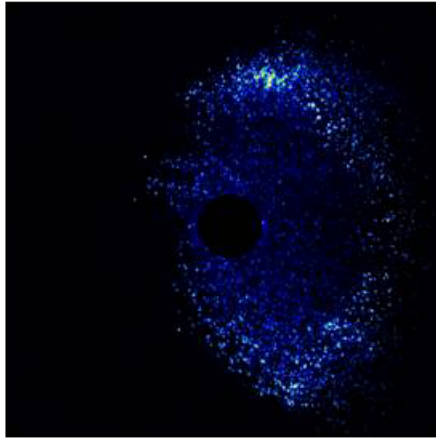Delay to PCO – 110ns
Laser Energy – 133mJ/pulse

Temp (K) – 446   Plane Height (mm)– 12.7
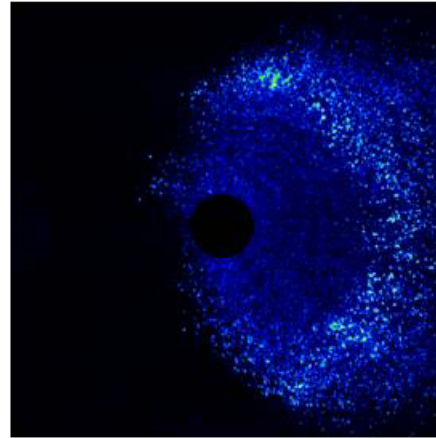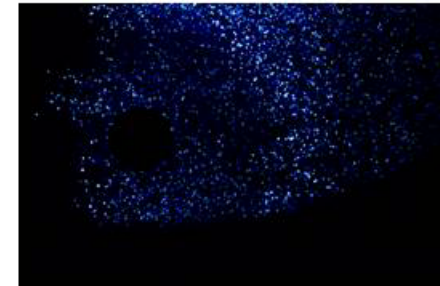Fuel Flow (kg/hr) – 26.76   Cross Flow Velocity (m/s) – 46

Test 19
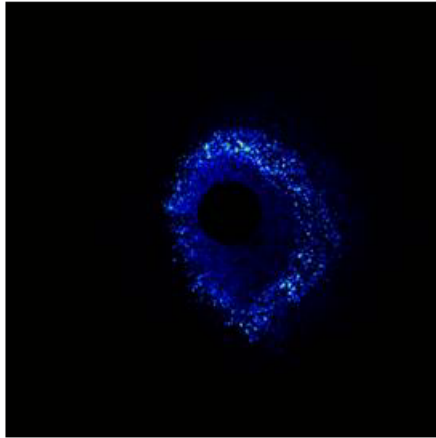
Fluorescence	Phosphorescence	Mie Scatter
[0 to 7000]	[0 to 3000]	[0 to 500]
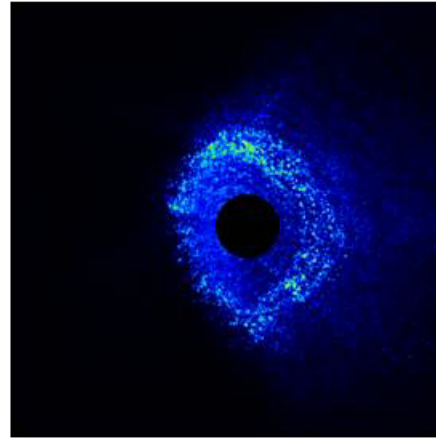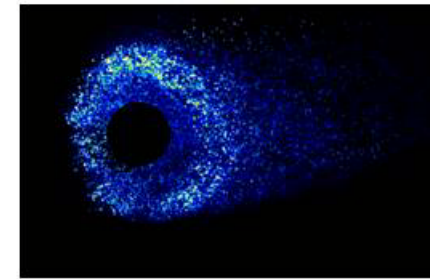
PCO Camera – 10ms exposure (first frame), f-stop: 2.8
Andor Camera – 20ms exposure, f-stop:16
Delay to PCO – 105ns
Laser Energy – 133mJ/pulse

Temp (K) – 446   Plane Height (mm)– 12.7
Fuel Flow (kg/hr) – 26.76   Cross Flow Velocity (m/s) – 46

Test 20
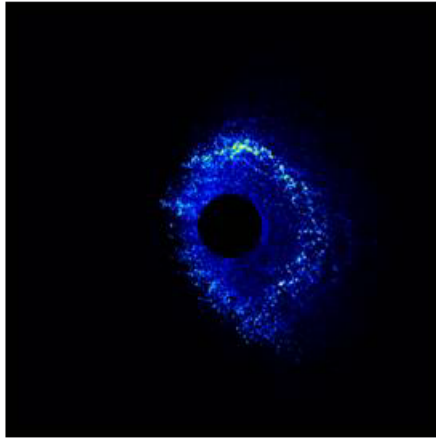
Fluorescence
[0 to 5000]
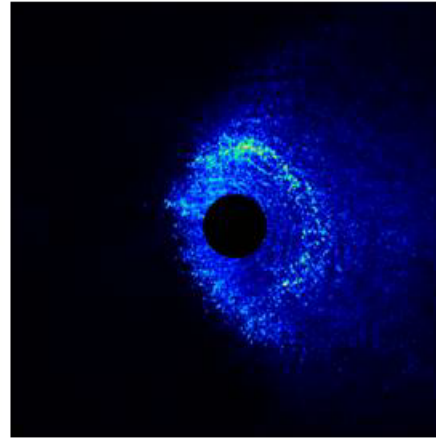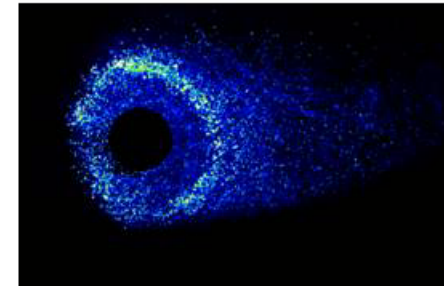
Phosphorescence
[0 to 3000]

Mie Scatter
[0 to 500]

PCO Camera – 10ms exposure (first frame), f-stop: 2.8
Andor Camera – 20ms exposure, f-stop:16
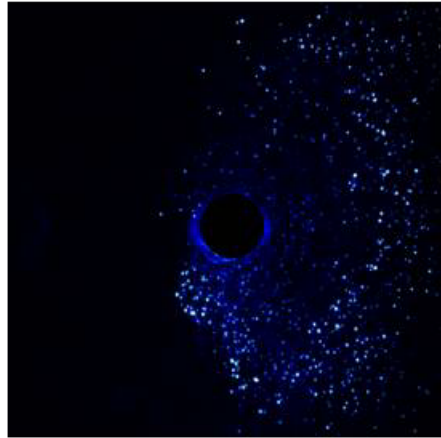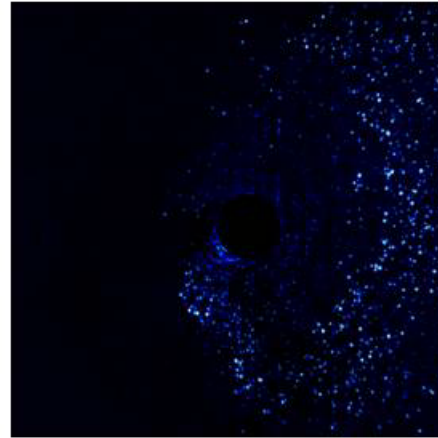Delay to PCO – 100ns
Laser Energy – 133mJ/pulse

Temp (K) – 446   Plane Height (mm)– 12.7
Fuel Flow (kg/hr) – 26.76   Cross Flow Velocity (m/s) – 46

Test 21
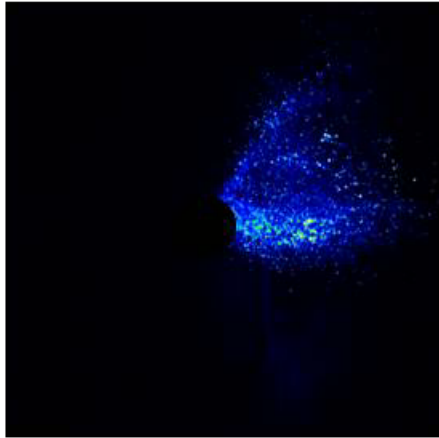
Fluorescence	Phosphorescence	Mie Scatter
[0 to 3000]	[0 to 3000]	[0 to 500]

PCO Camera – 10ms exposure (first frame), f-stop: 2.8

Andor Camera – 20ms exposure, f-stop:16

Delay to PCO – 100ns

Laser Energy – 133mJ/pulse

Temp (K) – 446	Plane Height (mm)– 12.7
Fuel Flow (kg/hr) – 10.89	Cross Flow Velocity (m/s) – 46

Test 22

Fluorescence	Phosphorescence	Mie Scatter
[0 to 6000]	[0 to 2000]	[0 to 500]

PCO Camera – 10ms exposure (first frame), f-stop: 2.8
Andor Camera – 20ms exposure, f-stop: 16
Delay to PCO – 100ns
Laser Energy – 133mJ/pulse

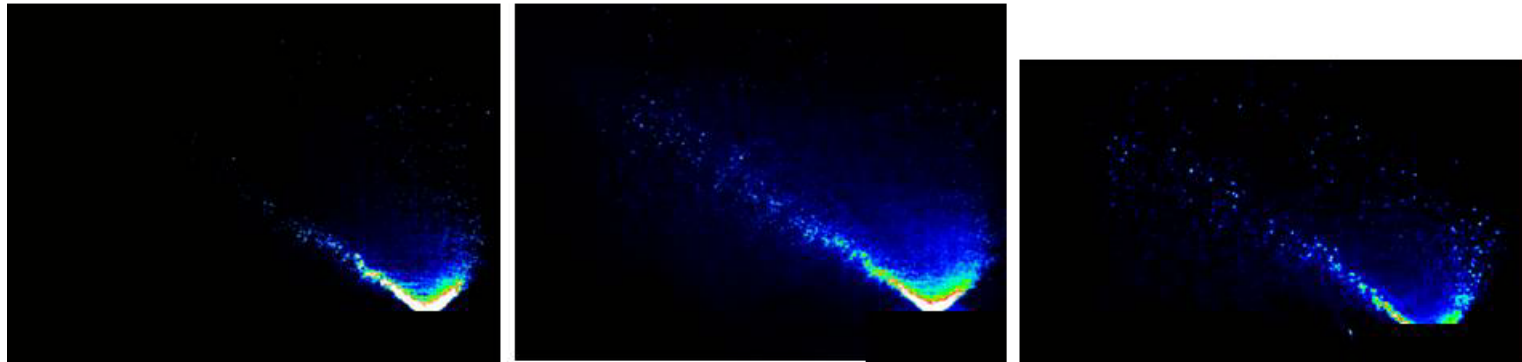Temp (K) – 557   Plane Height (mm)– 12.7
Fuel Flow (kg/hr) – 18.60   Cross Flow Velocity (m/s) – 31

Test 23
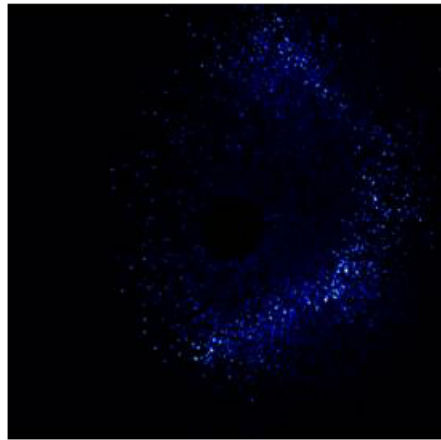
Fluorescence	Phosphorescence	Mie Scatter
[0 to 3000]	[0 to 3000]	[0 to 500]

PCO Camera – 10ms exposure (first frame), f-stop: 2.8
Andor Camera – 20ms exposure, f-stop:16
Delay to PCO – 100ns
Laser Energy – 133mJ/pulse

Temp (K) – 557	Plane Height (mm) – 25.4
Fuel Flow (kg/hr) – 18.60	Cross Flow Velocity (m/s) – 30

Test 24

Fluorescence	Phosphorescence	Mie Scatter
[0 to 2000]	[0 to 2000]	[0 to 500]

PCO Camera – 10ms exposure (first frame), f-stop: 2.8
Andor Camera – 20ms exposure, f-stop:16
Delay to PCO – 100ns
Laser Energy – 133mJ/pulse

Temp (K) – 444   Plane Height (mm)– 25.4
Fuel Flow (kg/hr) – 10.89 Cross Flow Velocity (m/s) – 46

Test 25

Fluorescence	Phosphorescence	Mie Scatter
[0 to 2000]	[0 to 2000]	[0 to 500]

PCO Camera – 10ms exposure (first frame), f-stop: 2.8
Andor Camera – 20ms exposure, f-stop:16
Delay to PCO – 100ns
Laser Energy – 133mJ/pulse

Temp (K) – 446   Plane Height (mm)– 25.4
Fuel Flow (kg/hr) – 26.76 Cross Flow Velocity (m/s) – 46

Test 26

Fluorescence
[0 to 2000]

Phosphorescence
[0 to 2000]

Mie Scatter
[0 to 500]

PCO Camera – 10ms exposure (first frame), f-stop: 2.8
Andor Camera – 20ms exposure, f-stop:16
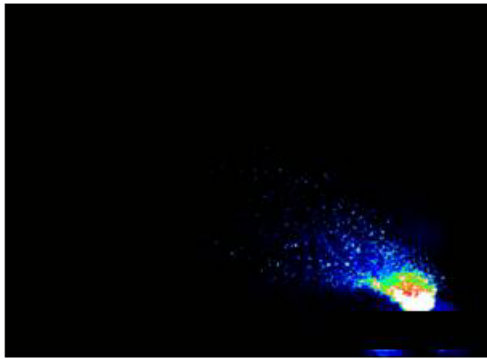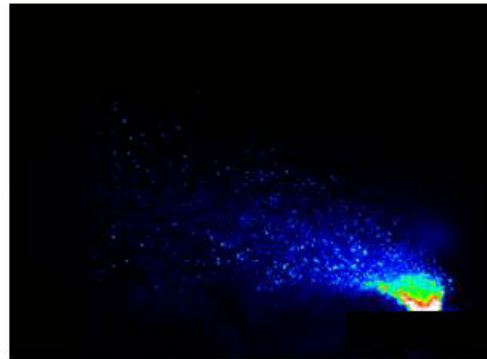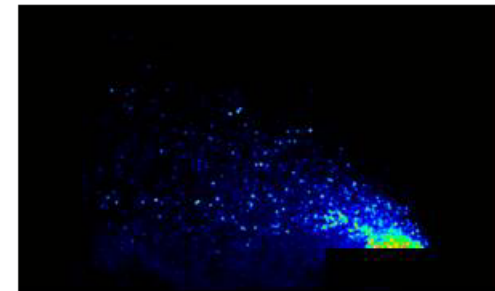Delay to PCO – 100ns
Laser Energy – 133mJ/pulse

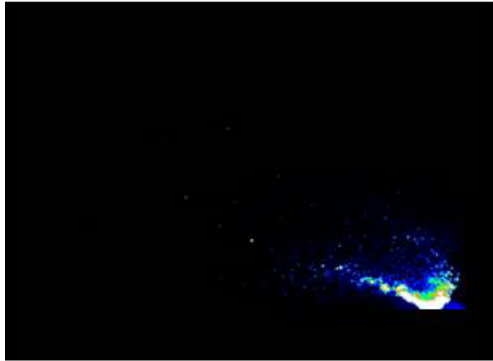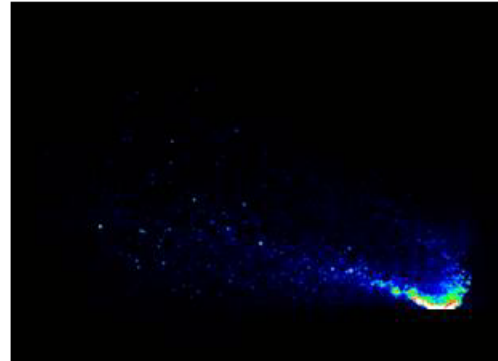**Temp (K) – 449**   **Plane Height (mm)– 25.4**
Fuel Flow (kg/hr) – 9.07 **Cross Flow Velocity (m/s) – 15**

A.2.2 Images of Vertical Planes through the Spray

Test Name	Fuel Flow Rate		Cross Flow Temperature		Plane Distance to Centerline		Cross Flow Velocity		Variable Delay*	
Test 27	26.76	kg/hr	446	K	0.015	mm	46	m/s	100	ns
Test 28	10.89	kg/hr	446	K	0.015	mm	46	m/s	100	ns
Test 29	10.89	kg/hr	554	K	0.015	mm	46	m/s	100	ns
Test 30	10.89	kg/hr	555	K	0.015	mm	46	m/s	100	ns
Test 31	10.89	kg/hr	557	K	6.019	mm	46	m/s	100	ns
Test 32	10.89	kg/hr	557	K	6.019	mm	46	m/s	100	ns
Test 33	10.89	kg/hr	557	K	12.023	mm	46	m/s	100	ns
Test 34	10.89	kg/hr	557	K	12.023	mm	46	m/s	100	ns
Test 35	10.89	kg/hr	557	K	25.026	mm	46	m/s	100	ns
Test 36	10.89	kg/hr	557	K	25.026	mm	46	m/s	100	ns
Test 37	10.89	kg/hr	557	K	-6.026	mm	46	m/s	100	ns
Test 38	10.89	kg/hr	557	K	-6.026	mm	46	m/s	100	ns
Test 39	10.89	kg/hr	557	K	-12.025	mm	46	m/s	100	ns
Test 40	10.89	kg/hr	557	K	-12.025	mm	46	m/s	100	ns
Test 41	10.89	kg/hr	557	K	-25.028	mm	46	m/s	100	ns
Test 42	10.89	kg/hr	557	K	-25.028	mm	46	m/s	100	ns
Test 43	10.89	kg/hr	443	K	6.031	mm	46	m/s	100	ns
Test 44	26.76	kg/hr	444	K	6.031	mm	46	m/s	100	ns
Test 45	26.76	kg/hr	444	K	12.034	mm	46	m/s	100	ns
Test 46	26.76	kg/hr	445	K	12.034	mm	46	m/s	100	ns
Test 47	10.89	kg/hr	445	K	25.037	mm	46	m/s	100	ns
Test 48	26.76	kg/hr	446	K	25.037	mm	46	m/s	100	ns
Test 49	26.76	kg/hr	446	K	-25.037	mm	46	m/s	100	ns
Test 50	10.89	kg/hr	446	K	-25.037	mm	46	m/s	100	ns
Test 51	10.89	kg/hr	446	K	-12.033	mm	46	m/s	100	ns
Test 52	26.76	kg/hr	446	K	-12.033	mm	46	m/s	100	ns
Test 53	26.76	kg/hr	446	K	-6.029	mm	46	m/s	100	ns
Test 54	10.89	kg/hr	446	K	-6.029	mm	46	m/s	100	ns

* (Note on Variable Delay) – Refer to Figure 11 for physical clarification.

Test 27

Fluorescence	Phosphorescence	Mie Scatter
[0 to 5000]	[0 to 5000]	[0 to 2000]

PCO Camera – 10ms exposure (first frame), f-stop: 2.8
Andor Camera – 20ms exposure, f-stop:16
Delay to PCO – 100ns
Laser Energy – 133mJ/pulse

|	
Temp (K) – 446	Plane Location (mm) – y = 0.015
Fuel Flow (kg/hr) – 26.76	Cross Flow Velocity (m/s) – 46

Test 28

Fluorescence	Phosphorescence	Mie Scatter
[0 to 5000]	[0 to 5000]	[0 to 2000]

PCO Camera – 10ms exposure (first frame), f-stop: 2.8
Andor Camera – 20ms exposure, f-stop:16
Delay to PCO – 100ns
Laser Energy – 133mJ/pulse

Temp (K) – 446   Plane Location (mm) – y = 0.015
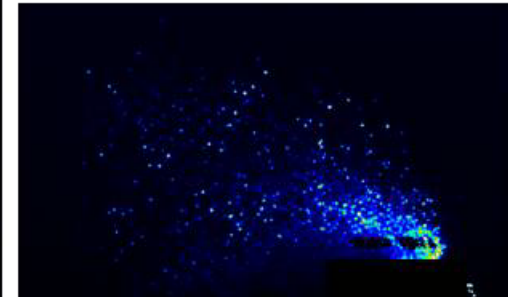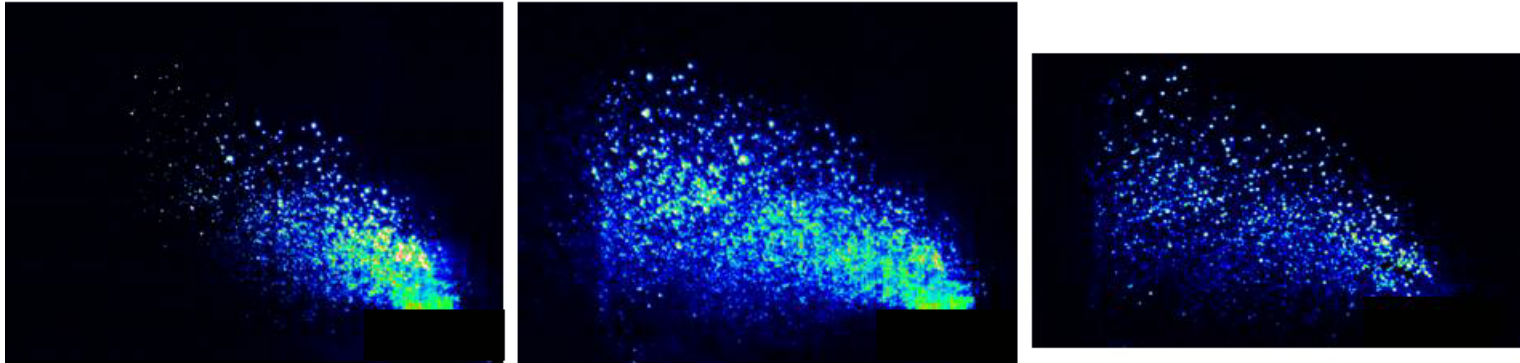Fuel Flow (kg/hr) – 10.89   Cross Flow Velocity (m/s) – 46

Test 29

| **Fluorescence** | **Phosphorescence** | **Mie Scatter** |
| [0 to 5000] | [0 to 5000] | [0 to 2000] |

PCO Camera – 10ms exposure (first frame), f-stop: 2.8
Andor Camera – 20ms exposure, f-stop:16
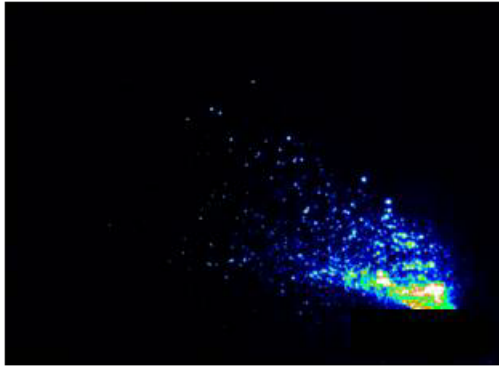Delay to PCO – 100ns
Laser Energy – 133mJ/pulse

Temp (K) – 554   Plane Location (mm) – y = 0.015
Fuel Flow (kg/hr) – 10.89 Cross Flow Velocity (m/s) – 46

Test 30

Fluorescence	Phosphorescence	Mie Scatter
[0 to 5000]	[0 to 5000]	[0 to 2000]

PCO Camera – 10ms exposure (first frame), f-stop: 2.8
Andor Camera – 20ms exposure, f-stop:16
Delay to PCO – 100ns
Laser Energy – 133mJ/pulse
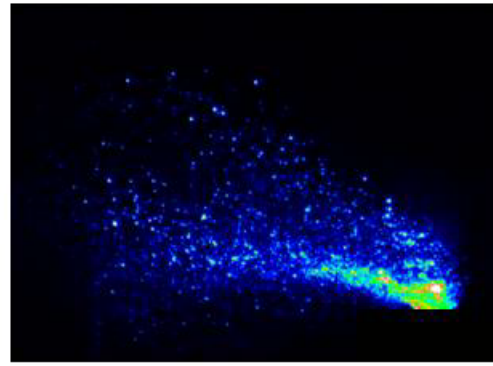
Temp (K) – 555   Plane Location (mm) – y = 0.015
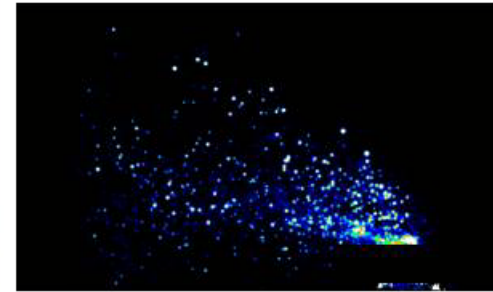Fuel Flow (kg/hr) – 10.89   Cross Flow Velocity (m/s) – 46

Test 31

Fluorescence	Phosphorescence	Mie Scatter
[0 to 5000]	[0 to 5000]	[0 to 2000]

PCO Camera – 10ms exposure (first frame), f-stop: 2.8
Andor Camera – 20ms exposure, f-stop:16
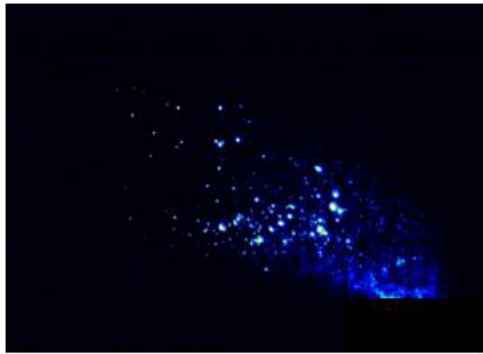Delay to PCO – 100ns
Laser Energy – 133mJ/pulse
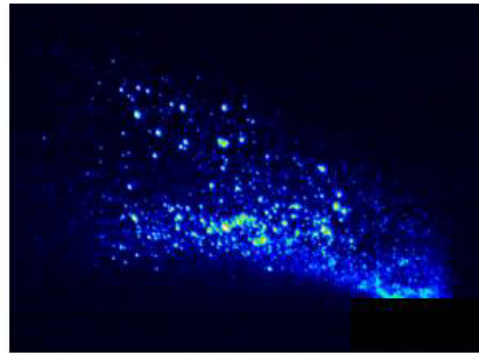
Temp (K) – 557   Plane Location (mm) – y = 6.019
Fuel Flow (kg/hr) – 10.89   Cross Flow Velocity (m/s) – 46

Test 32
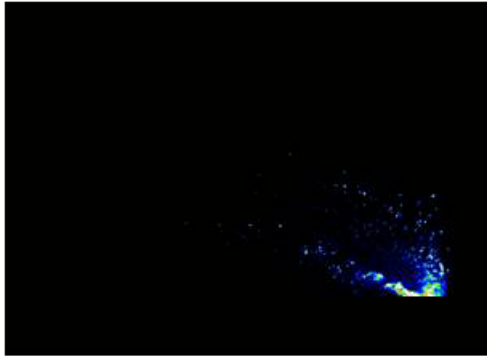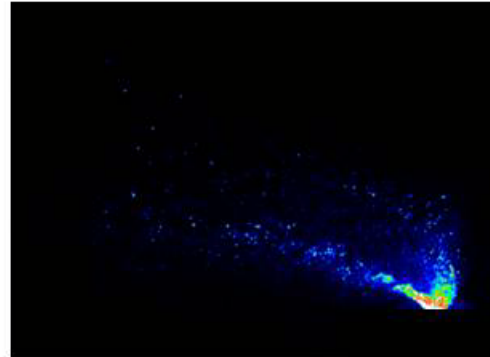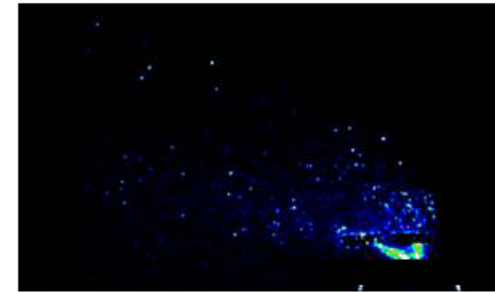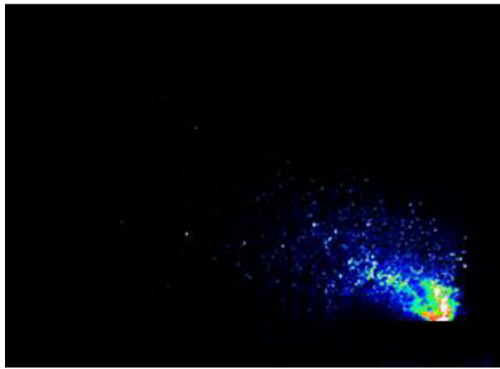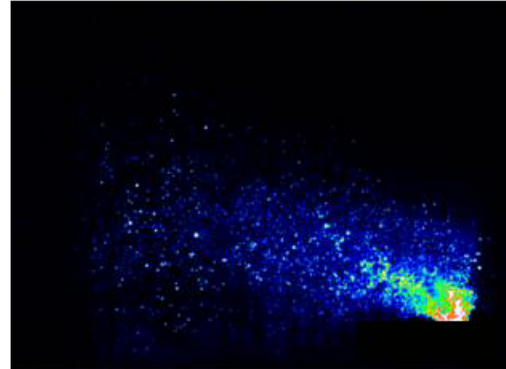
| Fluorescence
[0 to 5000] | Phosphorescence
[0 to 2000] | Mie Scatter
[0 to 2000] |

PCO Camera – 10ms exposure (first frame), f-stop: 2.8
Andor Camera – 20ms exposure, f-stop:16
Delay to PCO – 100ns
Laser Energy – 133mJ/pulse

Temp (K) – 557   Plane Location (mm) – y = 6.019
Fuel Flow (kg/hr) – 10.89   Cross Flow Velocity (m/s) – 46

Test 33

Fluorescence	Phosphorescence	Mie Scatter
[0 to 1000]	[0 to 1000]	[0 to 500]

PCO Camera – 10ms exposure (first frame), f-stop: 2.8
Andor Camera – 20ms exposure, f-stop:16
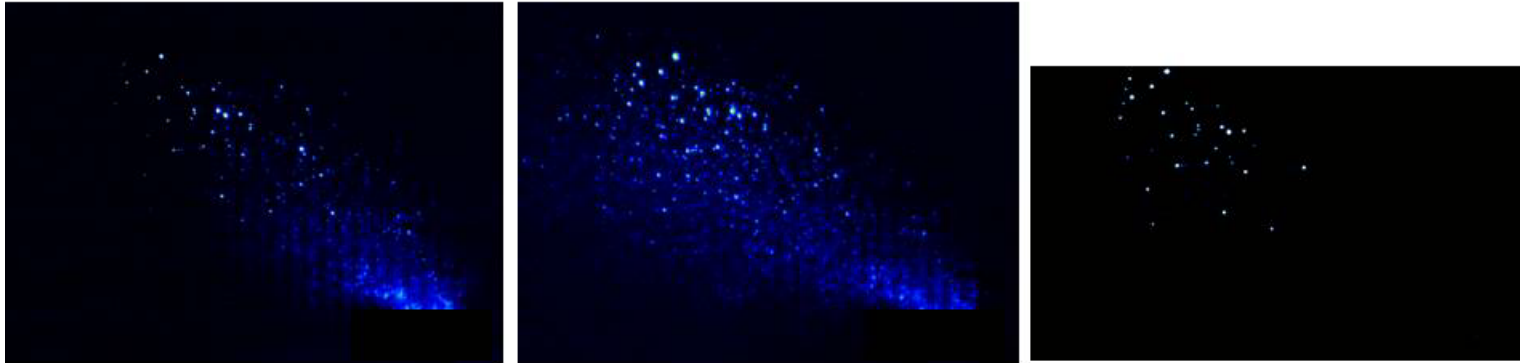Delay to PCO – 100ns
Laser Energy – 133mJ/pulse

Temp (K) – 557	Plane Location (mm) – y = 12.023
Fuel Flow (kg/hr) – 10.89	Cross Flow Velocity (m/s) – 46

Test 34

Fluorescence
[0 to 2000]

Phosphorescence
[0 to 2000]

Mie Scatter
[0 to 500]

PCO Camera – 10ms exposure (first frame), f-stop: 2.8
Andor Camera – 20ms exposure, f-stop:16
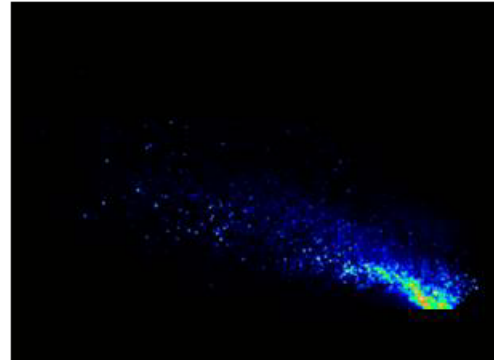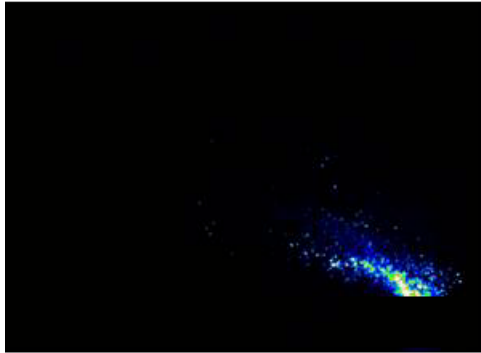Delay to PCO – 100ns
Laser Energy – 133mJ/pulse

Temp (K) – 557   Plane Location (mm) – y = 12.023
Fuel Flow (kg/hr) – 10.89   Cross Flow Velocity (m/s) – 46

Test 35

Fluorescence	Phosphorescence	Mie Scatter
[0 to 1000]	[0 to 1000]	[0 to 500]

PCO Camera – 10ms exposure (first frame), f-stop: 2.8
Andor Camera – 20ms exposure, f-stop:16
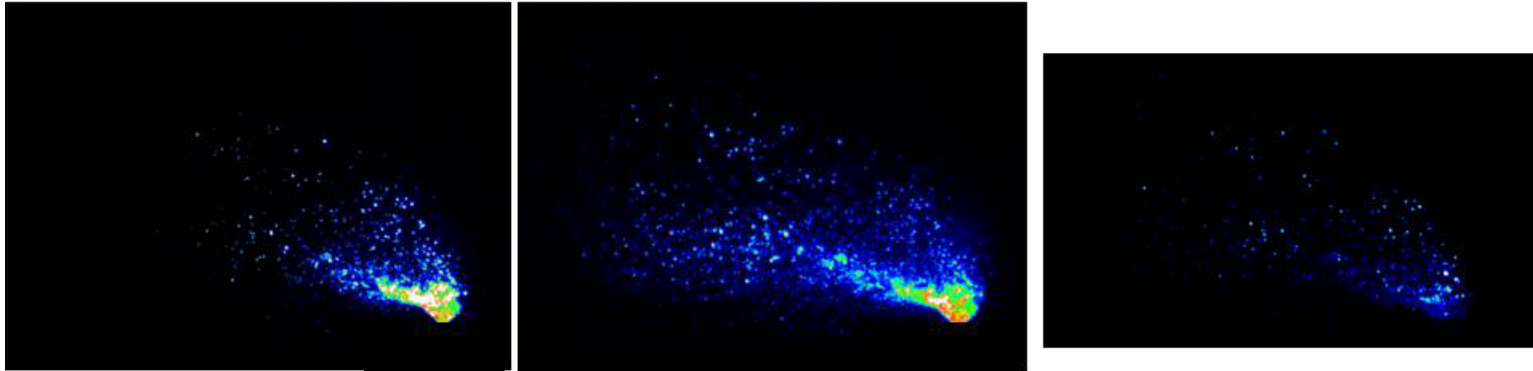Delay to PCO – 100ns
Laser Energy – 133mJ/pulse

Temp (K) – 557   Plane Location (mm) – y = 25.026
Fuel Flow (kg/hr) – 10.89   Cross Flow Velocity (m/s) – 46

Test 36

Fluorescence
[0 to 1000]

Phosphorescence
[0 to 1000]

Mie Scatter
[0 to 500]

PCO Camera — 10ms exposure (first frame), f-stop: 2.8
Andor Camera — 20ms exposure, f-stop:16
Delay to PCO — 100ns
Laser Energy — 133mJ/pulse

Temp (K) — 557   Plane Location (mm) — y = 25.026
Fuel Flow (kg/hr) — 10.89   Cross Flow Velocity (m/s) — 46

Test 37

Fluorescence
[0 to 3000]

Phosphorescence
[0 to 3000]

Mie Scatter
[0 to 1000]

PCO Camera – 10ms exposure (first frame), f-stop: 2.8
Andor Camera – 20ms exposure, f-stop:16
Delay to PCO – 100ns
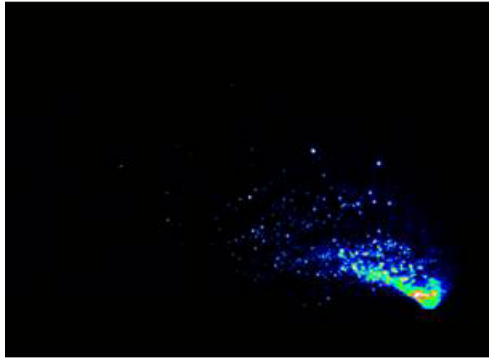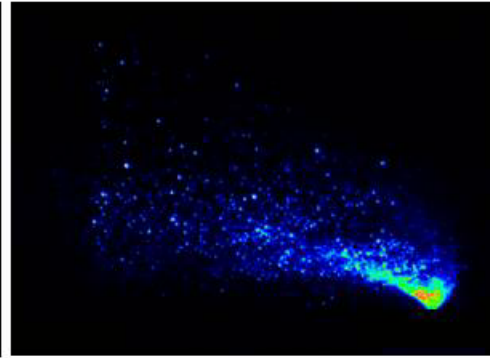Laser Energy – 133mJ/pulse

Temp (K) – 557   Plane Location (mm) – y = -6.026
Fuel Flow (kg/hr) – 10.89 Cross Flow Velocity (m/s) – 46

Test 38

Fluorescence	Phosphorescence	Mie Scatter
[0 to 3000]	[0 to 3000]	[0 to 1000]

PCO Camera – 10ms exposure (first frame), f-stop: 2.8
Andor Camera – 20ms exposure, f-stop:16
Delay to PCO – 100ns
Laser Energy – 133mJ/pulse

Temp (K) – 557   Plane Location (mm) – y = -6.026
Fuel Flow (kg/hr) – 10.89   Cross Flow Velocity (m/s) – 46

Test 39

Fluorescence	Phosphorescence	Mie Scatter
[0 to 3000]	[0 to 3000]	[0 to 1000]

PCO Camera – 10ms exposure (first frame), f-stop: 2.8
Andor Camera – 20ms exposure, f-stop:16
Delay to PCO – 100ns
Laser Energy – 133mJ/pulse

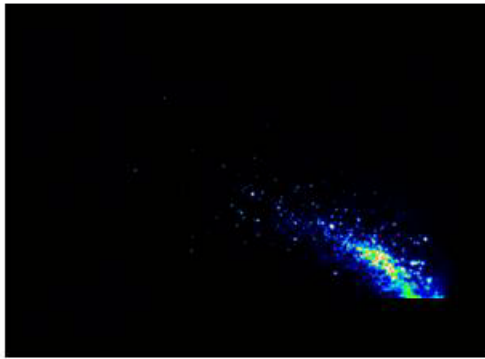Temp (K) – 557   Plane Location (mm) – y = -12.025
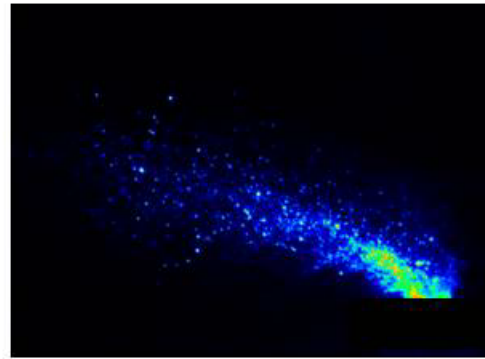Fuel Flow (kg/hr) – 10.89   Cross Flow Velocity (m/s) – 46

Test 40
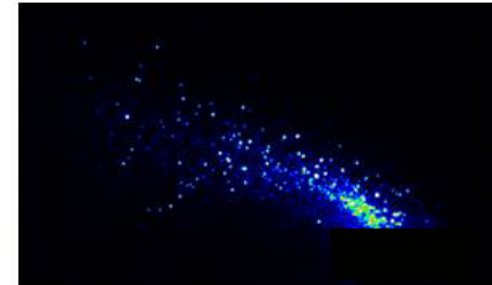

Fluorescence	Phosphorescence	Mie Scatter
[0 to 3000]	[0 to 3000]	[0 to 500]

PCO Camera – 10ms exposure (first frame), f-stop: 2.8
Andor Camera – 20ms exposure, f-stop:16
Delay to PCO – 100ns
Laser Energy – 133mJ/pulse

Temp (K) – 557   Plane Location (mm) – y = -12.025
Fuel Flow (kg/hr) – 10.89   Cross Flow Velocity (m/s) – 46

Test 41

Fluorescence	Phosphorescence	Mie Scatter
[0 to 3000]	[0 to 3000]	[0 to 500]

PCO Camera – 10ms exposure (first frame), f-stop: 2.8
Andor Camera – 20ms exposure, f-stop:16
Delay to PCO – 100ns
Laser Energy – 133mJ/pulse
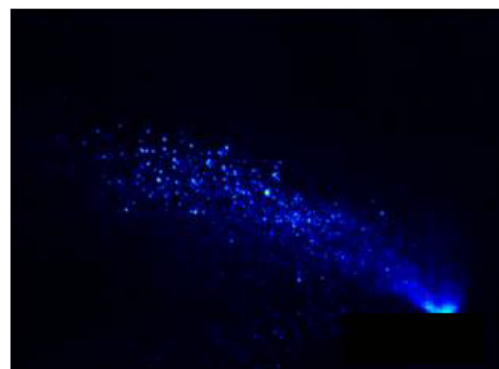
Temp (K) – 557   Plane Location (mm) – y = -25.028
Fuel Flow (kg/hr) – 10.89   Cross Flow Velocity (m/s) – 46

Test 42

Fluorescence
[0 to 3000]

Phosphorescence
[0 to 3000]

Mie Scatter
[0 to 500]

PCO Camera – 10ms exposure (first frame), f-stop: 2.8
Andor Camera – 20ms exposure, f-stop:16
Delay to PCO – 100ns
Laser Energy – 133mJ/pulse

Temp (K) – 557   Plane Location (mm) – y = -25.028
Fuel Flow (kg/hr) – 10.89   Cross Flow Velocity (m/s) – 46

Test 43

Fluorescence	Phosphorescence	Mie Scatter
[0 to 3000]	[0 to 3000]	[0 to 1000]

PCO Camera – 10ms exposure (first frame), f-stop: 2.8
Andor Camera – 20ms exposure, f-stop:16
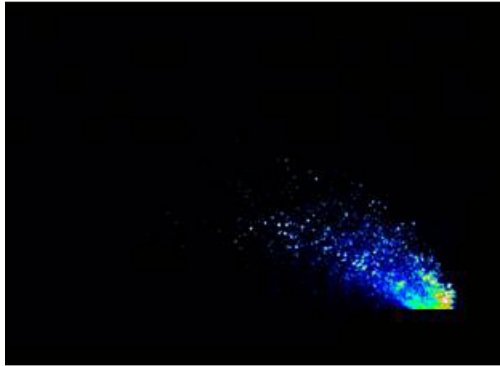Delay to PCO – 100ns
Laser Energy – 133mJ/pulse
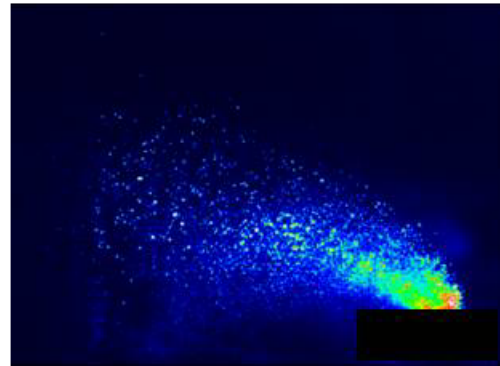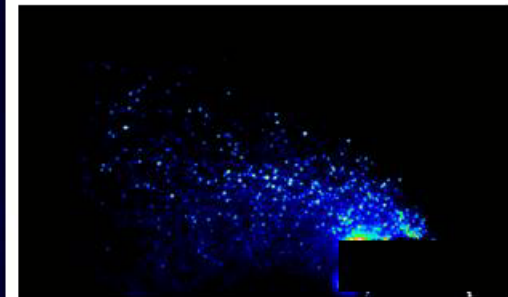
Temp (K) – 443   Plane Location (mm) – $y = 6.031$
Fuel Flow (kg/hr) – 10.89   Cross Flow Velocity (m/s) – 46

Test 44

Fluorescence	Phosphorescence	Mie Scatter
[0 to 3000]	[0 to 3000]	[0 to 1000]

PCO Camera – 10ms exposure (first frame), f-stop: 2.8
Andor Camera – 20ms exposure, f-stop:16
Delay to PCO – 100ns
Laser Energy – 133mJ/pulse

Temp (K) – 444   Plane Location (mm) – y = 6.031
Fuel Flow (kg/hr) – 26.76   Cross Flow Velocity (m/s) – 46

Test 45

Fluorescence	Phosphorescence	Mie Scatter
[0 to 3000]	[0 to 3000]	[0 to 1000]

PCO Camera – 10ms exposure (first frame), f-stop: 2.8
Andor Camera – 20ms exposure, f-stop:16
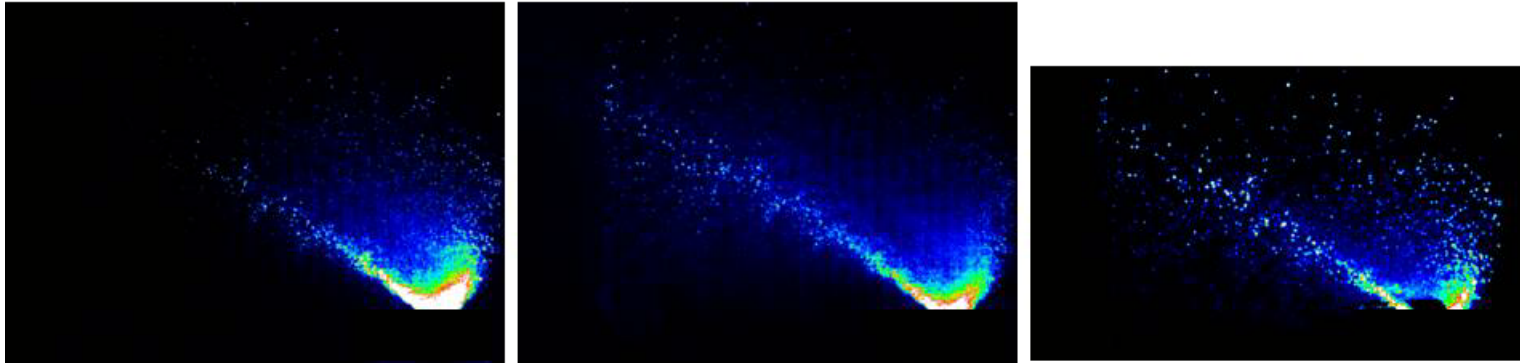Delay to PCO – 100ns
Laser Energy – 133mJ/pulse

Temp (K) – 444   Plane Location (mm) – y = 12.034
Fuel Flow (kg/hr) – 26.76   Cross Flow Velocity (m/s) – 46

Test 46

Fluorescence	Phosphorescence	Mie Scatter
[0 to 1000]	[0 to 1000]	[0 to 500]

PCO Camera – 10ms exposure (first frame), f-stop: 2.8
Andor Camera – 20ms exposure, f-stop:16
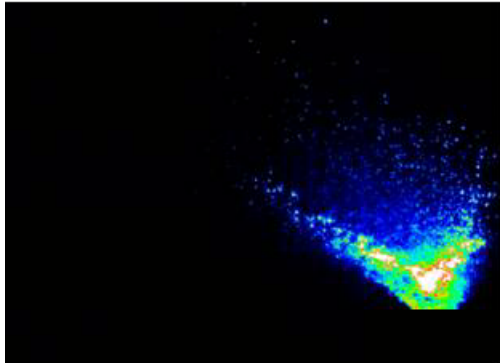Delay to PCO – 100ns
Laser Energy – 133mJ/pulse
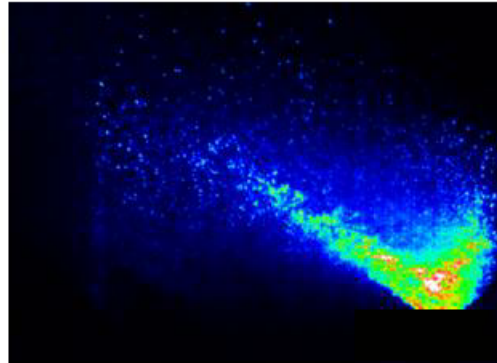
Temp (K) – 445   Plane Location (mm) – y = 12.034
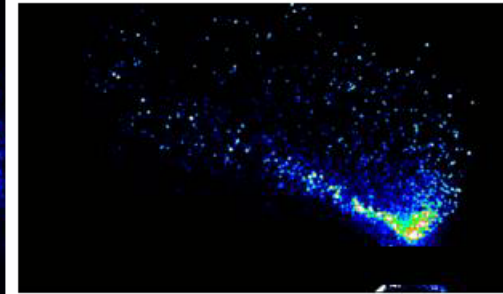Fuel Flow (kg/hr) – 26.76   Cross Flow Velocity (m/s) – 46

Test 47

Fluorescence	Phosphorescence	Mie Scatter
[0 to 500]	[0 to 500]	[0 to 500]

PCO Camera – 10ms exposure (first frame), f-stop: 2.8
Andor Camera – 20ms exposure, f-stop:16
Delay to PCO – 100ns
Laser Energy – 133mJ/pulse

Temp (K) – 445   Plane Location (mm) – y = 25.037
Fuel Flow (kg/hr) – 10.89   Cross Flow Velocity (m/s) – 46

Test 48

Fluorescence	Phosphorescence	Mie Scatter
[0 to 1000]	[0 to 1000]	[0 to 500]

PCO Camera – 10ms exposure (first frame), f-stop: 2.8
Andor Camera – 20ms exposure, f-stop:16
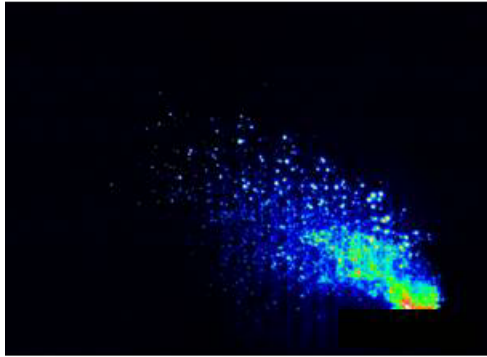Delay to PCO – 100ns
Laser Energy – 133mJ/pulse
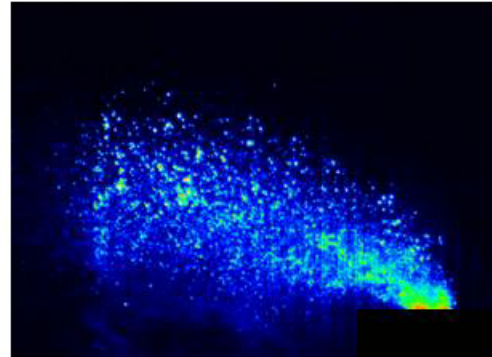
Temp (K) – 446   Plane Location (mm) – y = 25.037
Fuel Flow (kg/hr) – 26.76   Cross Flow Velocity (m/s) – 46

Test 49

Fluorescence	Phosphorescence	Mie Scatter
[0 to 3000]	[0 to 3000]	[0 to 500]

PCO Camera – 10ms exposure (first frame), f-stop: 2.8
Andor Camera – 20ms exposure, f-stop:16
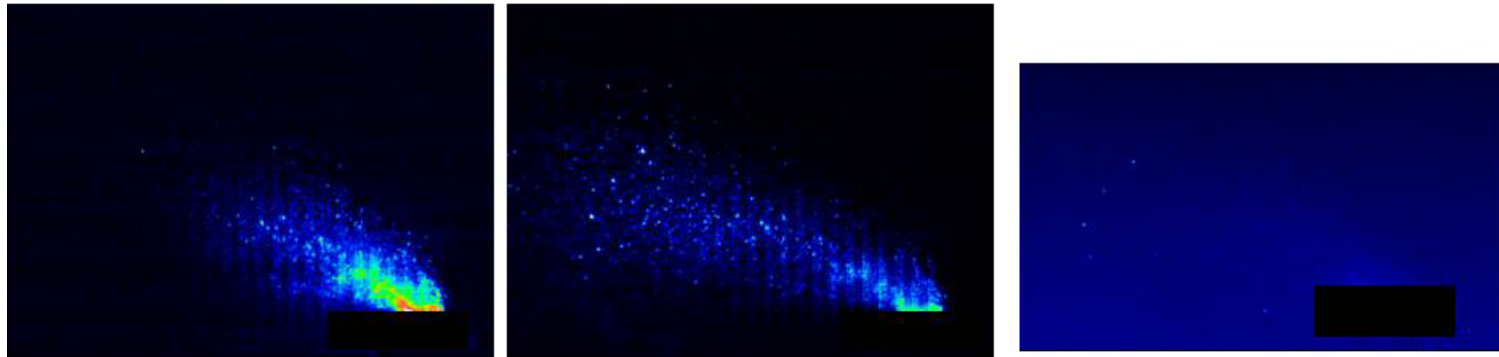Delay to PCO – 100ns
Laser Energy – 133mJ/pulse

Temp (K) – 446   Plane Location (mm) – y = -25.037
Fuel Flow (kg/hr) – 26.76   Cross Flow Velocity (m/s) – 46

Test 50

Fluorescence	Phosphorescence	Mie Scatter
[0 to 1000]	[0 to 1000]	[0 to 500]

PCO Camera – 10ms exposure (first frame), f-stop: 2.8
Andor Camera – 20ms exposure, f-stop:16
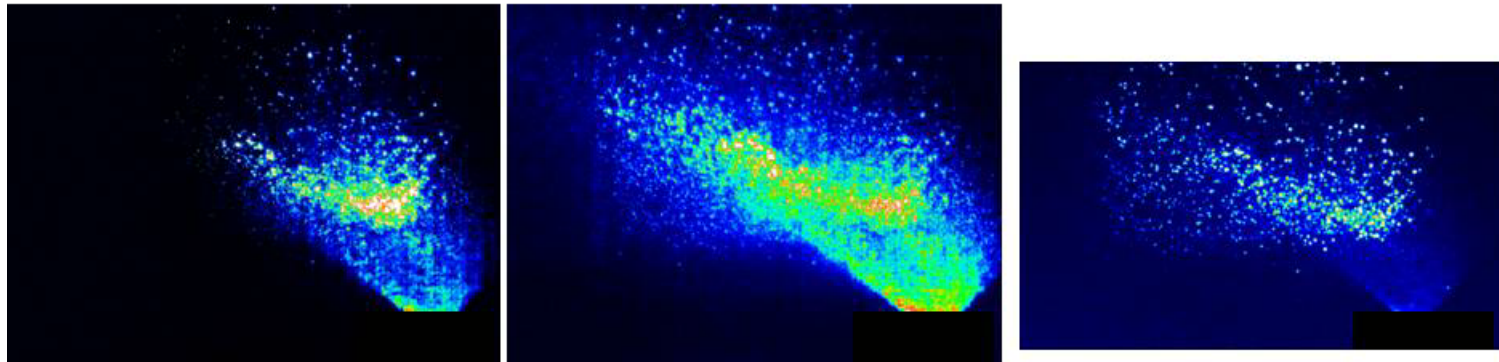Delay to PCO – 100ns
Laser Energy – 133mJ/pulse

Temp (K) – 446	Plane Location (mm) – y = -25.037
Fuel Flow (kg/hr) – 10.89	Cross Flow Velocity (m/s) – 46

Test 51

Fluorescence   Phosphorescence

[0 to 3000]   PCO Camera – 10ms exposure (first frame), f-stop: 2.8

Andor Camera – 20ms exposure, f-stop:16

Delay to PCO – 100ns

Laser Energy – 133mJ/pulse

Temp (K) – 446   Plane Location (mm) – y = -12.033

Fuel Flow (kg/hr) – 10.89   Cross Flow Velocity (m/s) – 46

118

Test 52

Fluorescence
[0 to 3000]

Phosphorescence
[0 to 3000]

Mie Scatter
[0 to 500]

PCO Camera – 10ms exposure (first frame), f-stop: 2.8
Andor Camera – 20ms exposure, f-stop:16
Delay to PCO – 100ns
Laser Energy – 133mJ/pulse

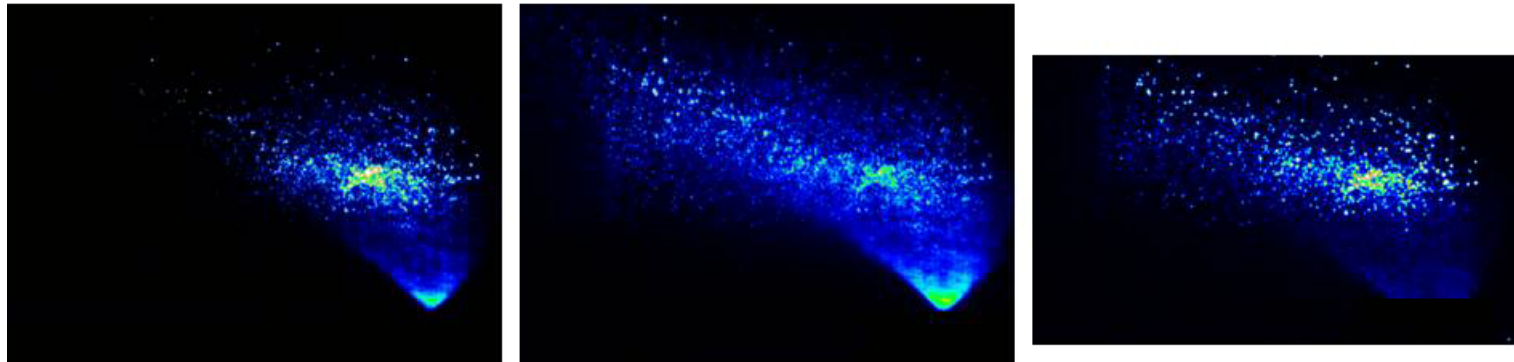Temp (K) – 446   Plane Location (mm) – y = -12.033
Fuel Flow (kg/hr) – 26.76   Cross Flow Velocity (m/s) – 46

Test 53
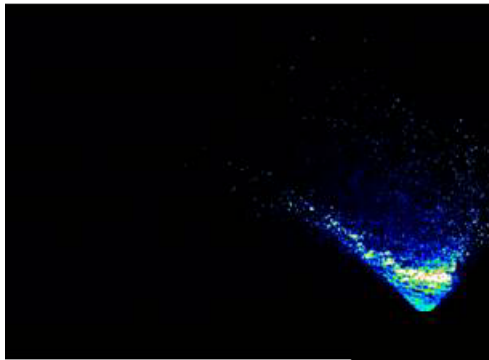
Fluorescence	**Phosphorescence**	**Mie Scatter**
[0 to 3000]	[0 to 3000]	[0 to 500]
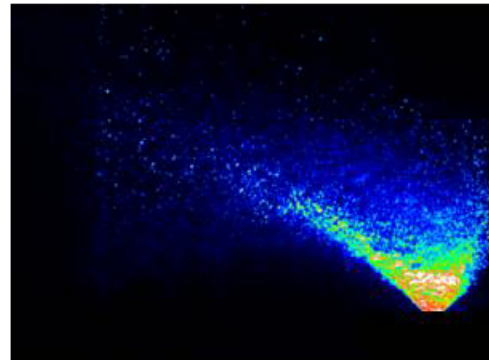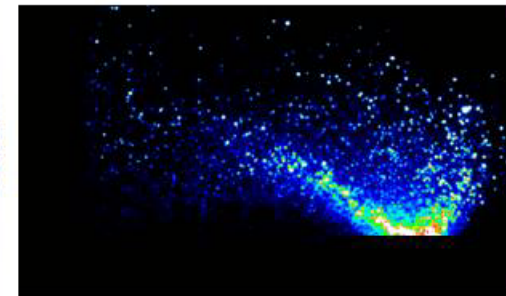
PCO Camera – 10ms exposure (first frame), f-stop: 2.8
Andor Camera – 20ms exposure, f-stop:16
Delay to PCO – 100ns
Laser Energy – 133mJ/pulse

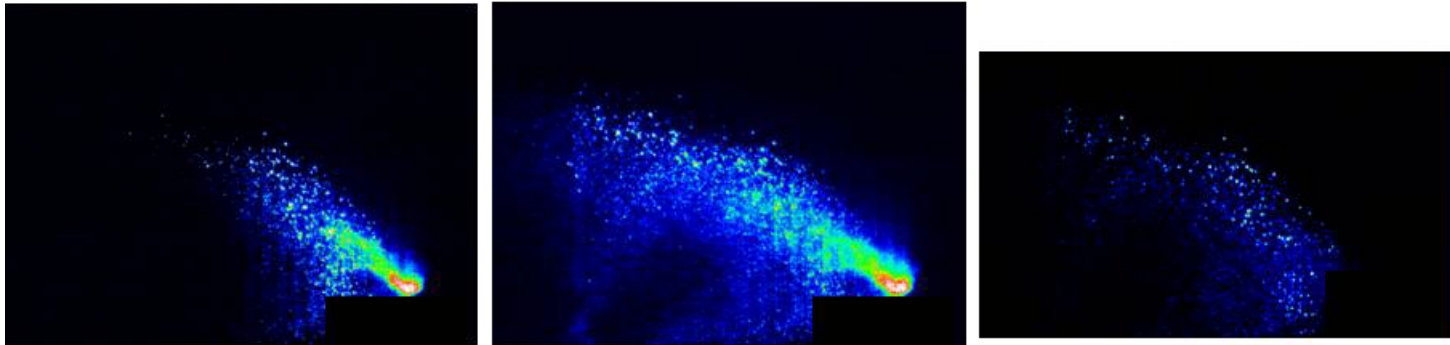Temp (K) – 446   Plane Location (mm) – y = -6.029
Fuel Flow (kg/hr) – 26.76   Cross Flow Velocity (m/s) – 46

Test 54
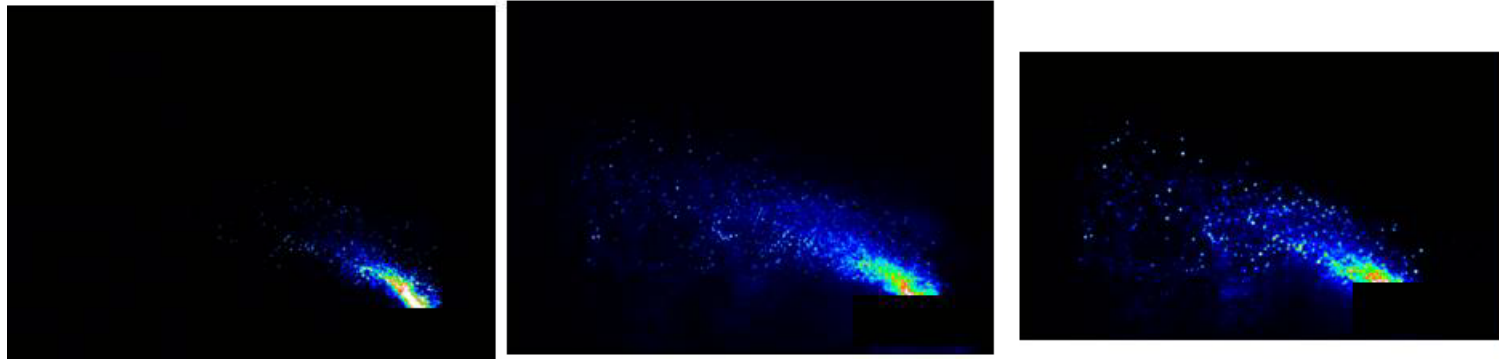
Fluorescence	Phosphorescence	Mie Scatter
[0 to 3000]	[0 to 3000]	[0 to 500]

PCO Camera – 10ms exposure (first frame), f-stop: 2.8
Andor Camera – 20ms exposure, f-stop:16
Delay to PCO – 100ns
Laser Energy – 133mJ/pulse

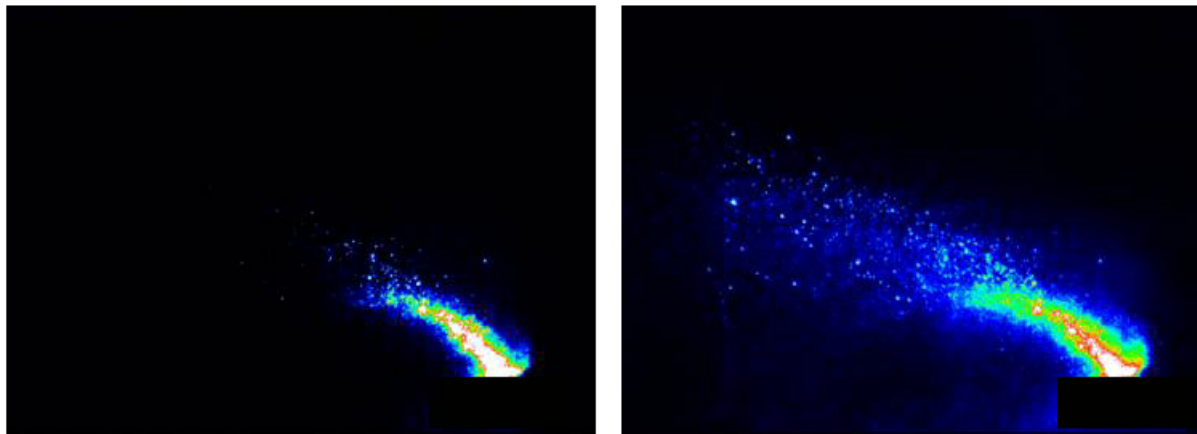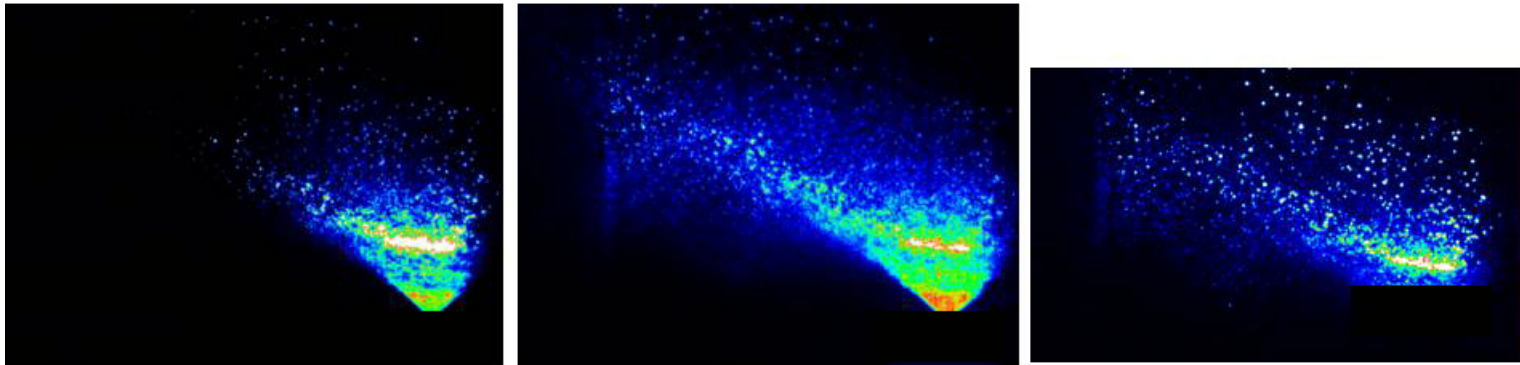Temp (K) – 446   Plane Location (mm) – y = -6.029
Fuel Flow (kg/hr) – 10.89   Cross Flow Velocity (m/s) – 46

A.3 Miscellaneous

R1.50

1.00

⌀4

1/8" NPT - 27
⌀.339 "R" TAP DRILL THRU.

4 X 1/4" - 20 TYP.
⌀.2101 "#7" TAP DRILL
▽ 0.75"

COMMENTS AND CONTACT INFO

DRAWN BY:
JACOB SCHMIDT
12 NOV 2007

CONTACT INFO:
507.213.0866
SCHMIDTJAKE@GMAIL.COM

ALL DIMENSIONS IN INCHES UNLESS
OTHERWISE NOTED.

MATERIAL: 6061 ALUMINUM

TITLE:

Injector Plate

SIZE **A** | DWG. NO. | REV

SCALE: 1:1 | WEIGHT: | SHEET 1 OF 1
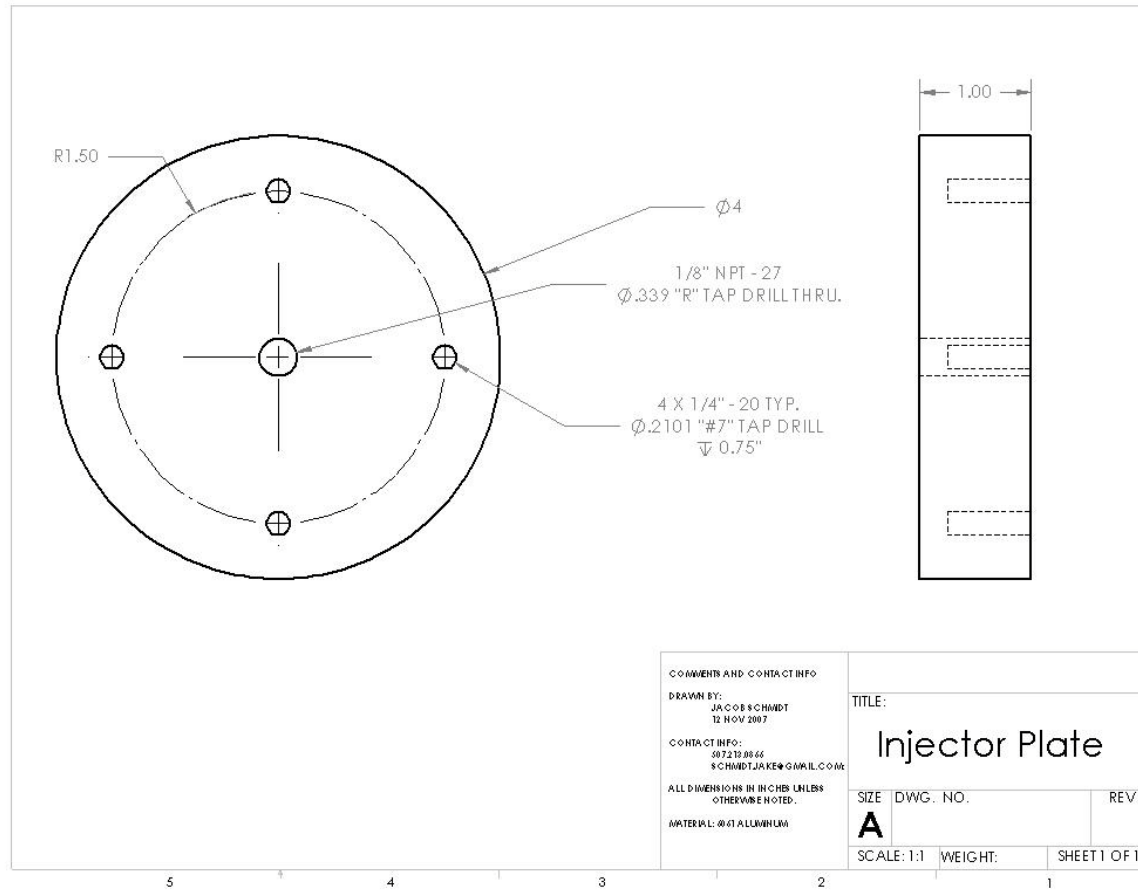
BIBLIOGRAPHY

Anon, untitled, Malvern Instruments Ltd, Malvern Worchester, England, 1983.

Bachalo, W. D., and Houser, M. J., "Analysis and Testing of a New Method for Drop Size Measurement Using Laser Light Scatter Interferometry," CR NAS3-23684, NASA Lewis Research Center, Nov. 1983.

Bachalo, W. D., Hess, C. F., and Hartwell, C. A., "An Instrument for Spray Droplet Size and Velocity Measurements, " Journal of Engineering for Power, Vol. 102, 1980, pp. 798-806.

Bachalo, W. D., Houser, M. J., and Smith, J. N., "Evolutionary Behavior of Sprays Produced by Pressure Atomizers," AIAA Paper 86-0296, 1986.

Baritaud, T. A., and Heinze, T. A., "Gasoline Distribution Measurements with PLIF in a SI Engine," SAE Technical Paper Series 922355, 1992.

Bazile, R. and Stepowski, D., "Measurement of vaporized and liquid fuel concentration filed in a burning spray of jet acetone using planar laser induced fluorescence," *Experiment in Fluids* Vol. 20, pp. 1-9.

Bogan, D.J. and Lee, D.H., "Triplet-State Chemiluminescence: Acetone T1 from the Decomposition of chemically Activated 3,3-Dimethy-4-(N,N-dimethylamino)-1,2-dioxetane," *The Journal of Physical Chemistry*, Vol. 95, No.4, 1991, pp. 1533-1535.

Borkman, R.F. and Kearns, D.R., "Triplet-State Energy Transfer in Liquid Solutions. Acetone-Photosensitized *cis-trans* Isomerization of pentene-2," *The Journal of the American Chemical Society*, Vol. 88, No. 15, 1966, pp. 3467-3475.

Bortolus, P., Dellonte, S., Faucitano, A., Gratani, F., "Photostabilizing Mechanisms of Hindered-Amine Light Stabilizers: Interaction with Electronically Excited Aliphatic Carbonyls," *Macromolecules*, Vol. 19, No.12, 1986, pp. 2916-2922.

Brown, M., Meyer, T., Gord, J., Belovich, V., and Roquemore, W., "Laser-Induced Incandescence Measurements in the Reaction Zone of a Model Gas Turbine Combustor," AIAA 2002-0393.

Bryant, R.A, Donbar, J.M., Driscoll, J.F., "Acetone Laser Induced Fluorescence for Low Pressure/Low Temperature Flow Visualization," *Experiments in Fluids*, Vol. 28, 2000, pp. 471-476.

Costela, A., Crespo, M.T., and Figuera, J.M., "Laser Photolysis of Acetone at 308nm," Journal of Photochemistry, Vol. 34, 1986, pp. 165-173.

Davy, M. H., Williams, P. A., and Anderson, R. W., "Effects of Fuel Composition on Mixture Formation in a Firing Direct-Injection Spark-Ignition (DISI) Engine: An Experimental Study Using Mie-Scattering and Planar Laser-Induced Fluorescence (PLIF) Techniques," SAE Technical Series 2000-01-1904.

Eckbreth, A. C., Laser Diagnostics for Combustion Temperature and Species, 1st ed., Abacus Press, Cambridge, Massachusetts. 1988

Emrich, M. and Warneck, P., "Photodissociation of Acetone in Air: Dependence on Pressure and Wavelength. Behavior of the Excited Singlet State," *Journal of Physical Chemistry A*, Vol. 104, No. 42, 2000, pp. 9436-9442.

Farmer, W. M., "Measurement of Particle Size, Number Density, and Velocity Using a Laser Interferometer," Applied Optics, Vol. 11, 1972, pp. 2603-2612.

Greenblatt, G.D., Ruhman, S., and Haas, Y., "Fluorescence Decay Kinetics of Acetone Vapour at Low Pressures," Chemical Physics Letters, Vol. 112, No. 3, 1984, pp. 200-206.

Haas, Y. and Yahav, G., "Infrared Laser Multiphoton Dissociation of Tetramethyldioxetane: Direct Observation of Triplet Acetone," *Journal of the American Chemical Society*, Vol. 100, No. 15, 1978, pp. 4885-4886.

Haas, Y., Ruhman, S., Greenblatt, G.D., and Anner, O., "Infrared Photochemistry of Tetramethyldioxetane. The Nature of Electronically Excited Products," *Journal of the American Chemical Society*, Vol. 107, 1985, pp. 5068-5074.

Hess, C. F., "A Technique Combining the Visibility of a Doppler Signal with the Peak Intensity of the Pedestal to Measure the Size and Velocity of Droplets in a Spray," AIAA Paper 84-0203, 1984.

Jermy, M. C., and Greenhalgh, D. A., "Planar drop sizing by elastic and fluorescence scattering in sprays too dense for phase Doppler measurement," Applied Physics B Vol. 71, 2000, pp. 703-710.

Kearney, S. P., Reyes, F.V., "Quantitative temperature imaging in gas-phase turbulent thermal convection by laser-induced fluorescence of acetone," Experiments in Fluids, Vol. 34, 2003, pp. 87-97.

Koch, J.D., Hanson, R.K, Koban, W., Schulz, C., "Rayleigh-calibrated fluorescence quantum yield measurements of acetone and 3-pentanone," *Applied Optics,* Vol. 43, No. 31, 2004, pp.5901-5910

Lofstom, C., Engstrom, J., Richter, M., Kaminski, C. F., Johansson, P., Nyholm, K., Hult, J., Nygren, J., and Alden, M., "Feasibility Studies and Application of Laser/Optical Diagnostics for Characterization of a Practical Low-Emission Gas Turbine Combustor," Proceedings of the ASME Turbo Expo 2000, ASME-GT2000-0124.

Lofstom, C., Kaaling, H., and Alden, M., "Visualization of Fuel Distributions in Premixed Ducts in a Low-Emission Gas Turbine Combustor using Laser Techniques," Twenty-sixth Symposium on Combustion, The Combustion Institute, 1996, pp. 2787-2793.

Lozano, A., "Laser-Excited Luminescent Tracers for Planar Concentration Measurements in Gaseous Jets," HTGL report no. T-284, Stanford University, Stanford, CA, August 1992.

Lucht, R. P., "Applications of laser-induced fluorescence spectroscopy for combustion and plasma diagnostics," *Laser Spectroscopy and its Applications*, L. J. Radzemski, R. W. Solarz and J. Paisner Eds., Marcel Dekker, New York, New York. 1987

Meyer, T. R., Roy, S., Belovich, V. M., Corporan, E., Gord, J. R., "Simultaneous planar laser-induced incandescence, OH planar laser-induced fluorescence, and droplet Mie scattering in swirl-stabilized spray flames," Applied Optics, Vol. 44, No. 3, 2005, pp. 445-454.

Pischel, U. and Nau, W., "Switch-Over in Photochemical Reaction Mechanism from Hydrogen Abstraction to Exciplex-Induced Quenching: Interaction of Triplet-Excited versus Singlet-Excited Acetone versus Cumyloxyl Radicals with Amines," *Journal of the American Chemical Society*, Vol. 123, No. 40, 2001, pp. 9727-9737.

Ritchie, B.D., and Seitzman, J.M., "Simultaneous Imaging of Vapor and Liquid Spray Concentration Using Combined Acetone Fluorescence and Phosphorescence," *42nd AIAA Aerospace Science Meeting and Exhibit,*, Reno, Jan. 2004, AIAA 2004-384.

Ruff, G. A., and Faeth, G. M., "Nonintrusive Measurement of the Structure of Dense Sprays," Structure of Dense Sprays, AIAA Publication, 1995, pp. 263-296.

Schulz, C., and Sick, V., "Tracer-LIF diagnostics: Quantitative measurement of fuel concentration, temperature and fuel/air ration in practical combustion systems," Progress in Energy and Combustion Science, Vol. 31, 2005, pp. 75-121.

Seitzman, J. M. and Hanson, R. K., "Planar Fluorescence Imaging in Gases"*, Instrumentation for Flows with Combustion*, Chapter 6, ed. A. M. K. P. Taylor, Academic Press, London, 1993.

Seyfried, H., Brackmann, C., Lindholm, A., Linne, M., Alden, M. Barreras, F., Bank, R. v.d., "Optical Diagnostics Applied to a Gas Turbine Pilot Burner," AIAA Paper 2006-0393.

Society of Automotive Engineers, "Handbook of Aviation Fuel Properties," handbook produced by Committee of the Coordinating Research Council, Inc. (CRC), Third Edition, 2004

Stojkovic, B. D., and Sick, V., "Evolution and impingement of an automotive fuel spray investigated with simultaneous Mie/LIF techniques," Applied Physics B Vol.73, 2001, pp. 75-83.

Thurber, M. C., and Hanson, R. K., "Pressure and composition dependences of acetone laser-induced fluorescence with excitation at 248, 266, and 308 nm," Applied Physics B, Vol. 69, 1999, pp. 229-240.

Thurber, M. C., Grisch, F., and Hanson, R. K., "Temperature imaging with single- and dual-wavelength acetone planar laser-induced fluorescence," Optics Letters, Vol. 22, No. 4, 1997, pp. 251-253.

Thurber, M. C., Grisch, F., Kirby, B. J., Votsmeier, M., and Hanson, R. K., "Measurements and modeling of acetone laser-induced fluorescence with implications for temperature-imaging diagnostics," Applied Optics, Vol. 37, No. 21, 1998, pp. 4963-4978.

Tran, T., Kochar, Y., Seitzman, J., 2005, "Measurements of Liquid Acetone Fluorescence and Phosphorescence for Two-Phase Fuel Imaging," 43rd Aerospace Sciences Meeting and Exhibit, AIAA-2005-0827, pp. 1-8.

Wilkinson, F., and Dubois J.T., "Energy-Transfer Studies by Spectrophotofluorometric Method," The Journal of Chemical Physics, Vol. 39, No. 2, 1963, pp. 377-383.

Yule, A. J., Ereaut, P. R., and Ungut, A., "Droplet Sizes and Velocities in Vaporizing Sprays," Combustion and Flame, Vol. 54, 1983, pp.15-22.

ACKNOWLEDGEMENTS

I would like to take this opportunity to express my thanks to those who helped me with various aspects of conducting research and the writing of this thesis. First and foremost, Dr. Terrence R. Meyer for his guidance, patience and support throughout this research and the writing of this thesis. His insights and words of encouragement have often inspired me and renewed my hopes for completing my graduate education. I would also like to thank my committee members for their efforts and contributions to this work: Dr. Theodore Heindel and Dr. Hui Hu.

Outside of my Iowa State University academic career there have been positive influences on my life as well. Dr. Gregory Nellis at the University of Wisconsin at Madison opened my eyes to college academics and research. It was while working at the university for him that I began to truly understand my love with learning and knowledge.

Lastly and perhaps most importantly, many thanks go out to my family as they have always been there to encourage and help me pursue my education. My mother, father and sister have played an instrumental part in helping become whom I am today. A very special thanks goes to my grandfather, Robert Hardcopf, Sr. He has always served as a guiding force in college, personal relations, and more importantly life. His contributions to my life are immeasurable.